Light Water Reactor Sustainability Program

Long-Term Crack Initiation Behavior of Alloy 690 and Its Weld Metals in PWR Primary Water

March 2020

U.S. Department of Energy

Office of Nuclear Energy

DISCLAIMER

This information was prepared as an account of work sponsored by an agency of the U.S. Government. Neither the U.S. Government nor any agency thereof, nor any of their employees, makes any warranty, expressed or implied, or assumes any legal liability or responsibility for the accuracy, completeness, or usefulness, of any information, apparatus, product, or process disclosed, or represents that its use would not infringe privately owned rights. References herein to any specific commercial product, process, or service by trade name, trade mark, manufacturer, or otherwise, does not necessarily constitute or imply its endorsement, recommendation, or favoring by the U.S. Government or any agency thereof. The views and opinions of authors expressed herein do not necessarily state or reflect those of the U.S. Government or any agency thereof.

Long-Term Crack Initiation Behavior of Alloy 690 and Its Weld Metals in PWR Primary Water

Ziqing Zhai
Matthew J. Olszta
Mychailo B. Toloczko
Stephen M. Bruemmer

Pacific Northwest National Laboratory

March 2020

Prepared for the
U.S. Department of Energy
Office of Nuclear Energy

ABSTRACT

Determining the resistance of high-Cr Ni-base Alloy 690 and its weld metals 152/52 to environmental degradation during long-term pressurized water reactor (PWR) exposure is needed to confirm their viability as the replacement material for Alloy 600/182/82 and help establish a quantitative factor of improvement for SCC initiation. This report updates the ongoing long-term constant load SCC initiation testing on 42 Alloy 690 specimens from seven control rod drive mechanism/plate/bar heats with different cold-worked (CW) levels and thermal-mechanical histories where susceptibility to SCC growth has been documented in tests at PNNL. Previous results identified unexpected observations of grain boundary cavity formation and precursor IG cracking in a few highly CW heats. This report summarizes the third series of detailed characterizations performed after SCC testing reaches ~28,000 hours on the original materials and ~18,600 hours on replacement materials to assess the evolution of precursor damage and IG cracks with direct comparisons to previous examinations. In addition, this report reviews the long-term blunt notch testing conducted on two Alloy 52M weld specimens in collaboration with an NRC program at PNNL on SCC crack growth. These Alloy 52M welds have a high density of pre-existing ductility-dip cracks which is recognized as a significant issue during the joining of high-Cr, Ni-base alloys. This study provides critical information on whether the presence of pre-existing weld defects can promote SCC initiation and growth in service with systematic test approach and periodic examination of the weld defects. The results from both of these long-term SCC initiation tests are benefiting not only the LWRS Program but also the EPRI/NRC joint program on SCC initiation where similar long-term tests are underway on Alloy 690, 152 and 52 materials in a single CW condition.

ACKNOWLEDGEMENT

The authors gratefully acknowledge the financial support from the Office of Nuclear Energy, U.S. Department of Energy through the Light Water Reactor Sustainability Program. In addition, support is recognized from the U.S. Nuclear Regulatory Commission for pre-test microstructural characterizations of cold worked Alloy 690 materials and blunt notch SCC initiation testing on Alloy 52M materials. Dr. Karen Kruska is acknowledged for performing the FIB serial trenching on Alloy 690 specimens. Key technical assistance from Anthony Guzman, Ryan Bouffioux, Ferdinan Colon, and Ryley Peterson is acknowledged for SCC initiation testing and materials preparation activities.

CONTENTS

FIGURES

TABLES

ACRONYMS

BSE	backscatter electron
BN	blunt notch
CF	cold-forged
CGR	crack growth rate
CLT	constant load tensile
CR	cold-rolled
CRDM	control rod drive mechanism
CT	compact tension
CW	cold-worked
DCPD	direct current potential drop
DDC	ductility dip cracking
EBSD	electron backscattered diffraction
EDS	energy dispersive x-ray spectroscopy
EPRI	Electric Power Research Institute
FEM	finite element modeling
FIB	focused-ion-beam
GB	grain boundary
IG	intergranular
LAS	low alloy steel
LWR	light water reactor
MA	mill-annealed
NRC	Nuclear Regulatory Commission
PWR	pressurized water reactor
SA	solution-annealed
SCC	stress corrosion cracking
SEM	scanning electron microscope
TT	thermally treated
WD	weld defect
YS	yield stress

Long-Term Crack Initiation Behavior of Alloy 690 and Its Weld Metals in PWR Primary Water

PROJECT BACKGROUND

Objective

This research project addresses one of the least understood aspects of stress corrosion cracking (SCC) for light water reactor (LWR) pressure boundary components - crack initiation. The focus of the work is to investigate important material (composition, processing, microstructure, strength) and environmental (temperature, water chemistry, electrochemical potential, stress) effects on the SCC susceptibility of corrosion-resistant, nickel-base alloys. The primary objectives are to identify mechanisms controlling crack nucleation, investigate the transition from short to long crack growth in these alloys under realistic LWR conditions and help establish the framework to effectively model and mitigate SCC initiation processes.

Approach

Alloy 600 materials were selected for the first phase of SCC initiation experimentation followed by testing on the more resistant Alloy 690 materials. For both alloys, material variants known to influence SCC response are being examined including cold/warm work (forged, rolled and tensile strained), banded/inhomogeneous microstructures (plate versus extruded tubing), grain boundary precipitation (heat-to-heat variations, mill-annealed, solution annealing and changes due to thermal treatments) and surface grinding (various damage depths, surface roughness and nanocrystalline layers). Materials and material conditions have been identified and obtained from an ongoing research project for the U.S. Nuclear Regulatory Commission (NRC) where stress-corrosion crack growth has been characterized, thus creating an important link between SCC initiation and propagation behavior. Detailed examinations have been performed using optical and electron microscopy to establish key bulk and surface microstructural features that may act as initiation precursors. Dedicated test systems with continuous in-situ detection of crack formation were designed and constructed enabling SCC initiation experimentation of a range of Alloy 600 and 690 materials. After SCC testing in high temperature autoclave systems, surface and near-surface characterizations were conducted to document nano-to-microscale initiation precursors leading to macroscopic stress corrosion cracks. The fundamental understanding of how the near-surface microstructure is degraded during high-temperature water exposure is essential to an improved predictive methodology for SCC initiation. Collaborations with ongoing PNNL projects supported by the NRC and EPRI play an important role in our research and has enabled testing on an expanded matrix of Alloy 600/690 and Ni-base alloy weld metals.

Focus of Current Report

This report reviews the long-term SCC initiation testing and characterization activities on Alloy 690 and its weld metals Alloy 152/52 in high temperature, simulated pressurized water reactor (PWR) primary water. Following earlier milestone reports that detailed precursor damage evolution and crack initiation in CW Alloy 690 materials after ~1.1 and 2.1 years of exposure [1-3], the first part of this report provides a detailed update on the microstructural characterization activities performed on Alloy 690 SCC initiation specimens after ~3 years of exposure highlighting the effect of starting microstructure, cold work and applied stress on the evolution of precursor damage and short cracks. Additional quantification results on grain boundary (GB) cavities were also included to establish correlation between cavity evolution and cold work levels for predicting long-term degradation behavior of Alloy 690 in PWR service relevant

conditions. The second part of this report reviews the long-term blunt notch compact tension testing conducted on two Alloy 52M weld specimens in collaboration with an NRC program at PNNL on SCC crack growth. These Alloy 52M welds have a high density of pre-existing ductility-dip cracks and the test is designed to evaluate their potential effects on SCC initiation in PWR primary water. Detailed surface characterizations after exposure times of 3,800, 8,000, 12,000, and 16,000 hours have revealed occasional formation of new cracks and some growth of existing weld cracks. The implication of these pre-existing defects on the SCC initiation susceptibility of high Cr, Ni-base weld metals will be discussed.

LONT-TERM CRACK INITIATION BEHAVIOR OF ALLOY 690 IN PWR PRIMARY WATER

Chapter Overview

SCC initiation testing on cold-worked (CW) Alloy 600 materials in PWR primary water has demonstrated that intergranular (IG) attack is the precursor to SCC initiation in this material [4-6]. In comparison, an equivalent degradation and cracking process does not exist in CW Alloy 690. Due to a much higher Cr content in alloy composition, a compact chromia layer readily forms above GB intersecting the surface when exposed to high-temperature water and remains protective after long term exposures at high stresses. As a result, CW Alloy 690 is considered resistant to SCC initiation. However, recent experimental studies have revealed an alternate mechanism of crack initiation in this material through formation and growth of grain boundary cavities induced by creep [7-12]. To better understand the evolution of GB cavities and predict degradation of Alloy 690 in realistic PWR operating conditions, systematic long-term SCC initiation testing is being performed at PNNL to evaluate factors influencing GB cavity formation and growth in seven commercial Alloy 690 heats. To date, the test consists of four phases with the first three phases each lasted for about 1.1 year and the fourth one ongoing. While the precursor damage and crack morphology after Phase I and Phase II exposure have been reported in detail in previous milestone reports, current report focuses on the new characterization results on moderately and highly CW Alloy 690 materials after Phase III exposure. Nucleation of IG cracks associated with creep cavities were evidenced in an Alloy 690 thermally treated (TT) material with slightly less susceptible microstructure in both 21% and 31% CW conditions after extended exposure at yield stress, but no crack initiation has yet been detected by direct current potential drop (DCPD). Meanwhile, elimination of GB carbides, decrease in applied stress and cold work level all have shown to significantly hinder GB cavity growth. These results are providing key information to better predict long-term degradation behavior for in-service Alloy 690 materials.

Experimental Procedures

Constant Load Tensile (CLT) Test on Cold-Worked Alloy 690 Materials

The precursor damage evolution and crack initiation behavior in CW Alloy 690 is being evaluated using CLT test. In such test, multiple (up to 36) tensile specimens can be tested simultaneously in the same environment where the stress state and surface condition can be varied for each individual specimen, providing an efficient way to assess the effects of various factors on SCC initiation. 30.4 mm (1.2-inch) tall uniaxial tensile specimens are being used for the CLT test (Figure 1). All specimens have an identical gauge length of 4 mm and were machined with the gauge section along the thickness direction (short transverse) of the forged/rolled block. By varying the gauge diameter, different stress levels can be achieved in the specimens loaded in the same string, allowing them to be tested at their yield stress (YS) or any other target stress under the applied load. In this test, the diameters of the CLT specimens varied from 2.92 to 3.19 mm enabling them to be tested at their yield stress using a target load of 4670 N (~1050 lbs) exerted by a high-precision servo-electric load control system. At the beginning of the long-term SCC initiation test on Alloy 690, three specimens were prepared for each combination of heat and cold work condition with one polished to a 1 μm surface condition and the other two a ground finish on the gauge emulating surface damage condition of in-service LWR components [13]. With the progression of the test, a number of these original specimens were selectively removed for destructive examinations, and new replacement specimens were added to the test. The material condition of the new specimens is determined with expanded interest in exploring the effect of more variables on crack initiation in Alloy 690 and were not necessarily the same as the ones being replaced. An 1 μm surface finish were prepared for these new specimens allowing detailed characterization of precursor damage and cracks on the surface.

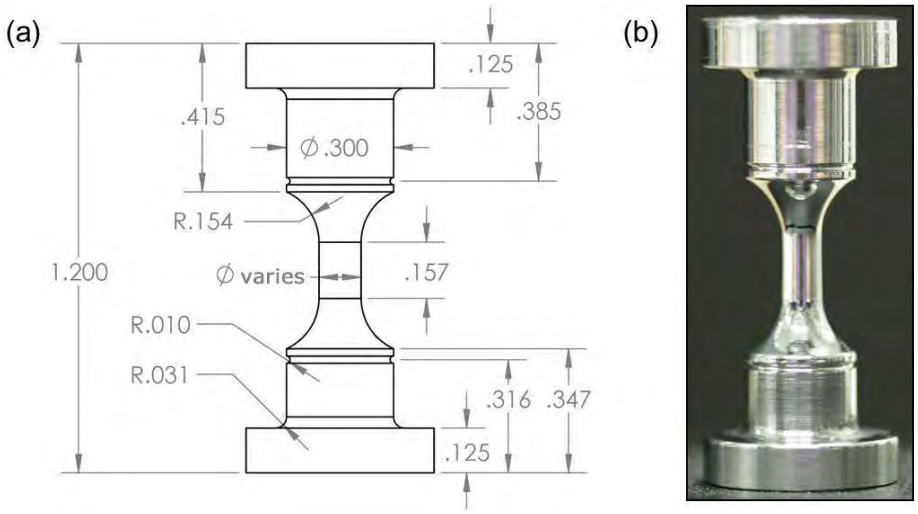

Figure 1. PNNL initiation specimen design. Gauge diameter is selected based on material strength and can be varied from 2.75-4.5 mm (0.11-0.18 inches) and the gauge length is 4.0 mm (0.157 inches). Overall height is 30.5 mm (1.2 inches).

Figure 2 shows the load train and DCPD instrumentation for the typical SCC initiation specimen set up at PNNL. Currently two smaller SCC initiation systems and one large SCC initiation system are being used under the scope of LWRS. The two small SCC initiation systems can test up to 6 fully instrumented specimens, and the large SCC initiation system allows 36 specimens be tested simultaneously with up to 24 specimens instrumented. The long-term SCC initiation testing on Alloy 690 is currently being conducted in the large test system and one of the small systems on a total of 42 specimens. The load frame in both types of systems is designed to sustain the load even when individual specimens fail during the test enabling the test to continue for the other specimens loaded in the same string. However, it is important to note that none of the LWRS Alloy 690 specimens have been allowed to fail during an SCC initiation test and all specimens have been removed shortly after DCPD-indicated initiation to assess cracking.

A reversing DCPD technique developed by General Electric [14] and KAPL [15] was adapted for on-line monitoring of SCC initiation behavior with details provided in previous publications [4, 16]. DCPD voltage across the gauge section is sensitive not only to reduction in cross-sectional area of the gauge region due to crack formation, but also to changes in gauge length and diameter from creep strains that occur during testing. Due to a limited number of holes in the feed through connector for wire passage in the large test system, originally only the highly polished specimen from each combination of heat and cold work condition was instrumented by DCPD, and resistivity drift was not monitored as we normally do for specimens tested in smaller autoclaves. If the highly polished specimen was removed from the test later on, then a specimen with a ground surface finish from the same material and cold work condition would be monitored instead. With progression of the test, a few original 3-specimen sets were completely removed. In such case, the opened-up DCPD vacancy will be assigned to newer specimens of high interest (e.g. longer exposure time, susceptible microstructure, etc.).

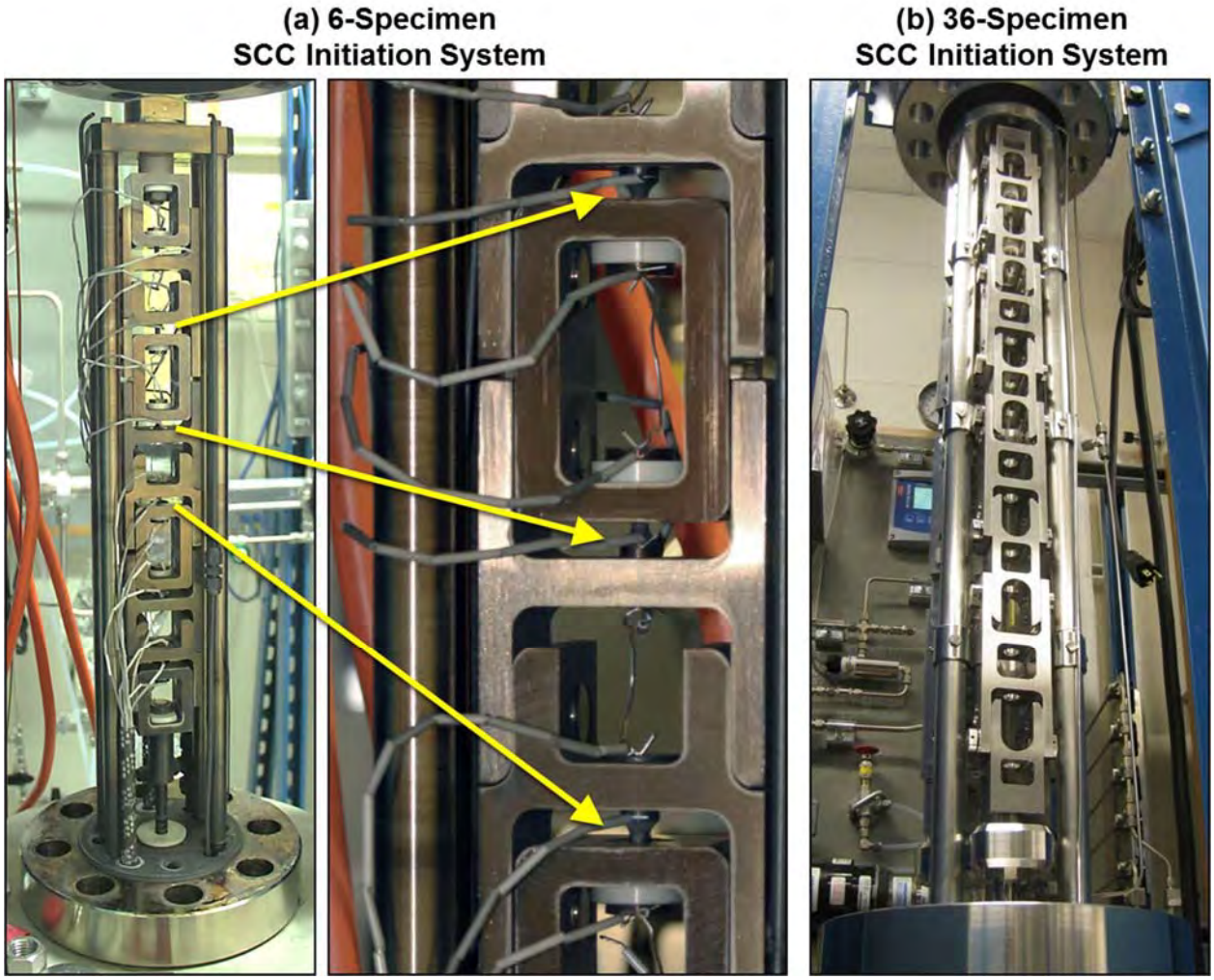

Figure 2. Crack initiation test system load train at PNNL in the (a) small SCC initiation test system with capacity of testing up to 6 fully instrumented specimens and the (b) large SCC initiation test system with capacity of testing up to 24 instrumented specimens and up to 36 specimens in total.

Alloy 690 Materials and Pre-Test Microstructures

This section summarizes the pre-test microstructural characterization on the materials being investigated in the first two stages of the long-term SCC initiation experiment on CW Alloy 690. Most initial examinations were conducted on these heats as part of a NRC project at PNNL investigating SCC crack growth behavior [17, 18]. GB microstructures were characterized in detail for both the as-received and CW conditions. Heat-to-heat comparisons were made focusing on the distribution of permanent damage induced during cold work.

Examinations of As-Received Alloy 690 Microstructures

Three Alloy 690 control rod drive mechanism (CRDM) heats from three different manufacturers have been evaluated as listed in Table 1. All materials are in the TT condition with a semi-continuous GB carbide coverage as shown by the SEM-BSE images in Figure 3. Grain size images in Figure 4 indicated that the Valinox and Doosan materials have a grain size of ~90 µm while the Sumitomo CRDM has a smaller average grain size of ~35 µm with significant twinning.

Table 1. Composition, heat treatment and mechanical properties for the as-received Alloy 690TT CRDM materials.

Source/ Manufacturer and Heat #	Dimension (mm)	Composition, wt%	Heat Treatments and Room Temp. Mechanical Properties
Valinox/ Valinox RE243 Tube 2360	112 OD x 34 wall	Ni-28.9Cr-10.4Fe-0.02C-0.3Mn-0.35Si-0.14Al-0.23Ti-0.024N-0.008P-0.0005S	1122°C/~1 min, WQ + 716-725°C/10.5h, Air Cool YS = 255 MPa, HV = 157 kgf/mm^2
EPRI/ Sumitomo E67074C Tube	127 OD x 33 wall	Ni-29.8Cr-9.8Fe-0.02C-0.29Mn-0.23Si-0.03Cu-0.0002S	Anneal + 725°C/10h/Air Cool YS and HV not measured
EPRI/ TK-VDM (Doosan) 133454 Bar	152 OD solid bar	Ni-29.1Cr-8.9Fe-0.020C-0.26Mn-0.29Si-0.26Al-0.32Ti-0.01Cu-0.02N-0.005P-<0.002S-0.002B	1045°C/4 hr/WQ + 720°C/10h/Air Cool YS = 263 MPa, HV = 165 kgf/mm^2

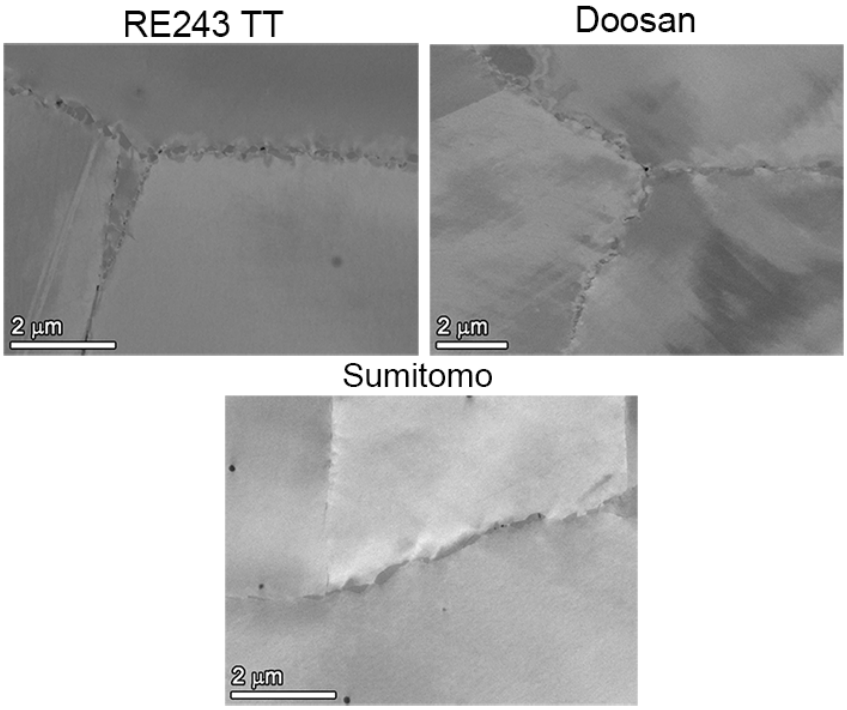

Figure 3. SEM-BSE images illustrating the GB microstructures for the three Alloy 690TT CRDM materials in the as-received condition.

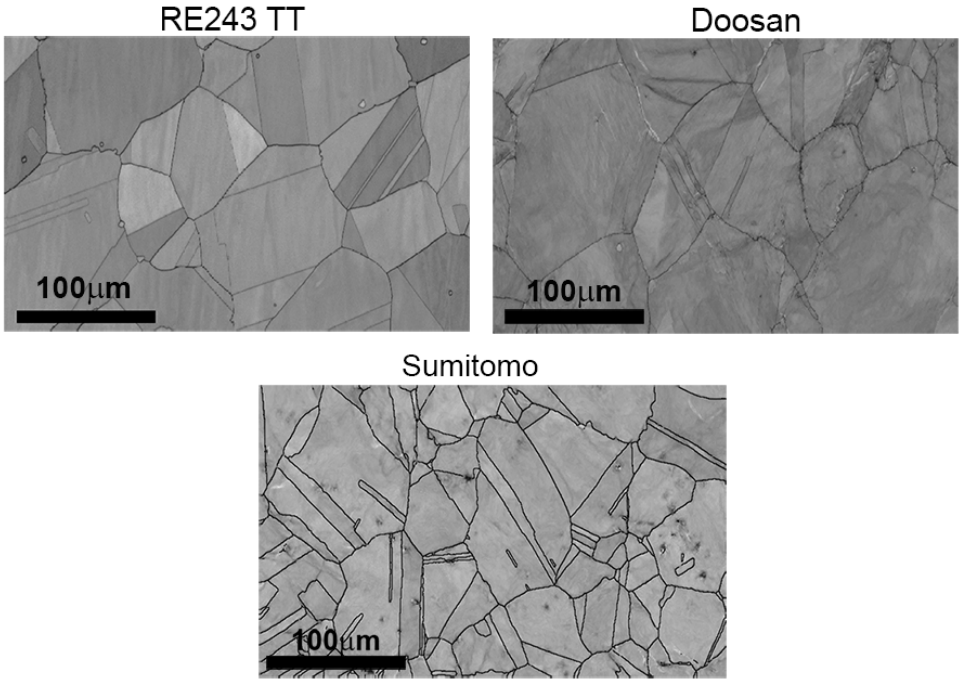

Figure 4. SEM EBSD pattern quality maps showing the general microstructure and grain size for the three Alloy 690TT CRDM materials in the as-received condition.

Four Alloy 690 plate/bar materials from three manufacturers have also been evaluated with specifications given in Table 6. Carbide precipitation was limited to a few isolated GBs in the mill-annealed (MA) GEG B25K heat, while the MA ANL NX3297HK12, the TT TK-VDM 114092 and the Allvac X87N-1 heats exhibited a moderate distribution of IG carbides as shown in Figure 5. SEM-electron backscattered diffraction (EBSD) pattern quality images in Figure 6 show that the grain size is ~15 μm for the GEG material, ~50 μm for the ANL material and ~30 μm for the TK-VDM material. This information on the CRDM and bar/plate heats is summarized in Table 3.

Table 2. Composition, heat treatment, and mechanical properties for the Alloy 690 bar/plate materials covered in this report.

Source/Manufacturer and Heat #	**Composition, wt%**	**Heat Treatments and Room Temp. Mechanical Properties**
ANL/ Special Metals NX3297HK12	Ni-29.5Cr-9.9Fe-0.03C-0.20Mn-0.07Si-0.01Cu-<0.001S	1038°C/2 hr/AC YS not measured, HV = 173 kgf/mm^2
GEG/ Allvac B25K	Ni-29.3Cr-9.2Fe-0.034C-0.22Mn-0.06Si-0.26Al-0.37Ti-<0.01Cu-0.03N-0.006P-<0.0003S-<0.001B	996°C/20 min/AC YS = 294 MPa, HV = 173 kgf/mm^2
EPRI/TK-VDM 114092	Ni-29.5Cr-9.5Fe-0.020C-0.25Mn-0.26Si-0.32Al-0.36Ti-<0.01Cu-0.003P-<0.002S	1030°C/1 hr/WQ + 715°C/10 hr/AC YS = 285 MPa, HV = 155 kgf/mm^2
EPRI/ Allvac X87N-1	Ni-30.0Cr-9.2Fe-0.020C-0.20Mn-0.05Si-<0.01Cu-<0.0003S	1030°C/4 hr/WQ + 727°C/5 hr/AC YS = 265 MPa, HV not measured

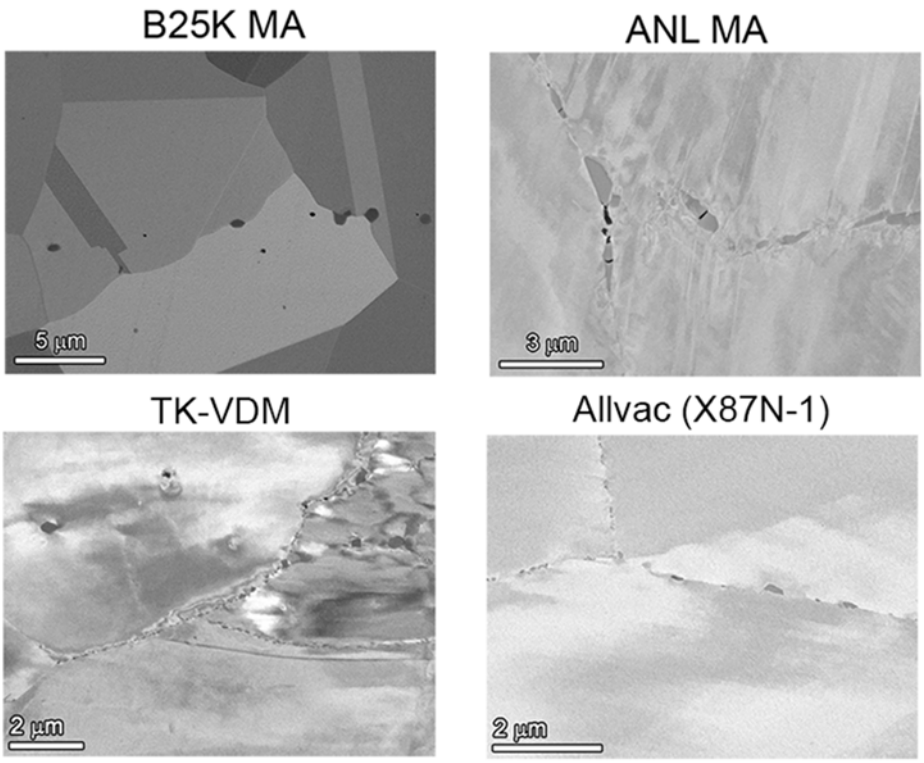

Figure 5. SEM-BSE images illustrating differences in the GB carbide microstructures for each of the Alloy 690 plate/bar materials in the as-received condition.

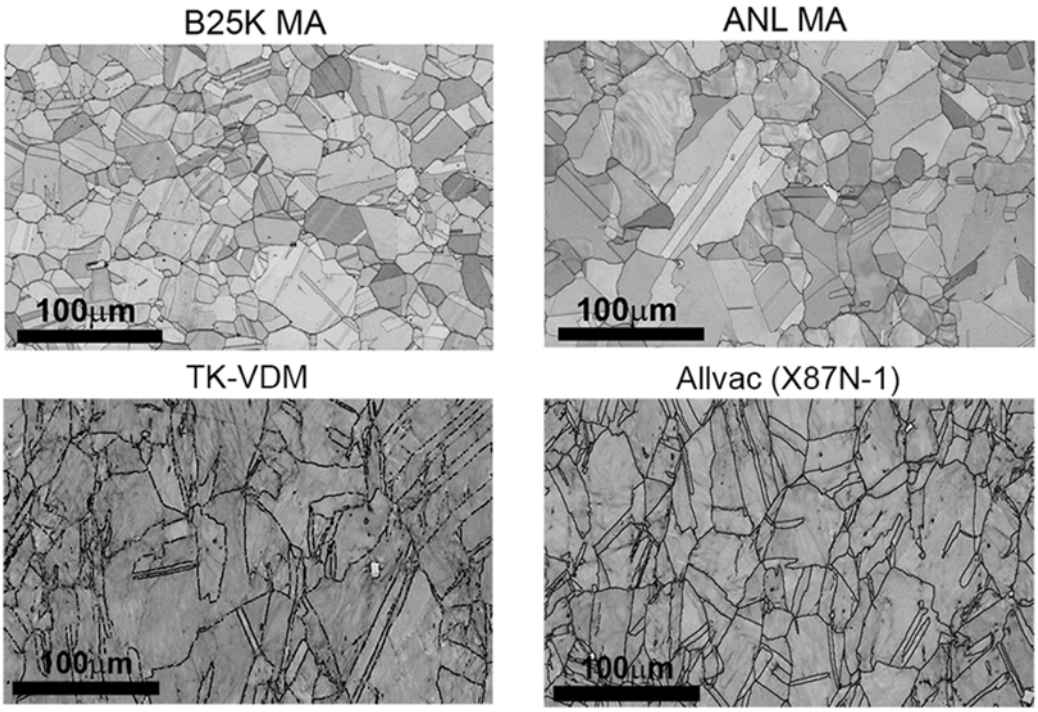

Figure 6. SEM EBSD pattern quality maps showing the grain size for the three Alloy 690 plate/bar materials.

Table 3. Summary of grain size and carbide distributions for materials selected for SCC initiation testing.

Material	Grain Size (μm)	Carbide Location, Size	GB Carbide Density
CRDM Materials			
Valinox RE243 TT	~90	IG, 50–200 nm	Semi-continuous, spacing ~100 nm
Doosan 133454 TT	~90	IG, 1–5 μm	Semi-continuous, spacing ~0.5–2 μm
Sumitomo E67074C TT	~35-40	IG, 50–300 nm	Semi-continuous, spacing ~100 nm
Plate/Bar Materials			
GEG B25K MA	~10-15	TG and isolated IG, 1–3 μm	Low
ANL HK3297HK12 MA	~20-25	IG, 0.5–3 μm	Semi-continuous, spacing ~0.2–2 μm
TK-VDM 114092 TT	~35-40	IG, 50-200 nm	Semi-continuous, spacing ~0.1–0.5 μm
Allvac X87N-1	~20-25	IG, 50-200 nm	Semi-continuous, spacing ~200 μm

Permanent Damage in CW Alloy 690 Materials

Prior to testing, the materials were either cold-forged (CF) or cold-rolled (CR) to produce a cold work level ranging from 12 to 32%. Most combinations of these material and cold work condition had already been evaluated for SCC crack growth behavior in the NRC project on SCC crack growth, where all heats in the 20-32%CW condition exhibited moderate-to-high SCC crack growth rates (CGR) except the Allvac X87N-1 plate heat. It is important to note that the pre-test cold work had introduced permanent damage in all CW materials. This damage was present at GBs as nano-to-micrometer size cavities and small, cracked precipitates, both of which increased in density as cold work level increased. It is also revealed that the size and density of permanent damage induced by cold work has a strong dependence on GB microstructure. An example is shown in Figure 7, where the permanent damage induced by cold work in the 31%CF Alloy 690TT Valinox and Doosan CRDM materials are highlighted. The images are shown at the same scale providing a direct comparison of the size and distribution of cavities and cracks. Apparently, the materials exhibiting fine carbides at GBs often feature small voids at a higher density on certain boundaries, whereas the damage in the materials having larger and more widely spaced carbides are also larger and more spaced out. A summary of the degree of damage for the CRDM materials and Plate/Bar materials is provided in Table 4 and Table 5, respectively.

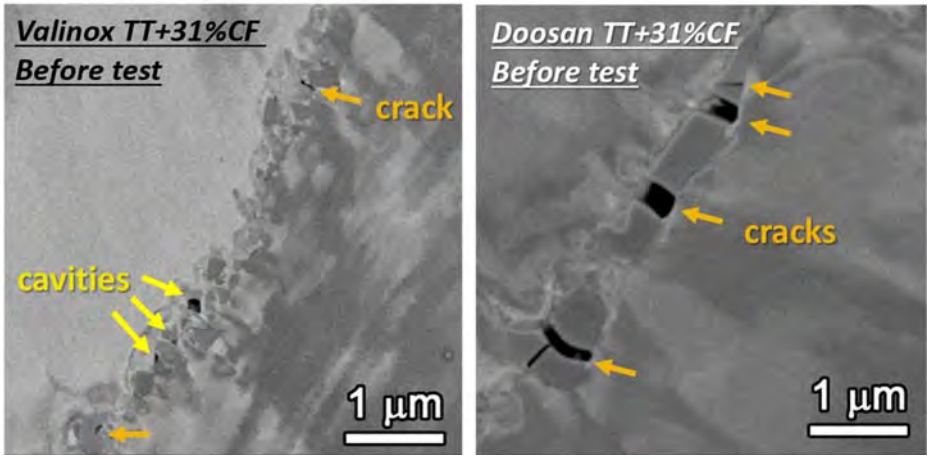

Figure 7. SEM-BSE image shown in the scale illustrating the permanent damage (highlighted by arrows) induced by cold work in the 31%CF Alloy 690TT Valinox and Doosan CRDM materials.

Table 4. Summary of carbide microstructures and damage morphologies in CW Alloy 690 TT CRDM materials.

Material	AR GB Carbide Microstructure		Cold Work Induced GB Damage	
	Location, Size	Density, Spacing	Density of Cracked GB Precipitates	IG Void Density
Valinox RE243 12% CF*	IG, 50–200 nm	Semi-continuous, spacing ~100 nm	None–Low	Low
Valinox RE243 21% CF*			Low	Low–Moderate
Valinox RE243 31% CF*			Low	Moderate
Sumitomo E67074C 21% CF	IG, 50–200 nm	Semi-continuous, spacing ~100 nm	Low	Low–Moderate
Sumitomo E67074C 31% CF			Low	Moderate
Doosan 133454 21% CF	IG, 1–5 µm	Semi-continuous, spacing ~0.5–2 µm	Low	Low–Moderate
Doosan 133454 31% CF			Low	Moderate

Table 5. Summary of carbide microstructures and damage morphologies in CW Alloy 690 plate and bar materials.

Material	AR GB Carbide Microstructure		Cold Work Induced GB Damage	
	Location, Size	Density, Spacing	Density of Cracked GB Precipitates	IG Void Density
ANL MA 26% CR	IG, 0.5–3 µm	Semi-continuous, spacing ~0.2–2 µm	Moderate	Moderate–High
GEG MA 18% CR	Primarily TG, 1–3 µm	Low density, unevenly distributed	None–Low	None–Low
TK-VDM 114092 22% CF	IG, 50–200 nm	Semi-continuous, spacing ~0.2–0.5 µm	Low	Low–Moderate
TK-VDM 114092 32% CF			Low	Moderate
Allvac X87N-1 21% CF	IG, 50-200 nm	Semi-continuous, spacing ~0.2–0.5 µm	Low-Moderate	Moderate

Microstructural characterizations

SEM/FIB Examinations

Characterizations started by documenting the entire gauge surface of all specimens after each test interruption using a JEOL 7600 scanning electron microscope (SEM). In order to achieve this, four fiducial scribe marks (90° to one another) were made at the button ends of each specimen to keep track of the specimen orientation. Each of the four orientations was then mapped using high-kV backscatter electron (BSE) montage imaging so that features covered by thin surface oxides can be revealed. However, after Phase II exposure, a layer of densely packed spinel oxides was found on the surface of all highly polished specimens due to extended exposure in high-temperature water, making it difficult to resolve GB damage features even under high-kV conditions. To solve this issue, a non-aggressive surface oxide stripping method was developed to remove this excessive oxide layer with little impact to the surface [2]. It turned out that this method is effective and specimens received oxide stripping at the 2nd test interruption did not need to be treated again after Phase III exposure for detailed surface examination.

As will be shown later in the Results section, no specimen was removed from the test for destructive cross-section examination after Phase III exposure. In order to get an idea on the sub-surface morphology of some precursor damage and cracks identified on specimen surface, a FEI Quanta field-emission-gun, dual-beam focused-ion-beam (FIB)/SEM system was used to create shallow trenches intersecting the identified features. Serial milling was often employed to document the sub-surface damage evolution along GBs, if there is any.

Quantification of Precursor Damage in Alloy 690

As reported in previous milestone report [2, 3], detailed quantification on GB cavities was conducted on highly CW Alloy 690 specimens to better understand the effect of starting microstructure and applied stress. The quantification activities have continued this fiscal year expanding to moderately CW TT+21%CF Valinox and Doosan Alloy 690 specimens removed after Phase I and II exposure. Great care was taken during cross-section polish to avoid precipitate fallouts, and during image acquisition to differentiate cavities from artefacts to obtain reliable data for analysis. Finite element modeling (FEM) also was performed on these specimens prior to SEM examination to analyze the stress distribution from the gauge center to the fillet region where a gradually increasing diameter results in a decreased stress. Quantification were performed on both the gauge center loaded at high stress (100% YS) and the reference region under low load (~15% YS) during exposure (Figure 8). An area with a fixed size of 150×150 μm^2 near the centerline was selected in each region based on low-magnification montage image where GB cavities were indicated. The size of the squared area was chosen such that multiple grains can be included irrespective of heat. SEM-BSE images were acquired along every high-energy GB included in the area using a magnification of 15,000X, which allows sufficient resolution for nm-sized cavities. Low-kV imaging with fixed contrast and brightness was used to prevent any unwanted bias in cavity size due to change in imaging settings. Generally, 100 to 150 images were taken in each area, stitched together and processed in *Image J*, an open source image processing program. While this software can effectively remove most unrelated objects and background in the images, further correction was manually made on misidentified features by comparing the processed images to the original ones. These mainly include unremoved TiN precipitates and surface contamination that produced a contrast similar to that of the cavities, as well as partially missing cavities due to accumulation of polish remnants. More details on this topic can be found in a previous publication [12]. Upon completion of image processing on the GBs, data on the number and size of the cavities were automatically collected using *Image J*. Two parameters, cavity density and cavity coverage, were chosen to quantify the distribution of GB cavities using expressions listed below:

$$\text{Cavity density} = \frac{\sum \text{number of IG cavities}}{\text{GB length}} \quad (1)$$

$$\text{Cavity coverage} = \frac{\sum \text{height of IG cavities}}{\text{GB length}} \ \% \quad (2)$$

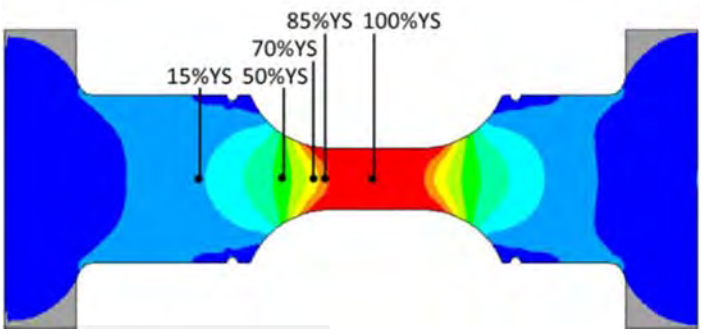

Figure 8. FEM analysis of the Von Mises stress distribution in the specimen when the gauge section is loaded at yield stress.

Results

Test Update

Because Alloy 690 shows a strong increase in SCC CGR with cold work, it was determined to assess the susceptibility to SCC initiation in CW Alloy 690 materials. To better understand SCC initiation response in CW Alloy 690 materials, long-term SCC initiation testing has been established and continued since 2014. Figure 9 shows the SCC CGR obtained by our NRC project [17, 18] for the materials that have been selected for SCC initiation evaluation. The research first started with three Alloy 690TT CRDM heats and three TT/MA plate/bar heats that exhibited high SCC crack growth rates at CW levels from 20–30%. These materials are being tested for SCC initiation response in 360°C simulated PWR primary water in 12–31% CW conditions. Starting from Phase II, the test matrix was expanded to include more variations in GB carbide distribution (TT vs. SA), applied stress (100% YS versus 90% YS), and heat IGSCC susceptibility in the highly CW condition (moderate-high CGR vs. low CGR). To-date the study consists of four phases each lasted for approximately one year with selected specimens continuing through all four exposures. Phase I and II exposures were conducted each for approximately one year on 36 specimens in the large SCC initiation test system. 13 specimens were removed after Phase I exposure with another 13 new replacement specimens adding in. 7 specimens were removed after Phase II exposure with another 10 new specimens added. Since crack initiation was detected by DCPD in a highly CW Alloy 690TT Valinox CRDM specimen near the end of the Phase II exposure, decision was made to move three specimens that have a higher susceptibility to SCC initiation than the others from the large test system to a small test system. This gave more flexibility in stopping the test to remove the specimens once crack initiation is detected, while exposure can continue in the large test system without disturbance. It also allows referenced DCPD response to be monitored on these specimens, thus providing more accurate determination of crack initiation. This turned out to be a wise decision as one of the three specimens in the small system did show sign of initiation after ~3,800 hours of additional exposure, and we were able to shut down the test, remove the specimen, and restart the test much more quickly than handling the large 36-specimen system. Besides the initiated specimen, no more specimens were removed after Phase III exposure ended, but it was again determined to move six of the original specimens to a small system for better DCPD monitoring and more flexibility in test control. Therefore, six more new replacement specimens were prepared and added to the large system, making a total number of specimens in test to 42. As of March 2020, Phase IV exposure has been ongoing for ~2,700 hours in the large 36-specimen test system and ~3,500 hours in the small 6-specimen test system with the original specimens now reaching a total exposure time of >31,300 hours. In Figure 10, a progression bar chart is provided illustrating the heat and material conditions evaluated in each phase and their up-to-date exposure times. A more detailed status summary on all the tested and in-test specimens is provided in Table 6.

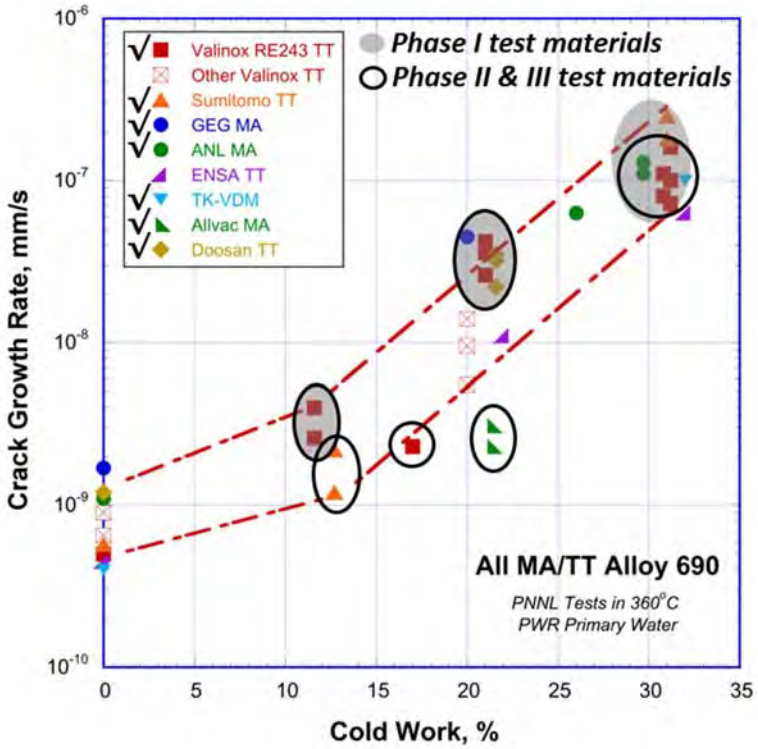

Figure 9. SCC CGR response of TT/MA Alloy 690 materials obtained at PNNL through a Nuclear Regulatory Commission (NRC) project [17, 18]. The heats and cold work levels selected for SCC initiation evaluation at each stage were checked in the label box and circled in the plots, respectively.

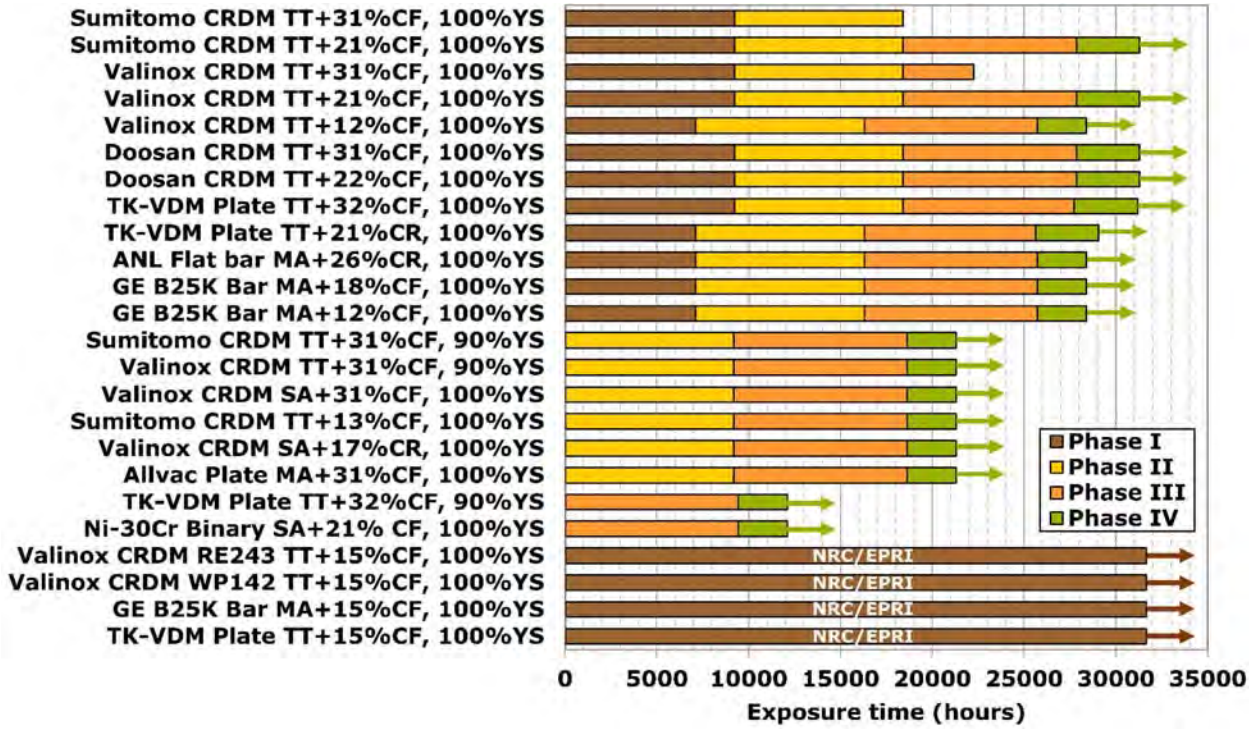

Figure 10. Exposure time of the CW Alloy 690 materials evaluated at Phases I–IV of the SCC initiation testing. The Phase IV is ongoing and the plotted exposure time is up-to-date as of March 2020.

Table 6. Summary of material condition and SCC initiation testing status of all the tested Alloy 690 specimens (as of March 2020).

Specimen	Material	Material Condition	Surface Condition	Applied Stress† (MPa)	Exposure time (h)			
					Phase I	Phase II	Phase III	Phase IV
IN024	Sumitomo CRDM	TT + 21% CF	1 μm	590	9220	9180	9440	3440*
IN025■	Sumitomo CRDM	TT + 21% CF	Ground C	590	9220	9180	/	/
IN026■	Sumitomo CRDM	TT + 21% CF	Ground C	590	9220	/	/	/
IN027	Valinox CRDM	TT + 21% CF	1 μm	525	9220	9180	9440	3440*
IN028■	Valinox CRDM	TT + 21% CF	Ground C	525	9220	9180	/	/
IN029■	Valinox CRDM	TT + 21% CF	Ground C	525	9220	/	/	/
IN030	Doosan CRDM	TT + 21.6% CF	1 μm	555	9220	9180	9440	2670*
IN031■	Doosan CRDM	TT + 21.6% CF	Ground C	555	9220	9180	/	/
IN032■	Doosan CRDM	TT + 21.6% CF	Ground C	555	9220	/	/	/
IN033■	Sumitomo CRDM	TT + 31% CF	1 μm	710	9220	/	/	/
IN034■	Sumitomo CRDM	TT + 31 % CF	Ground C	710	9220	/	/	/
IN035■	Sumitomo CRDM	TT + 31% CF	Ground C	710	9220	9180	/	/
IN036■	Valinox CRDM	TT + 31% CF	1 μm	720	9220	9180	3845	/
IN037■	Valinox CRDM	TT + 31% CF	Ground C	720	9220	9180	/	/
IN038■	Valinox CRDM	TT + 31% CF	Ground C	720	9220	/	/	/
IN039	Doosan CRDM	TT + 31% CF	1 μm	685	9220	9180	9440	3440*
IN040■	Doosan CRDM	TT + 31% CF	Ground C	685	9220	9180	/	/
IN041■	Doosan CRDM	TT + 31% CF	Ground C	685	9220	/	/	/
IN042	TK-VDM Plate	TT + 31.9% CF	1 μm	700	9220	9180	9332	3440*
IN043■	TK-VDM Plate	TT + 31.9% CF	Ground C	700	9220	9180	/	/
IN044■	TK-VDM Plate	TT + 31.9% CF	Ground C	700	9220	/	/	/
IN053	ANL Flat Bar	MA + 26% CR	1 μm	775	7110	9180	9440	2670*
IN054	ANL Flat Bar	MA + 26% CR	1 μm	775	7110	9180	9440	2670*
IN055■	ANL Flat Bar	MA + 26% CR	Ground C	775	7110	/	/	/
IN056	GE B25K Bar	MA + 18.3% CF	1 μm	550	7110	9180	9440	2670*
IN057	GE B25K Bar	MA + 18.3% CF	1 μm	550	7110	9180	9440	2670*
IN058■	GE B25K Bar	MA + 18.3% CF	Ground C	550	7110	/	/	/
IN059	TK-VDM Plate	TT + 21% CR	1 μm	675	7110	9180	9332	3440*
IN060	TK-VDM Plate	TT + 21% CR	1 μm	675	7110	9180	9440	3440*
IN061■	TK-VDM Plate	TT + 21% CR	Ground C	675	7110	/	/	/
IN062	GE B25K Bar	MA + 12.4% CF	1 μm	510	7110	9180	9440	2670*
IN063	GE B25K Bar	MA + 12.4% CF	1 μm	510	7110	9180	9440	2670*

IN064■	GE B25K Bar	MA + 12.4% CF	Ground C	510	7110	/	/	/
IN065	Valinox CRDM	TT + 11.7% CF	1 μm	365	7110	/	/	/
IN066	Valinox CRDM	TT + 11.7% CF	1 μm	365	7110	9180	9440	2670*
IN067■	Valinox CRDM	TT + 11.7% CF	Ground C	365	7110	/	/	/
IN172	Allvac Plate	MA + 31%CF	1 μm	655	/	9180	9440	2670*
IN173	Allvac Plate	MA + 31%CF	1 μm	655	/	9180	9440	2670*
IN174	Valinox CRDM	SA + 31%CR	1 μm	650	/	9180	9440	2670*
IN175	Valinox CRDM	SA + 31%CR	1 μm	650	/	9180	9440	2670*
IN176	Sumitomo CRDM	TT + 21%CF	1 μm	575	/	9180	9440	2670*
IN177	Valinox CRDM	TT + 21.9%CF	1 μm	510	/	9180	9440	2670*
IN178	Valinox CRDM	TT + 21.9%CF	1 μm	510	/	9180	9440	2670*
IN179	Sumitomo CRDM	TT + 30.6%CF	1 μm	621 (90%YS)	/	9180	9440	2670*
IN180	Sumitomo CRDM	TT + 30.6%CF	1 μm	621 (90%YS)	/	9180	9440	2670*
IN181	Valinox CRDM	TT + 31%CF	1 μm	630 (90%YS)	/	9180	9440	2670*
IN182	Valinox CRDM	TT + 31%CF	1 μm	630 (90%YS)	/	9180	9440	2670*
IN183	Sumitomo CRDM	TT + 12.7%CF	1 μm	405	/	9180	9440	2670*
IN184	Valinox CRDM	SA + 17%CR	1 μm	335	/	9180	9440	2670*
IN263	Ni-30Cr	SA + 21%CF	1 μm	488	/	/	9440	2670*
IN264	Ni-30Cr	SA + 21%CF	1 μm	488	/	/	9440	2670*
IN265	Ni-30Cr	SA + 21%CF	1 μm	488	/	/	9440	2670*
IN266	TK-VDM CRDM	TT + 32%CF	1 μm	603 (90%YS)	/	/	9440	2670*
IN267	TK-VDM CRDM	TT + 32%CF	1 μm	670	/	/	9440	2670*
IN268	TK-VDM CRDM	TT + 32%CF	1 μm	603 (90%YS)	/	/	9440	2670*
IN269	Valinox RE243	SA + 31%CR	1 μm	655	/	/	9440	2670*
IN270	Valinox RE243	SA + 31%CR	1 μm	655	/	/	9440	2670*
IN271	Doosan CRDM	TT + 21%CF	1 μm	530	/	/	9440	2670*
IN272	Sumitomo CRDM	TT + 21%CF	1 μm	550	/	/	9440	2670*
IN294	Valinox CRDM	TT + 21.9%CF	1 μm	510	/	/	/	2670*
IN295	Valinox CRDM	TT + 21.9%CF	1 μm	510	/	/	/	2670*
IN296	Valinox CRDM	TT + 11.7%CF	1 μm	365	/	/	/	2670*
IN297	Sumitomo CRDM	TT + 12.7%CF	1 μm	405	/	/	/	2670*
IN298	Doosan CRDM	TT + 21.6% CF	1 μm	550	/	/	/	2670*
IN299	Doosan CRDM	TT + 21.6% CF	1 μm	550	/	/	/	2670*

† The applied stress is the yield stress of the specimens at the tested temperature (360°C) unless otherwise specified.

■ Specimens removed for cross-section examination. *Ongoing test.

GB Damage Evolution after Phase III Exposure

As mentioned in the experimental section, SEM examinations were carried out on all specimens at every test interruption. The results after Phase I and II exposures have been reported in several previous LWRS milestone reports [1, 2]. Phase III exposure ended in the summer of 2019 with characterization activities continued into the new fiscal year. In this report, key SEM characterization results after Phase III will be reported with a focus on precursor damage evolution in the moderately and highly CW materials that have been exposed for ~2.1–3.2 years. An update will also be given on the cavity quantification in selected moderately CW materials highlighting the GB microstructure effects on cavity evolution and crack initiation in CW Alloy 690.

Precursor Damage Evolution in Highly CW Alloy 690TT Materials

Previous SEM results after Phases I and II revealed IG cracks formation and growth associated with creep cavities in highly CW Alloy 690TT Sumitomo and Valinox materials featuring small and densely spaced GB carbides loaded at yield stress. By the end of Phase III, specimens from these conditions no longer exists (all were either removed for destructive examination or initiated as indicated by DCPD), therefore this time the SEM characterization focused on the other TT+31%CF specimens with the longest exposure times. A number of specimens in other material/load conditions were also examined in detail to better understand the effect of grain boundary carbide and applied stress on precursor damage evolution and crack initiation.

As indicated in Table 3, the Alloy 690TT TK-VDM heat features small GB carbides that have similar size to those in the Alloy 690TT Sumitomo and Valinox CRDM heats, but with slightly larger spacings in between. As shown in Figure 11a, only a few obvious short cracks were discovered on the gauge surface of the TT+31%CF TK-VDM specimen IN042 after Phase II exposure (highlighted in red) plus some additional continuous IG features of darker contrast indicative of possible cracks (highlighted in green). After an additional ~1.1 year of exposure, a clear increase in the number of obvious cracks was discovered in the gauge surface of this specimen. These cracks were formed either from features previously identified as possible cracks or GBs that previously appear to be intact with examples shown in Figure 12. To get an idea of the sub-surface morphology of these cracks, FIB trenching was carefully employed to intersect selected cracks towards their tip ending location on the surface. Results revealed a series of densely spaced cavities leading at the crack front in the cross-sections, similar to what was observed in the TT+31%CF Sumitomo and Valinox CRDM specimens after Phase I and Phase II exposure. This suggests that while the formation and aggregation of GB cavities may be slower in the TT+31%CF TK-VDM plate material than in the Sumitomo and Valinox CRDM materials due to larger spacings between GB carbides, it has continued to grow with extended exposure and may have acted as precursor to more crack formation. Since most of the cracks are still quite small and no crack initiation has yet been indicated by DCPD, decision was made to put this specimen back to test for longer exposure.

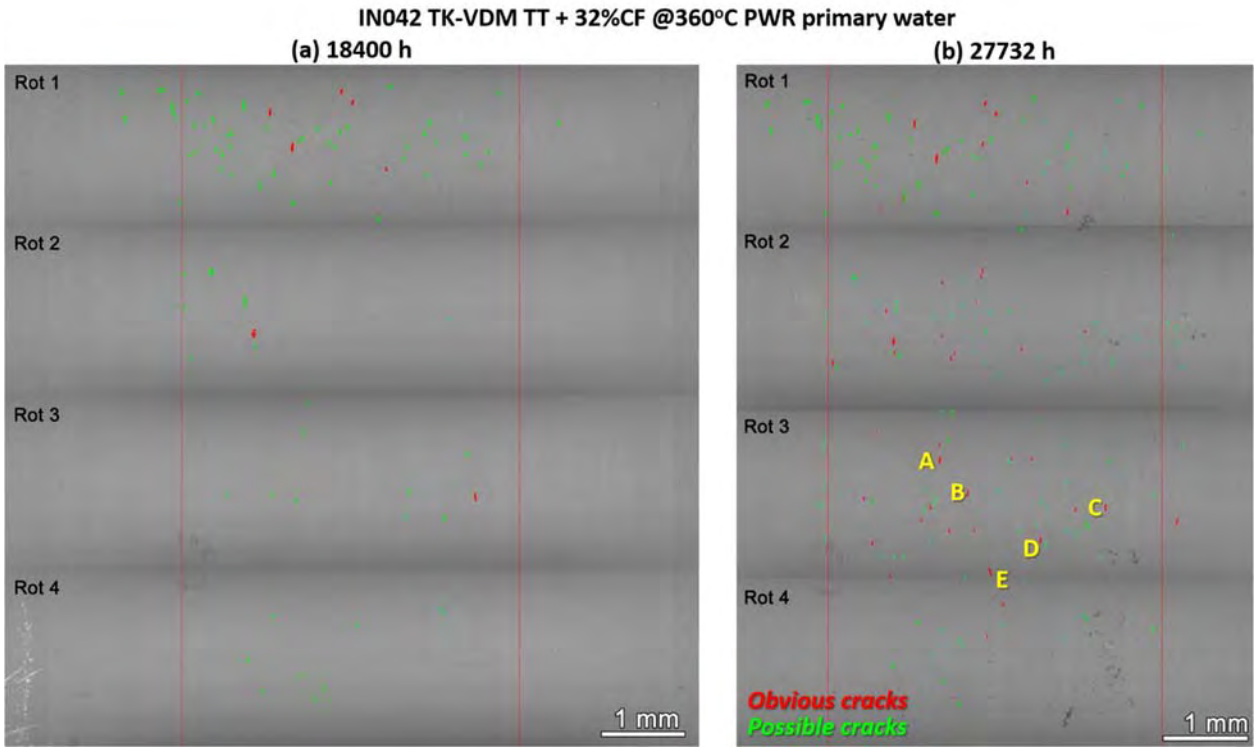

Figure 11. SEM-BSE montage images of the entire gauge surface and part of the fillet surface after Phase II (left) and Phase III (right) exposure in the 1 µm finish, TT+31.9%CF Alloy 690 TK-VDM plate specimen IN042. Obvious cracks are highlighted in red and possible cracks in green.

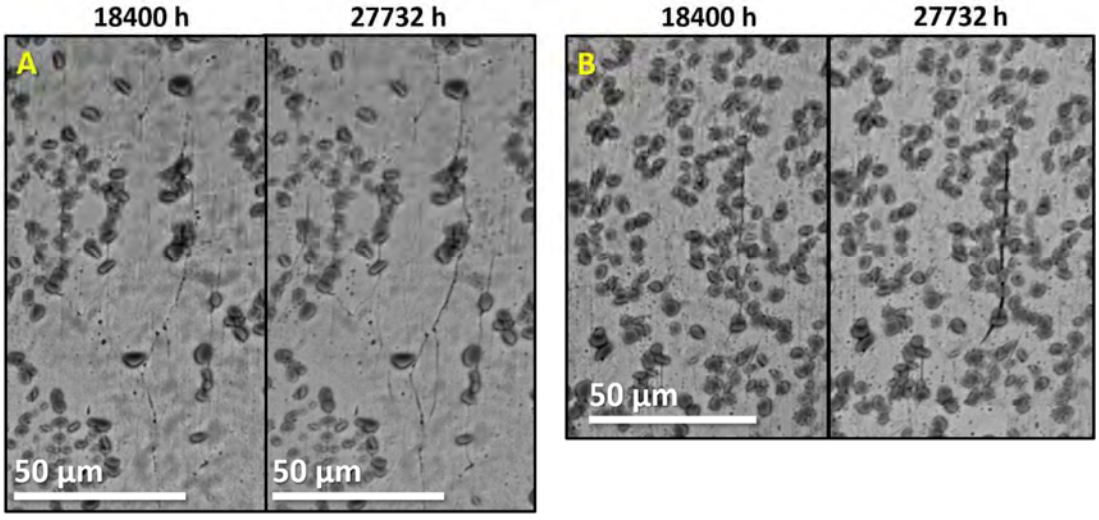

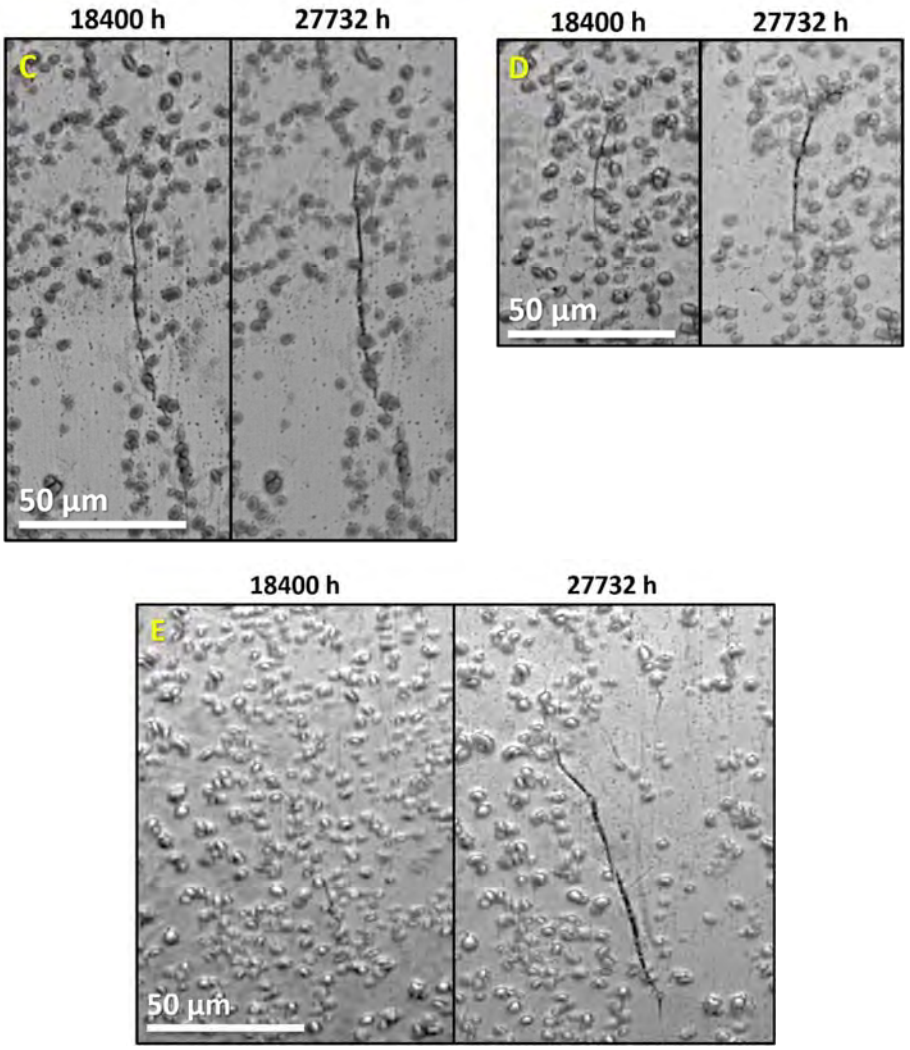

Figure 12. Higher magnification SEM-BSE images on crack evolution at sites A–E identified in Figure 11 after Phase II and III exposure in the 1 µm finish, TT+31.9%CF Alloy 690 TK-VDM plate specimen IN042.

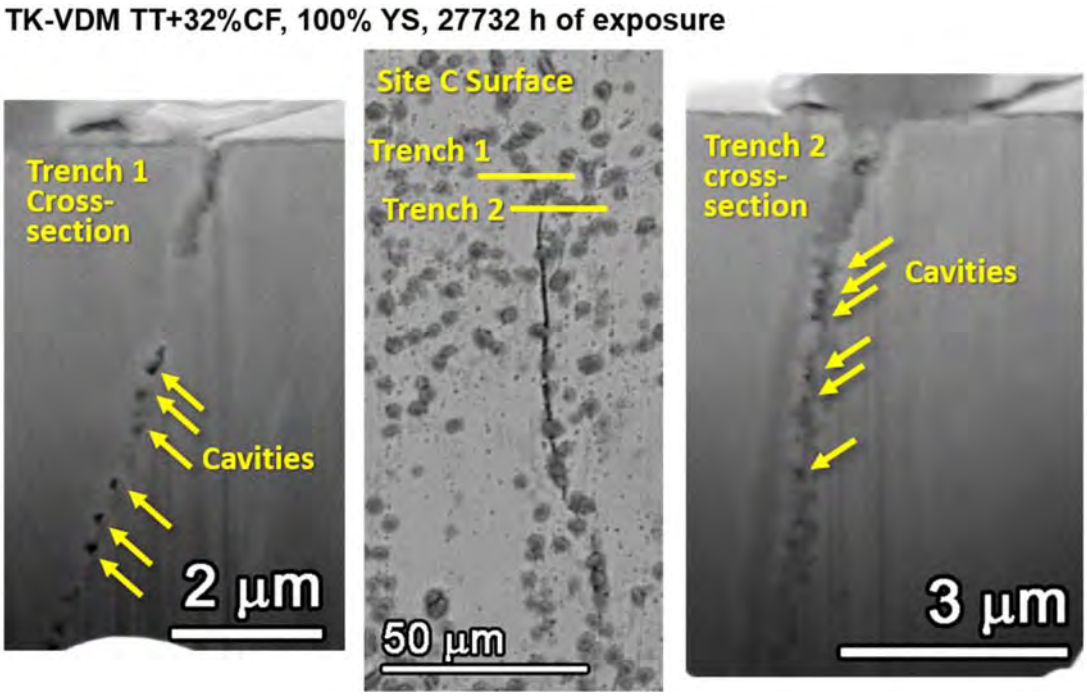

Figure 13. Low-kV FIB-SE images of the sub-surface cross-section morphology of FIB trenches (left and right) intersecting a surface crack at site C as identified in the middle SEM-BSE image after Phase III exposure in the 1 µm finish, TT+31.9%CF Alloy 690 TK-VDM plate specimen IN042.

Among the first batch of highly CW Alloy 690TT specimens tested since Phase I, the TT+31%CF Doosan CRDM specimen IN030 is the only other TT specimen in highly CW condition that remains in test beside IN042. However, this TT material features GB carbides 5-100X larger than those in the other three TT materials that also are generally 5X+ more widely apart. This has led to much fewer cracks observed in the surface and little evolution was seen between Phase II and Phase III exposure, therefore the overview image is not displayed here. However, a number of selected sites were documented by SEM at high magnifications after each test phase enabling a direct comparison of the morphological evolution of features of interest. As presented in Figure 14, minor changes were observed on the precursor damage observed on the surface of this specimens from Phase II to Phase III exposure. Both Sites 1 and 2 features discrete nano-sized voids decorating high-energy GBs like perforation holes in the postage stamps that have been demonstrated to be cavities intersecting the surface likely due to permanent damage produced during cold work. After being exposed at high stress for ~27,840 hours, some of these features exhibited little change as shown at Site 1, but in some regions IG "attack" seem to have taken place linking these discrete features into continuous network as shown at Site 2. In addition, possible cracks were also spotted in the specimen with darker, continuous contrast along certain GBs. To examine its sub-surface morphology, FIB trenching and serial milling was again performed on selected cracks with an example shown in Figure 15. A crack-like feature of ~40 µm long on the surface was trenched on one end and the cross-section revealed very limited IG penetration of only ~20 nm deep. The distribution and size of GB cavities appear to be commensurate with what was observed prior to testing, suggesting little growth had taken place over the entire duration of high temperature exposure at yield stress.

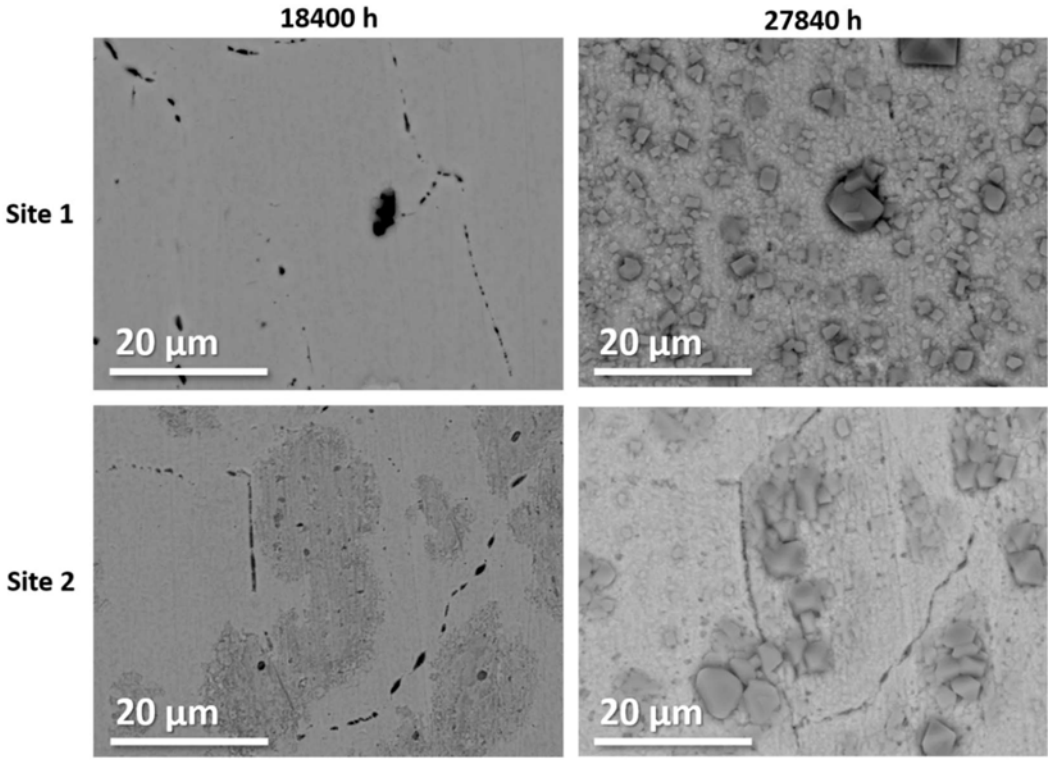

Figure 14. SEM-BSE images of the typical surface morphology examined at the same sites after Phase II (left) and Phase III (right) exposure in the 1 µm finish, TT+31%CF Alloy 690 Doosan CRDM specimen IN039.

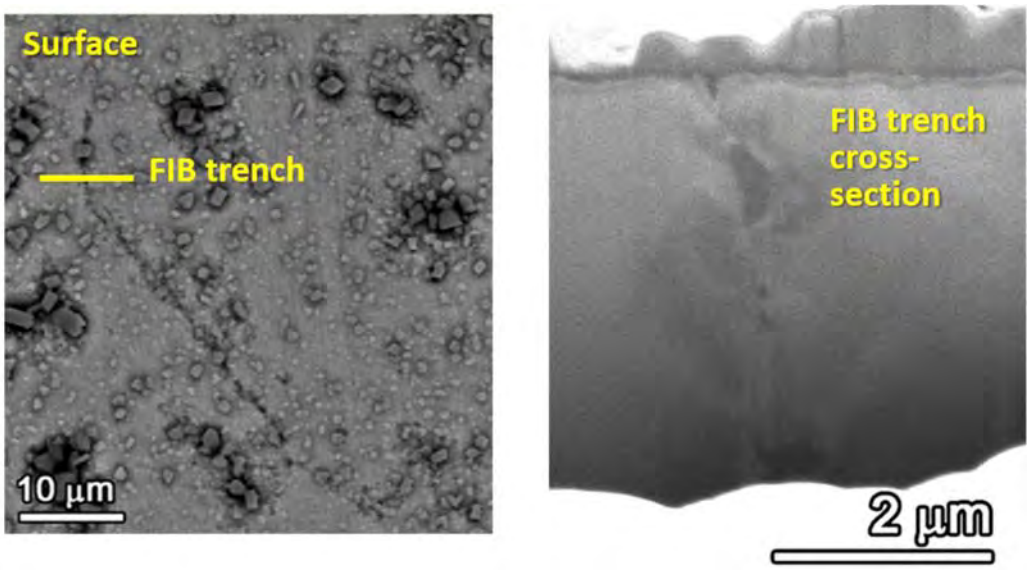

Figure 15. SEM-BSE image of a crack-like feature observed on the gauge surface of the 1 µm finish, TT+31%CF Alloy 690 Doosan CRDM specimen IN039 after 27,840 hours of exposure (left) and a low-kV FIB-SE image of the sub-surface cross-section morphology of a FIB trench intersecting the crack-like feature as identified in the left image (right).

The completion of Phase III test also marked ~2.1 years total exposure in 360°C simulated PWR primary water for the first batch of replacement specimens. Among them were the same TT+31%CF Sumitomo and Valinox CRDM materials that exhibited high susceptibility to crack initiation loaded at 100% YS, but these replacement specimens have been loaded at 90% YS to investigate the effect of applied stress on GB cavity and crack formation. As shown in Figure 16a, the TT+31%CF Sumitomo and Valinox CRDM specimens loaded at 100% YS already showed obvious crack formation on the gauge surface and a high density of GB cavities in the cross-section by 1-year exposure. In comparison, specimens with the same material condition with a lower applied stress at 90% YS exhibited little evidence of crack formation or increased density of GB cavities except the common "postage stamp" features along high-energy GBs (Figure 16b). Another interesting replacement specimen to note is the solution annealed (SA)+31%CF Valinox CRDM specimen loaded at 100% YS. The solution annealing removed GB carbides, enabling a direct comparison on the crack initiation behavior between high density of GB carbides vs. no GB carbide microstructures. As shown in Figure 17, after ~2.1 years of exposure in 360°C simulated PWR primary water, only sporadic, minor IG damage was observed in the SA+31%CF specimen loaded at 100% YS, of which the depth remained extremely shallow within a few tens of nanometers.

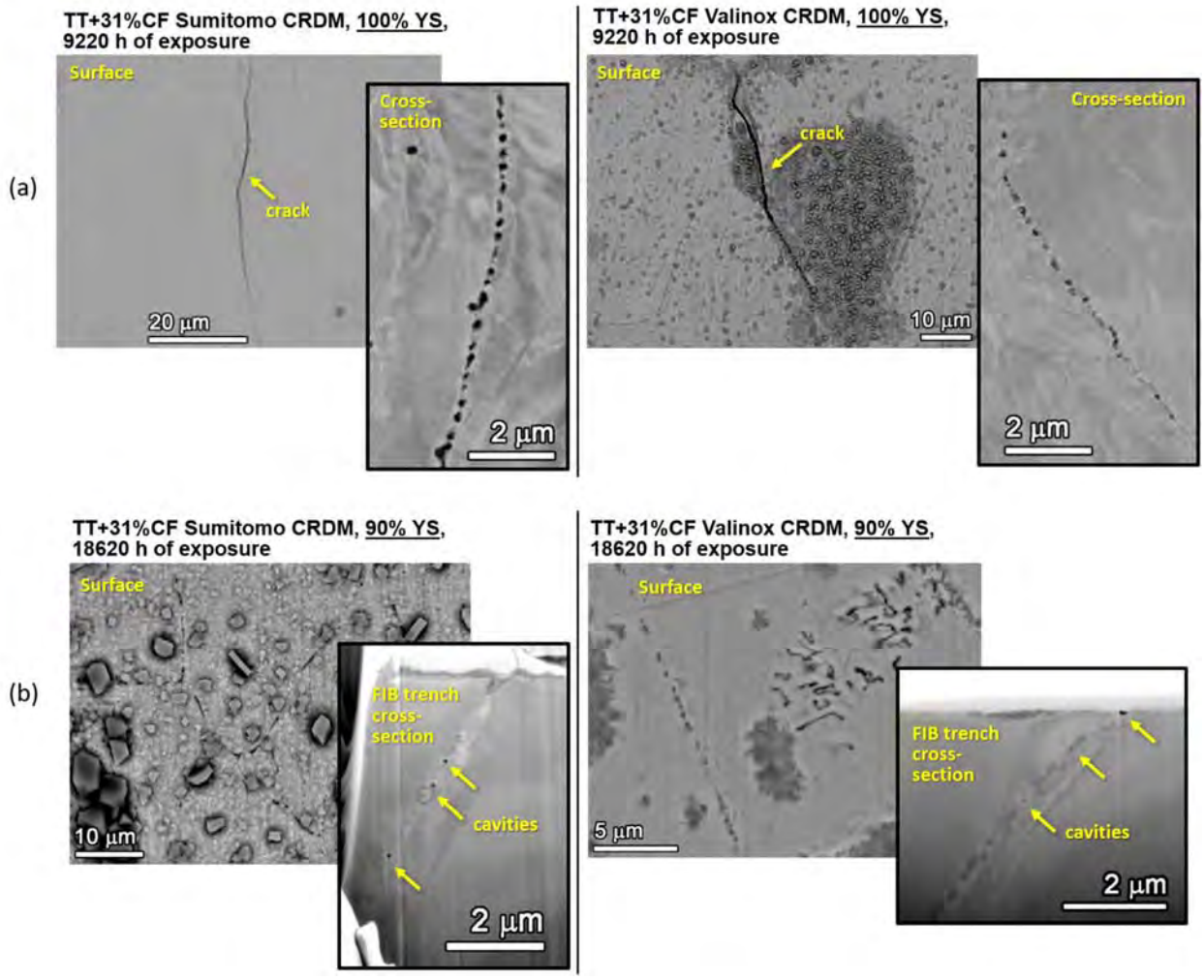

Figure 16. Representative damage features on the surface and in the cross-section of the TT+31%CF Sumitomo and Valinox CRDM specimens exposed to 360°C simulated PWR primary water (a) at 100% YS for 9,220 hours and (b) at 90% YS for 18,620 hours.

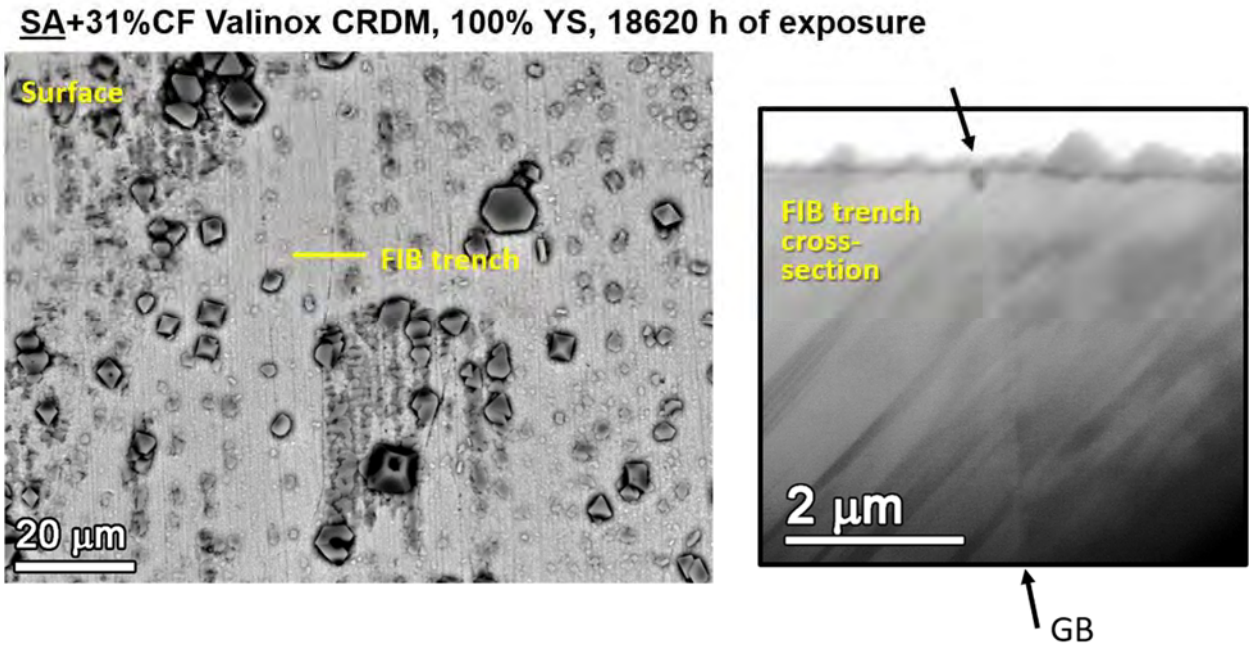

Figure 17. Representative damage features on the surface and in the cross-section of the SA+31%CF Valinox CRDM specimens exposed to 360°C simulated PWR primary water at 100% YS for 18,620 hours.

Precursor Damage Evolution in Moderately CW Alloy 690TT Materials

Unlike in most of the TT+31%CF specimens where obvious cracks can be easily identified in low-magnification SEM-BSE montage images of the gauge surface, the highly polished TT+21%CF specimens exhibit more subtle damage features that can only be resolved under high resolution examination at higher magnifications even after ~3.1 years (Phase III) of exposure. Therefore, additional close-up SEM examinations were routinely performed at the same randomly selected sites in these specimens after each test interruption. This enabled direct assessment of the evolution of precursor damage with examples shown for the TT+21%CF specimens from the three Alloy 690TT CRDM heats Sumitomo (Figure 18), Valinox (Figure 19), and Doosan (Figure 20). All three specimens exhibit "postage stamp" features along most high-energy GBs after Phase II exposure. As reported in an earlier milestone report [1], these features have been shown to be associated with discrete cavities intersecting the surface using serial FIB trenching. After Phase III exposure, these postage stamp features on the high-energy GBs have started to link up and appear to be forming more continuous IG damage on certain GBs in the TT+21%CF Sumitomo and Valinox materials with closely spaced nanometer-sized carbides (Figures 18 and 19). In comparison, little evolution of the postage stamp features was found in the TT+21%CF Doosan material having larger carbides that are more widely spaced (Figure 20).

Interestingly, the most obvious surface cracks have been identified on the TT+21%CF TK-VDM Plate specimen IN060 after Phase III exposure, where some IG cracks were readily identifiable in the low-magnification SEM-BSE montage images on the gauge surface. The details will be presented in the next section along with cross-section examination performed by serial FIB trenching of the cracks.

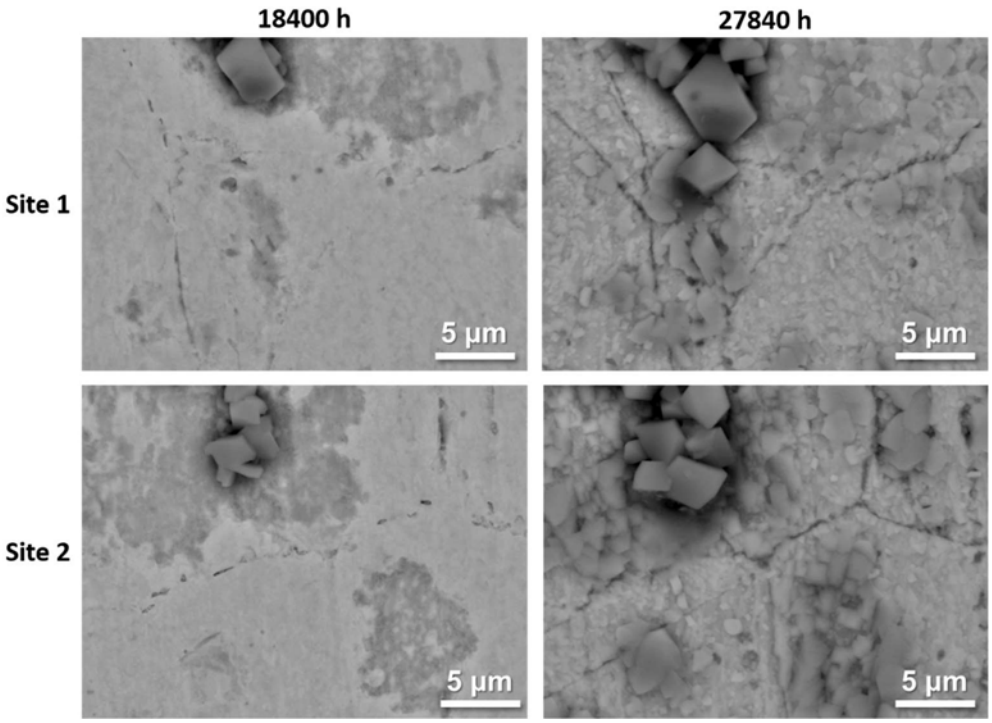

Figure 18. SEM-BSE images of the typical surface morphology examined at the same sites after Phase II (left) and Phase III (right) exposure in the 1 µm finish, TT+21%CF Alloy 690 Sumitomo CRDM specimen IN024.

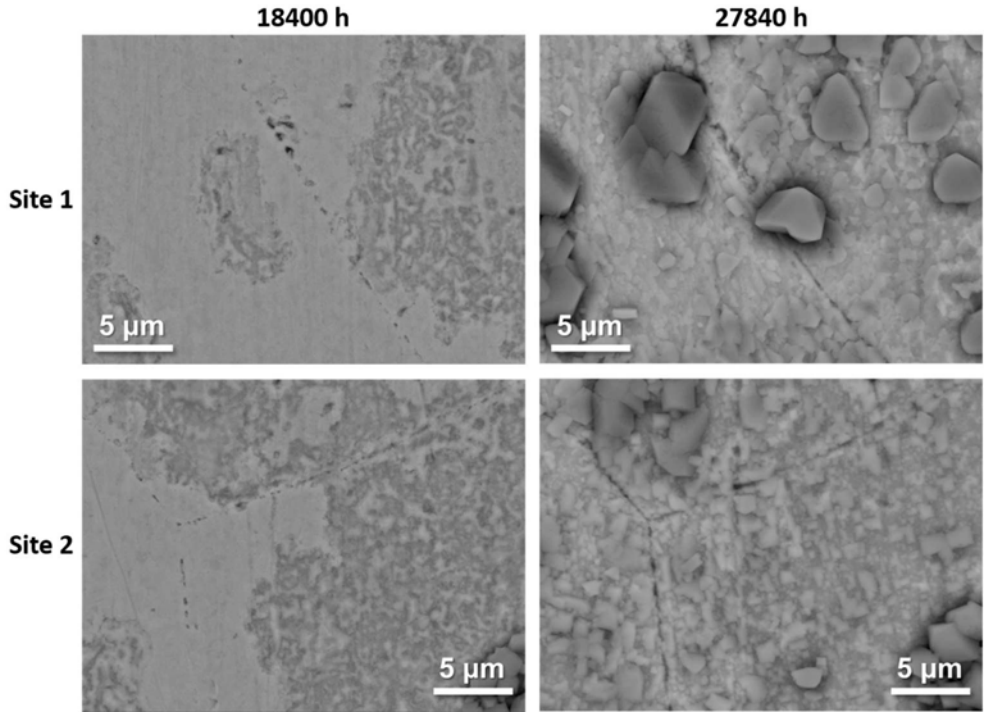

Figure 19. SEM-BSE images of the typical surface morphology examined at the same sites after Phase II (left) and Phase III (right) exposure in the 1 µm finish, TT+21%CF Alloy 690 Valinox CRDM specimen IN027.

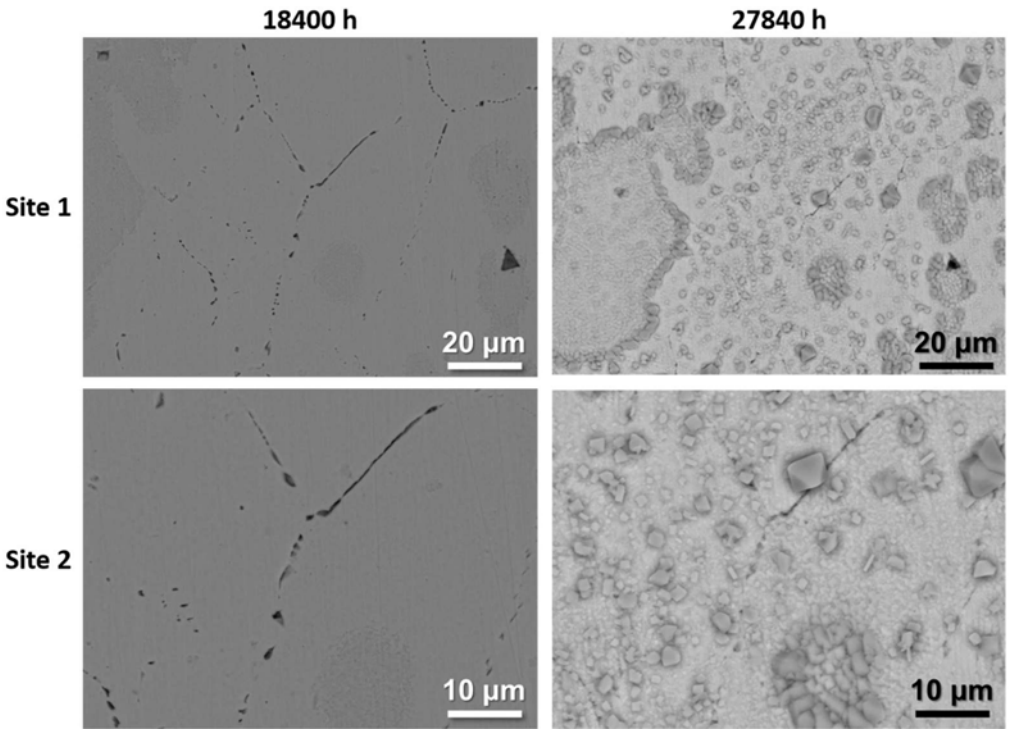

Figure 20. SEM-BSE images of the typical surface morphology examined at the same sites after Phase II (left) and Phase III (right) exposure in the 1 µm finish, TT+21%CF Alloy 690 Doosan CRDM specimen IN030.

One specimen from each of the three TT+21%CF Alloy 690 CRDM materials were removed after Phase II for cross-section examinations throughout the thickness of the entire gauge section with results shown in Figure 21. A slight increase in GB cavity aggregations was observed in the TT+21%CF Sumitomo CRDM material. However, rather than formation of new GB cavities, this is likely due to the increase in the size of existing cavities making them observable in the low-resolution montage images (Figure 21a). As for the 21%CF specimens from the Valinox and Doosan CRDM heats, GB cavities were sporadically evidenced at higher magnifications, but their size and density were too low to be identified in the montage maps (Figures 21b and c). This indicates a much lower kinetics of GB cavity formation and growth in the 21%CW Alloy 690 materials even after extended testing in 360ºC simulated PWR primary water. Quantification similar to what has been done on the TT+31%CF Valinox and Doosan specimens is undergoing for the same two materials at 21%CF condition and the results will be reported in near future.

Since there is only one original TT+21%CF specimen from each heat still remaining in test after Phase III exposure, decision was made to only employ non-destructive serial FIB trenching in the specimens to get an idea of the distribution of GB cavity in the bulk. At least 2–3 GBs were investigated in each specimen which all exhibited consistent morphology with representative results shown in Figure 22for the Valinox CRDM specimen IN027 and in Figure 23 for the Doosan CRDM specimen. Very shallow IG damage right beneath the surface with a depth of a few hundreds of nanometers were observed in both specimens, but the Valinox CRDM specimen appears to have a higher density of GB cavities than the Doosan CRDM specimen, which can again be associated with the difference in their GB carbide distributions.

Somewhat surprisingly, crack nucleation was identified in the TT+21%CR TK-VDM plate specimen IN060 after Phase III exposure. The rotation of the specimen exhibiting the highest density of IG cracks is presented in Figure 24a with zoom-in images (Figure 24b) showing more detailed surface morphology of two selected cracks, one relatively long (surface length ~100 µm) and one very short (surface length

<30 µm). Serial FIB trenching was performed on these two cracks starting from region outside the crack tip to opened portion of the crack. The sub-surface morphology of the trenches revealed small, closely spaced GB cavities leading at the crack tips (Figure 24c). This again confirmed the important role of GB creep cavities on IG crack nucleation.

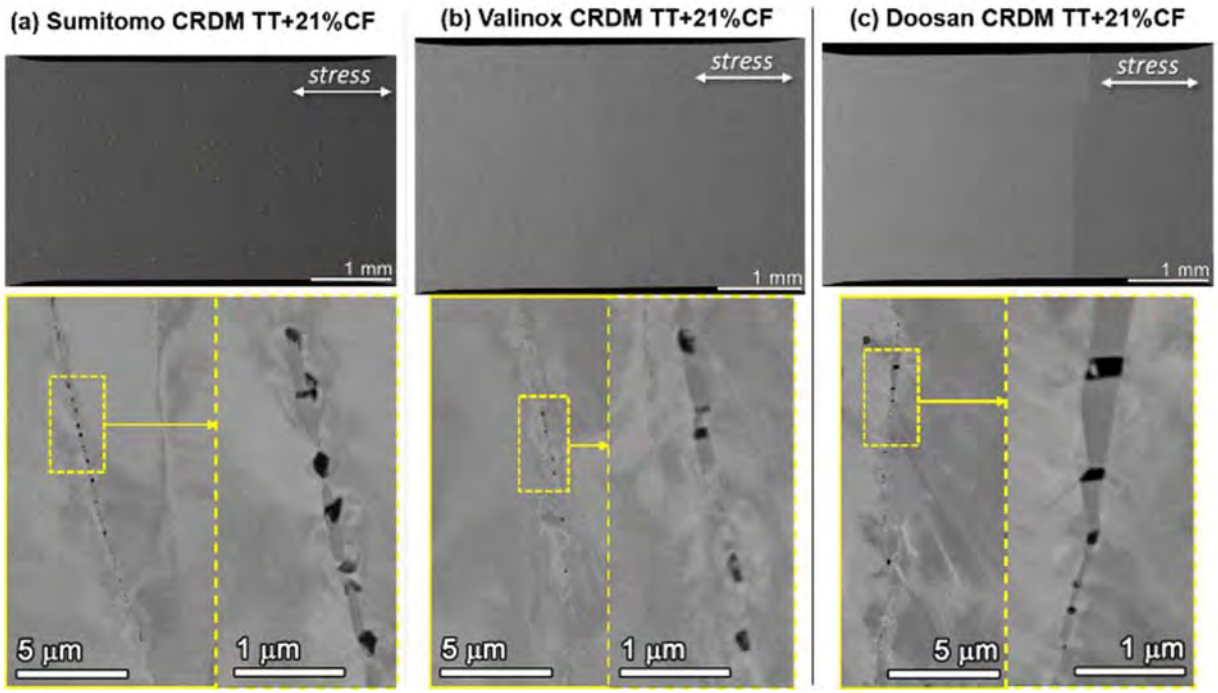

Figure 21. SEM-BSE montage images of the gauge cross-section with higher magnification images on the typical morphology of GB cavity aggregation after Phase II exposure in the ground finish, TT+21%CF Alloy 690 CRDM specimens (a) Sumitomo IN025, (b) Valinox IN028, and (c) Doosan IN031.

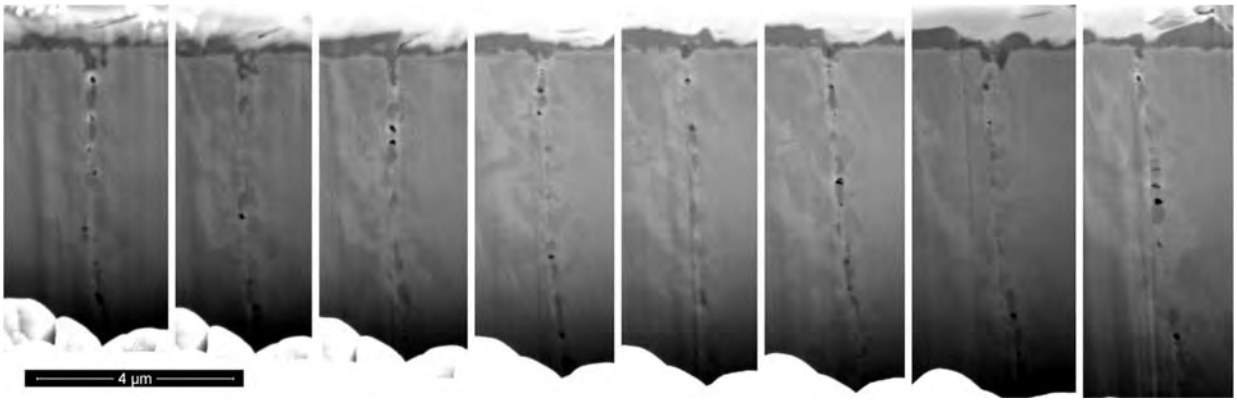

Figure 22. Low-kV FIB-SE image of GB cavities revealed by serial FIB trenching in the 1 µm finish, TT+21%CF Valinox CRDM specimen IN027 tested at yield stress after 27,840 hours of exposure in 360ºC simulated PWR primary water.

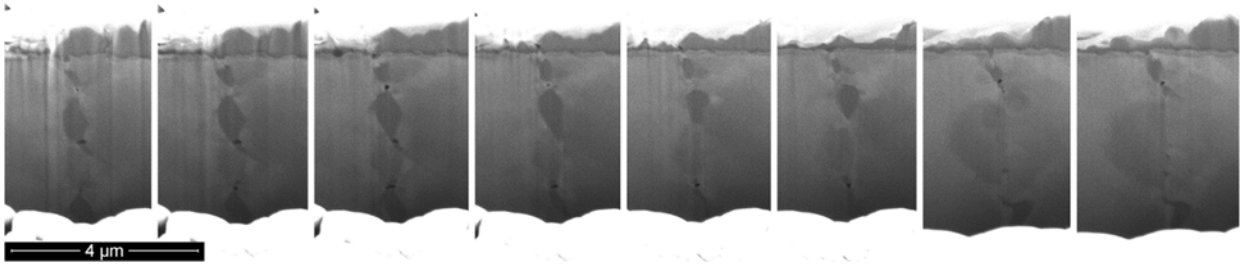

Figure 23. Low-kV FIB-SE image of GB cavities revealed by serial FIB trenching in the 1 µm finish, TT+21.6%CF Doosan CRDM specimen IN030 tested at yield stress after 27,840 hours of exposure in 360°C simulated PWR primary water.

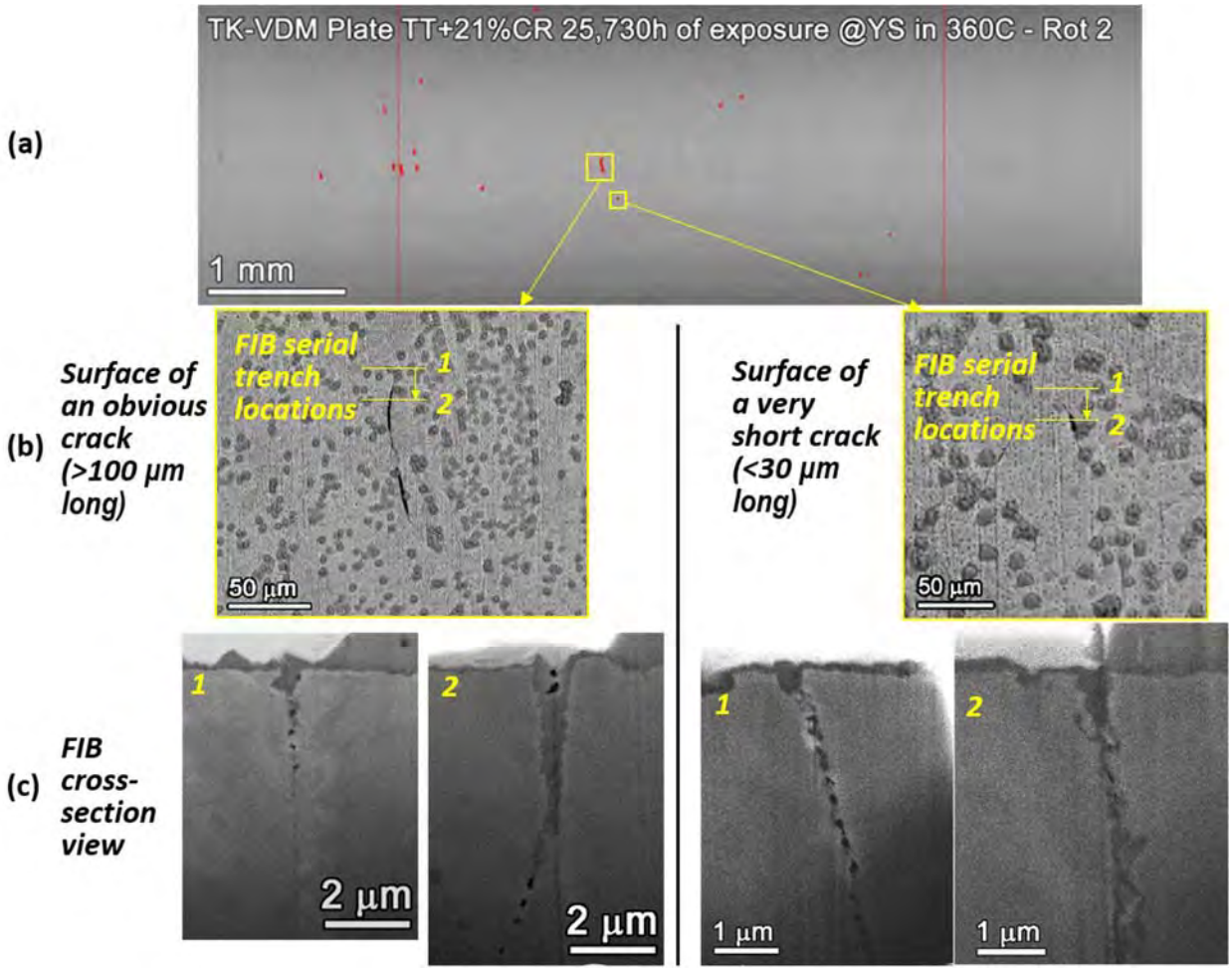

Figure 24. SEM-BSE montage images (a) of one rotation of the TT+21%CR Alloy 690 TK-VDM Plate specimen IN060 after Phase III (25,730 hours) exposure. Higher magnification SEM-BSE images of the surface morphology of identified cracks (b) and FIB-SE images of the cross-section of the cracks (c) are also shown.

Update on GB Cavity Quantification after Phase I and Phase II Exposure

As reported in the September 2019 milestone report [3], quantification has been performed on the TT+31%CF Valinox and Doosan CRDM specimens to evaluate GB cavity evolution with increase in exposure time and applied stress. These two materials exhibit a similar grain size but very different GB carbide morphologies, enabling a direct comparison on the effect of starting GB microstructure. Results are presented in terms of cavity density and cavity coverage per unit GB length as shown in Figures 25 and 26, respectively. The TT+31%CF Doosan CRDM material exhibits an average of one carbide per every 2-2.5 μm along GBs throughout the specimen. The percentage of GB length containing cavities remained constant at ~5% regardless of test time and applied stress. These results suggest that formation of new cavities has not occurred nor has significant growth of existing cavities taken place in the specimens. In contrast, a large increase in cavity density and cavity coverage at GB was found for the TT+31%CF Valinox CRDM material after Phase II exposure in the gauge section loaded at 100%YS. Meanwhile, the average percentage of cavity coverage at GBs, i.e. decohered fraction of GB has almost doubled in the gauge from ~15% to ~25%, and for some GBs it reached as high as ~37%. It should be noted that cracked portion of the GBs observed in the gauge section were excluded from quantification, therefore the actual value of these two parameters at 100% YS are even higher. The effect of applied stress also started to pick up as testing time proceeds. After Phase I exposure, the GB cavity density and coverage were relatively low until reaching 100% YS, but the increasing trend has become clear starting from ~70% YS after Phase II exposure. Nevertheless, the absolute values are still much lower in comparison to those at 100% YS.

To facilitate the prediction of long-term degradation behavior of service materials, quantification has expanded this fiscal year to investigate materials with lower cold work levels. The same Alloy 690TT Valinox and Doosan materials were investigated, this time in specimens at moderate cold work levels of 21% in the gauge center (at 100% YS) and the reference shoulder region (at ~15% YS). The new results are plotted in red symbols together with the corresponding TT+31%CF data for cavity density in Figure 25 and for GB cavity coverage in Figure 26. Consistent with the qualitative cross-section observations, the TT+21%CF specimens from both the Valinox and Doosan CRDM heats exhibited a lower cavity density and GB coverage than their 31%CF counterparts after the first 1.1 year of exposure. With the exposure time increased to ~2.1 years, the cavity density and GB coverage also increased slightly in both the 15% and 100% YS region in the TT+21%CF Valinox CRDM specimen with actual values reaching the pre-test distribution in its 31%CF counterpart. However, no significant increase in cavity distribution was observed with increase in applied stress from low load to yield stress. In the TT+21%CF Doosan CRDM specimen, the cavity density and GB coverage increase slightly in the low load region but decreased in the highly stressed gauge region. While this is probably due to data scatters, the result indicates in general, little change had occurred in GB cavity distribution over time in this material featuring larger GB carbides with wider spacings.

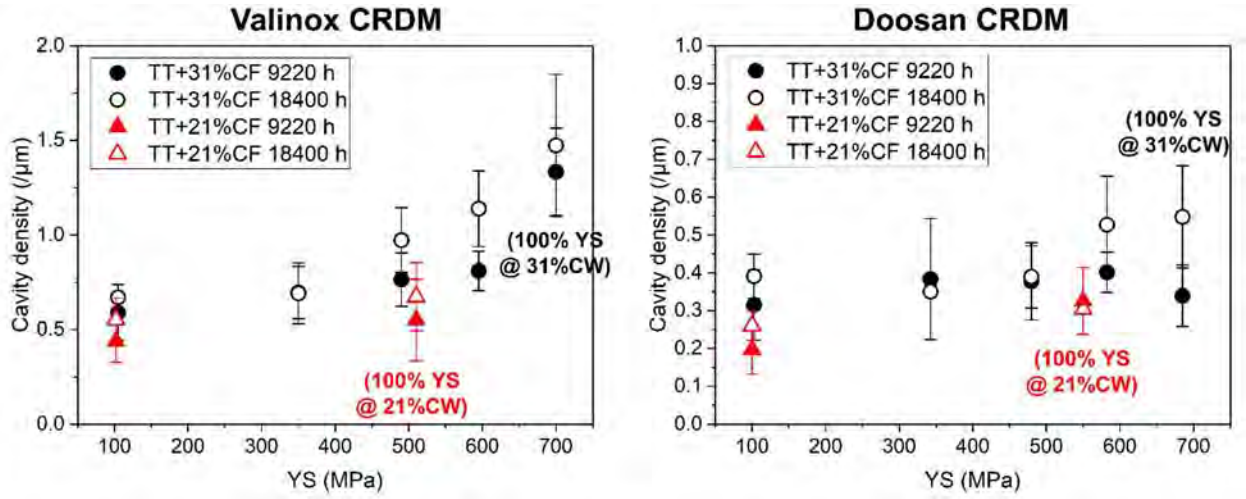

Figure 25. Quantification on cavity density evolution after Phase I and Phase II exposures as a function of applied stress in (a) 21% and 31%CF Alloy 690TT Valinox CRDM and (b) 21% and 31%CF Alloy 690TT Doosan CRDM SCC initiation specimens.

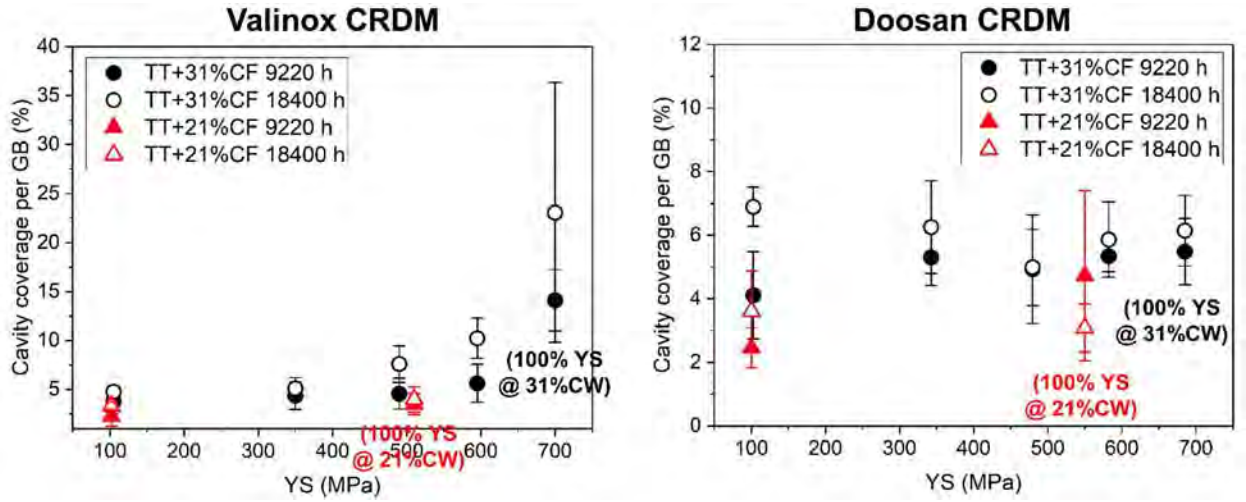

Figure 26. Quantification on GB cavity coverage evolution after Phase I and Phase II exposures as a function of applied stress in (a) 21% and 31%CF Alloy 690TT Valinox CRDM and (b) 21% and 31%CF Alloy 690TT Doosan CRDM SCC initiation specimens.

LONG-TERM CRACK INITIATION BEHAVIOR OF ALLOY 152/52 IN PWR PRIMARY WATER

Chapter Overview

Ductility dip cracking (DDC) is recognized as a significant issue during welding of high-Cr, Ni-based alloys. IG cracks are often produced in Ni-30Cr weld metals and may require weld repair. A critical question is whether the presence of pre-existing defects can promote SCC initiation and growth in service. To answer this question, LWRS has been collaborating with an NRC project at PNNL to perform SCC initiation test on selected weld materials. Two blunt notch compact tension (BNCT) specimens were machined from two EPRI mockups where DDC cracks were identified in Alloy 52M weld metal. Notch surfaces of these two specimens were specially prepared and highly polished to intersect pre-existing IG cracks in the weld metal. Constant load SCC tests have been conducted for up to 16,000 hours at high stress in 360°C simulated PWR primary water. The crack evolution on the notch surfaces was recorded every ~4,000 hours, and a thin slice was taken off after 3,810 and 16,000 hours of exposure for detailed cross-section examination on weld cracks intersecting or near the surface. New small cracks were observed on the blunt notch surface for one weld specimen after 3,810 hours. Only minor growth of a few pre-existing IG cracks was documented on the surface after 8,000 hours. No obvious change was found after 12000 hours of exposure. The load was increased by 5% twice at 13,000 and 15,000 hours, but the most recent observation after 16,000 hours of exposure still did not reveal any change in surface crack morphology. The other weld specimen showed very little evidence of new crack formation or growth of pre-existing cracks throughout the entire exposure.

Experimental Procedures

Blunt Notch Compact Tension Test on Alloy 52M Welds

Specimen Preparation

While CLT test provides an efficient way to assess the effects of various influencing factors on SCC initiation by testing a large number of specimens simultaneously, BNCT test has been selected for this study as it enables specimens to be prepared in a site-specific fashion with the notch positioned in region(s) of interest. As shown in Figure 27, standard 0.5T CT specimen geometry is used, but the notch tip was wet ground to a ~0.75 mm radius using a diamond wheel. The notch surface was then manually polished to a 1 μm finish. This created a well-controlled surface closely matching the surface condition for the CLT specimens. Crack initiation can be better resolved by SEM examinations of the notch for the polished surface and compared to in-situ DCPD measurements.

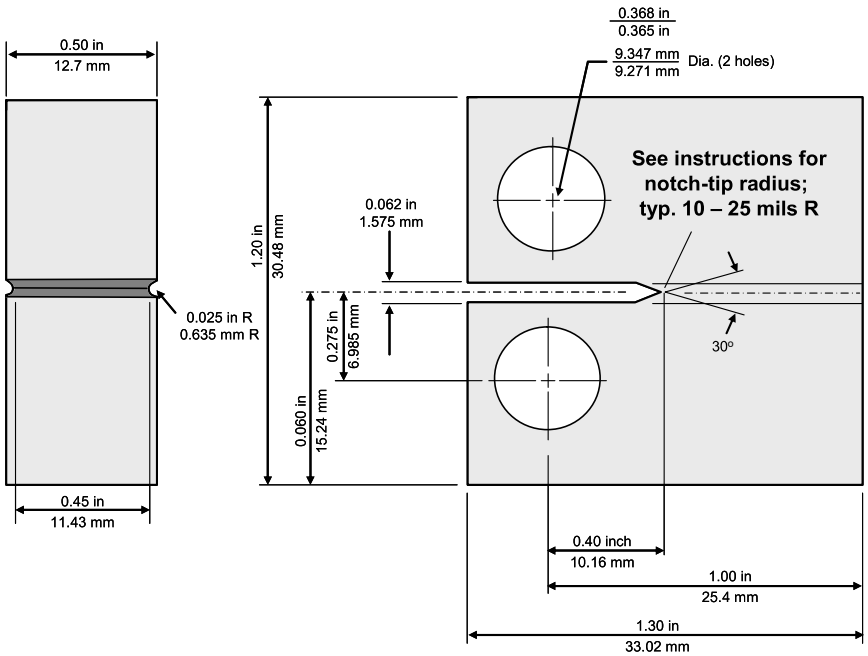

Figure 27. Dimensions of the 0.5T BNCT specimen. The notch radius is ~0.75mm for all specimens.

Two blunt-notch CT specimens were prepared from two dissimilar metal weld mockups made by EPRI to specifically introduce DDC in Alloy 52M. CT148 is machined from an EPRI WRTC 316L/52M/152/low alloy steel (LAS) V-groove weld and CT149 is from an EPRI Alloy 52M mockup. Prior to the test, the distribution of DDC in both welds were carefully mapped in SEM to facilitate determination of the notch location. The EPRI WRTC Alloy 52M-316L weld exhibited a high density of IG cracks in the Alloy 52M weld metal near the Alloy 152 interface, where the notch of CT148 is located (Figure 28). As presented in Figure 28b, a number of DDC cracks greater than 1 mm in length within ~0.5 mm of the Alloy 152 interface were seen in this region and the notch bottom is positioned in the aim to intersect one of the longest cracks. After the specimen was machined, the side grooves were polished and etched for OM/SEM examinations to verify the notch position. As confirmed in Figure 29, the notch successfully intersected a long crack at its bottom along a solidification grain boundary that aligns well with the anticipated growth direction (i.e. perpendicular to the load direction). In addition, the blunt notch was polished to a 1 μm diamond finish and SEM-BSE imaging was employed to document the initial distribution of cracks on the surface that will be exposed to high-temperature PWR primary water during testing. The presence of IG cracks ~50 μm in length can be seen in many regions on the CT148 blunt notch surface with several regions revealing cracks >100 μm in length (Figures 30 and 31). The hope is that these can be effectively located and characterized after long-term testing to determine whether any additional cracking has occurred.

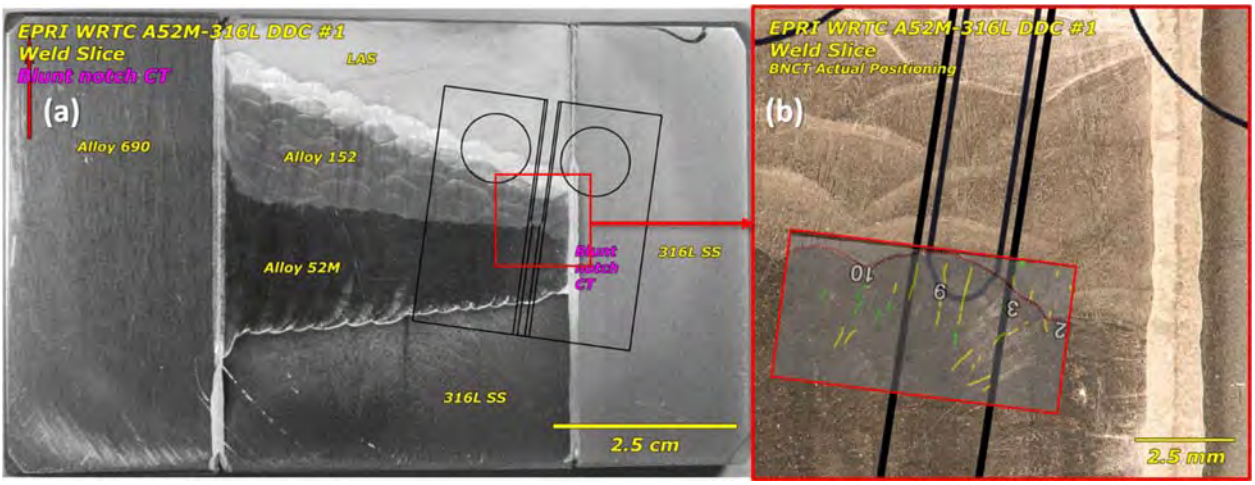

Figure 28. (a) Micrograph illustrating the blunt notch position for CT148, the EPRI WRTC 52M-316L V-groove weld with DDC specimen. (b) A zoom-in micrograph of the location of the notch with respect to pre-test SEM characterizations of DDC distributions (obvious cracks marked in yellow and possible cracks marked in green) in this weld.

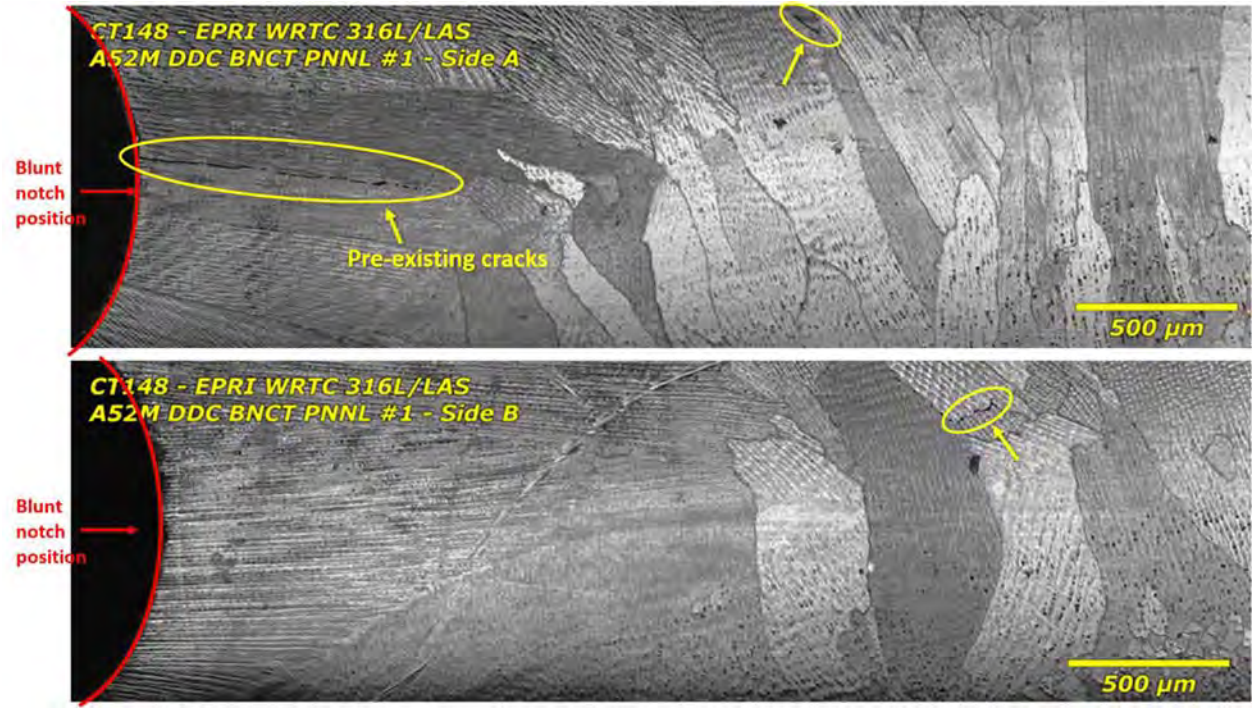

Figure 29. Micrographs revealing cracks identified in the side groove of CT148 just below the notch. The side groove surface was lightly etched for better visualization of solidification grain boundaries.

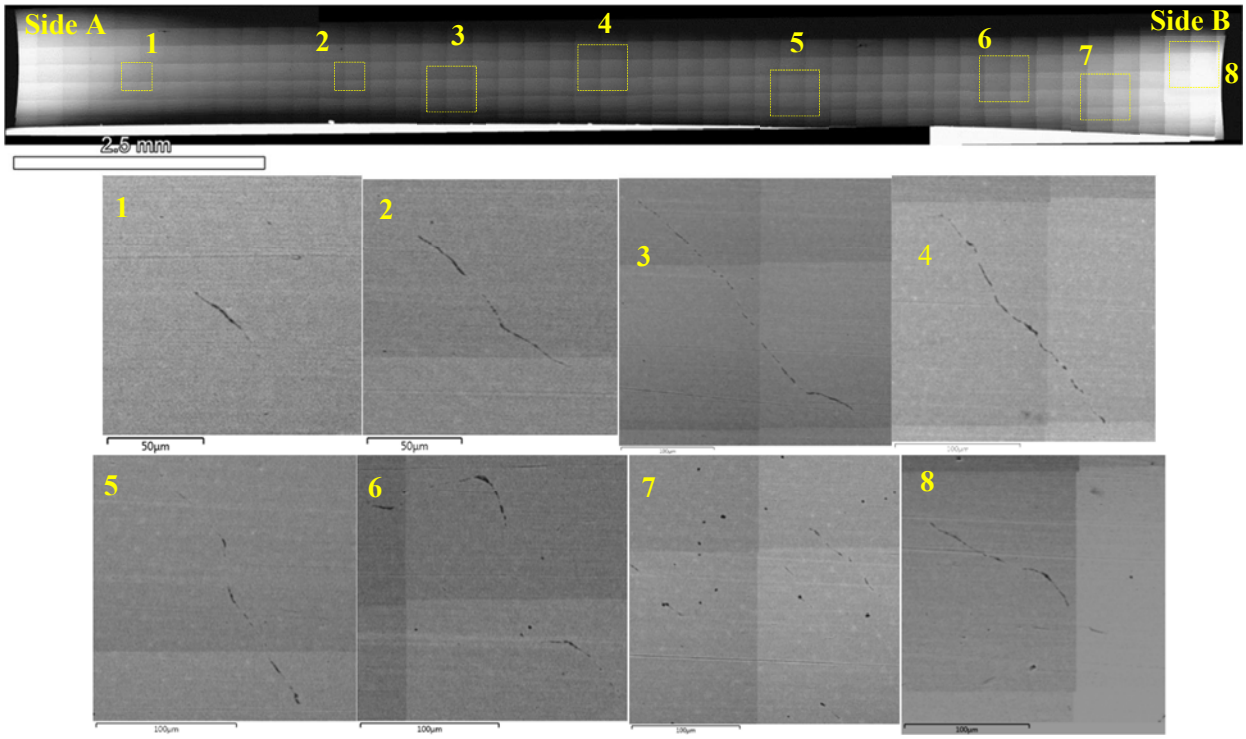

Figure 30. SEM-BSE low magnification montage image of the pre-test blunt notch surface of CT148 with examples of regions containing pre-existing DDC.

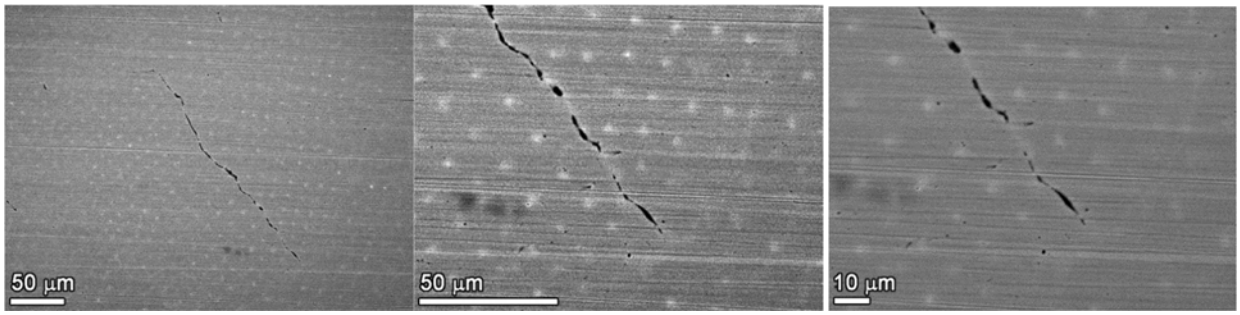

Figure 31. SEM-BSE high magnification micrographs of Region 4 in Figure 30 illustrating the DDC is along a solidification grain boundaries (SGBs). The bright intensity of the Nb signal segregation highlights two different grain orientations on either side of the crack.

The same approach was used to determine the notch position of the EPRI Alloy 52M DDC mockup specimen CT149. The WRTC 52M DDC mockup weld applied refuse passes in an attempt to create DDC cracks and this was partially successful. However, the density and size of these weld cracks were quite small. Several regions were mapped and the maximum number and size of DDC cracks was found within the areas identified by a yellow box overlaid on the upper optical image. As shown in Figure 32, the position of the notch is targeted to intersect the region with the most DDC, but SEM examination on the machined specimen only revealed sporadic and small DDC cracks in the side grooves (Figure 33) and some other possible defects represented by aggregations of dotted precipitates in the blunt notch surface (Figure 34). This illustrates the difficulty in intersecting a meaningful density of small pre-existing defects in this weld. However, since the solidification grain boundaries are properly aligned in the side grooves of the specimens, the decision was made to test this specimen together with CT148.

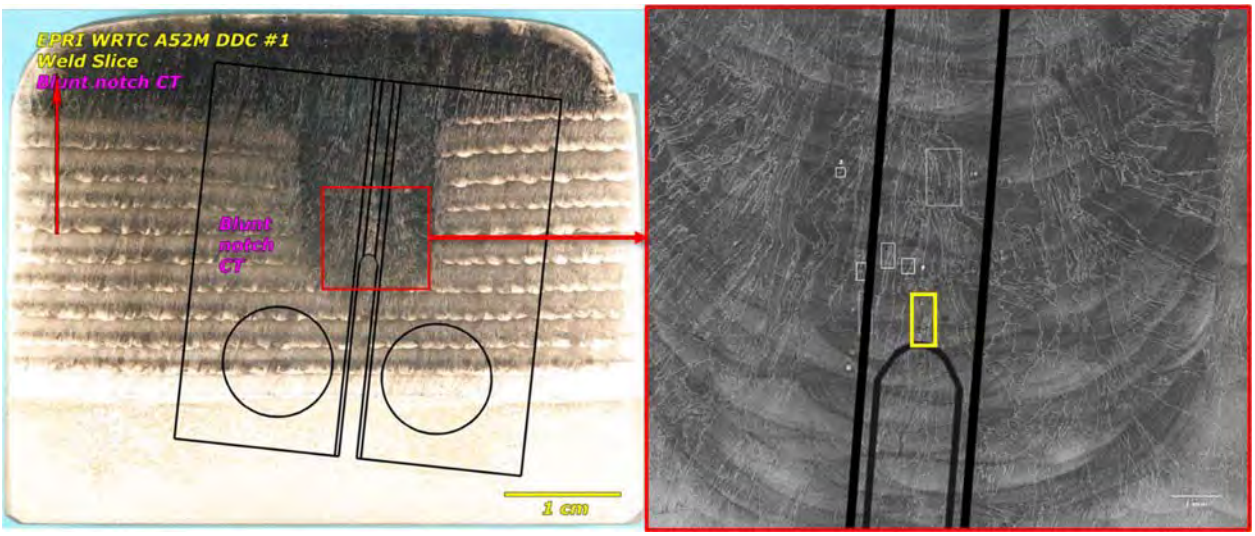

Figure 32. (a) Micrograph illustrating the blunt notch position for CT149, the EPRI WRTC Alloy 52M DDC Mockup specimen. (b) A zoom-in micrograph of the notch location.

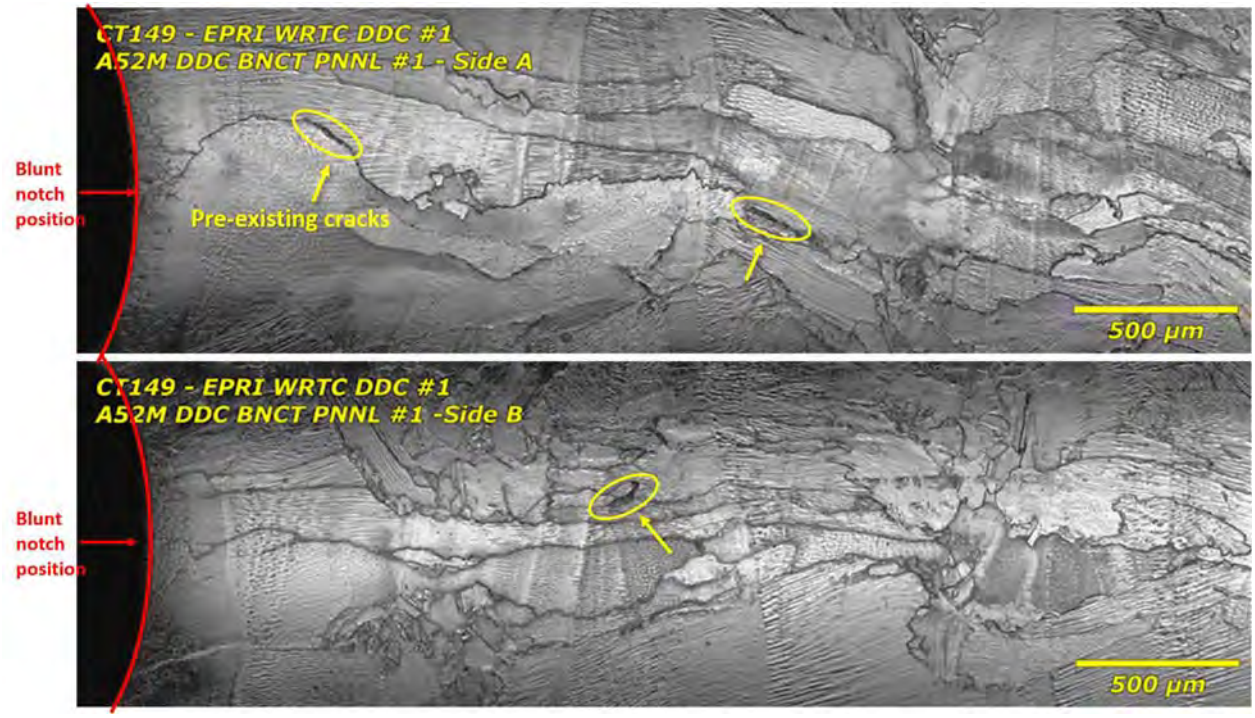

Figure 33. Micrographs revealing cracks identified in the side groove of CT149 just below the notch.

6

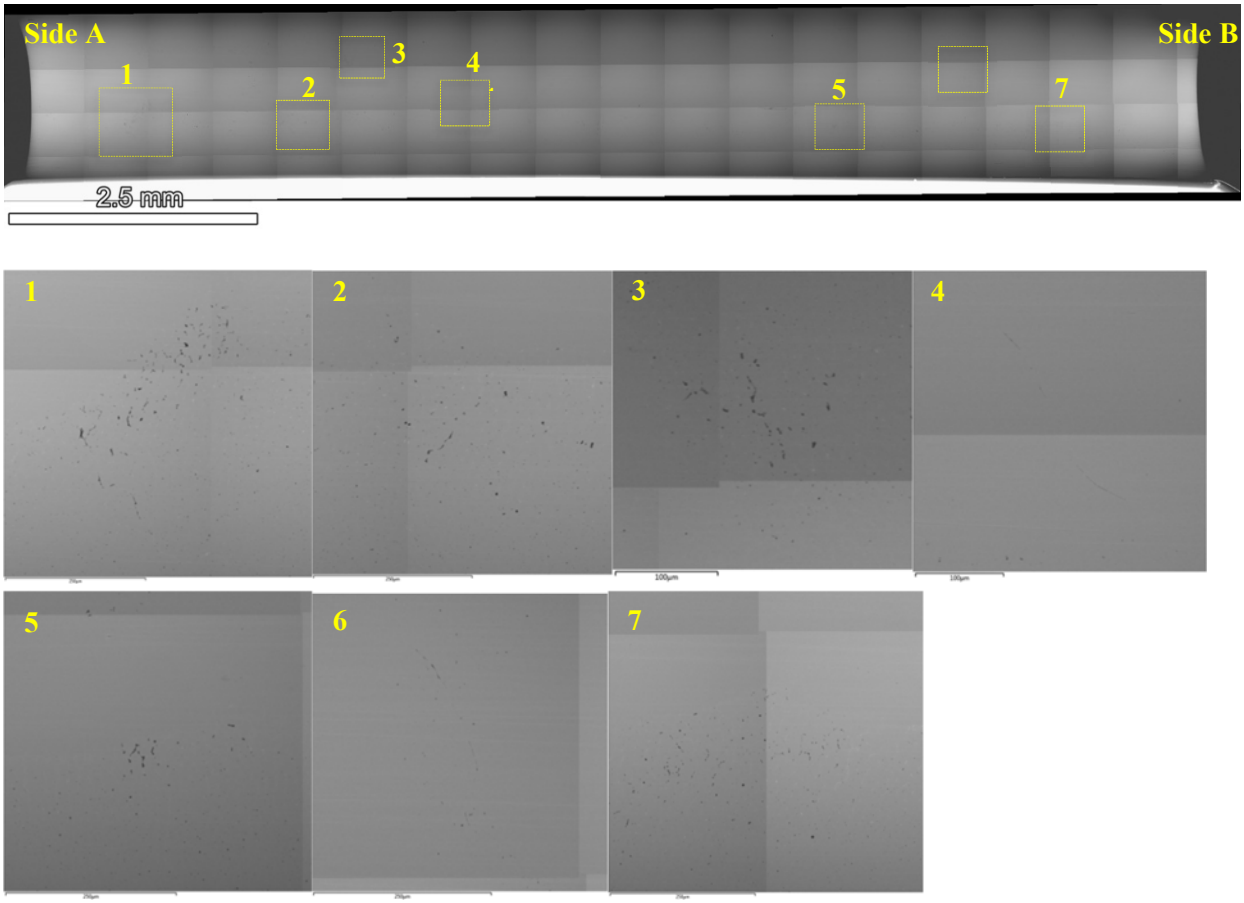

Figure 34. SEM-BSE montage image of the pre-test blunt notch surface of CT149 showing possible regions of pre-existing DDC cracking and defects intersecting the intersecting the surface.

Test Procedure and DCPD Response

The two BNCT specimens were loaded in series in an NRC SCC test system equipped with active load control via a high-precision servo-electric load control system and in-situ monitoring using DCPD. The test environment simulates PWR primary water (1000 ppm of boron, 2 ppm of lithium) at 360°C and 20.4 MPa with a dissolved hydrogen content of 25 cc/kg to maintain a corrosion potential at the Ni/NiO stability line. The test has been conducted at constant load and a high stress intensity (K) level in the attempt to initiate or grow SCC from existing DDC cracks. Since the blunt notch was slightly longer in CT148 to better intersect DDC cracks, the applied load produced a slightly higher estimated K level of ~45 MPa√m in CT148 while the K in CT149 reached ~41 MPa√m. These K levels are better described as a "pseudo K" as they are calculated assuming a tight crack is present across the specimen versus a blunt notch with a smooth surface. The DCPD measurement of crack length is different for the blunt notch specimens because growth from a sharp crack is probably not occurring.

The long-term SCC initiation test has been conducted for a total of ~21.3 months (16,000 hours) and an overview of the DCPD response is presented in Figure 35. There are two major contributors to the change in DCPD response. The first is crack growth since propagation of the crack will change the cross-sectional surface area being monitored and reflected in DCPD as change in electrical resistance. The other is electrical resistivity evolution due to microstructural aging during high temperature exposure. This is a known phenomenon for Ni-base alloys 600/690 and their weld metals, which will lead to decreasing DCPD propagation rate over time. Usually this latter component can be corrected by monitoring the resistivity change in low load region away from the notch where no crack is present, however this is only

applicable to specimen made of uniform material but not specimens containing different materials like these two BNCT specimens machined from dissimilar metal weld mockups. Therefore, only non-referenced DCPD behavior has been tracked in this test. As shown in Figure 35, both specimens showed a decreasing DCPD-indicated propagation rate over the entire test duration which is consistent with the electrical resistivity evolution known for Ni-base weld metals. At ~1380 hours, CT148 exhibited a small step increase in crack length of ~2 μm and then returned to a steady indicated growth rate. The reason for this step increase is unknown but may have resulted from growth and coalescence of the preexisting IG weld cracks since this specimen did have a higher density of larger cracks intersecting the surface (Figure 30). However, no indication of SCC initiation or crack growth were detected by DCPD in either specimen since then. As a result, a decision was made to slightly increase the applied load and see if this has any influence on the DCPD assessment of crack length in the specimens. This was done based on finite element modeling results that predict that a significant decrease will occur in crack-tip K due to creep for a non-growing crack at 360°C, perhaps by as much as 20%. The applied load was increased by 5% at test times of 13,000 and 15,000 hours as identified in Figure 35. A very small immediate increase in the DCPD signal was observed as the load was increased, but there has been no detectable change in the subsequent DCPD response.

To document the evolution of pre-existing defects on the notch surface and to verify DCPD response, the test was stopped every ~4,000 hours for detailed SEM examinations as indicated in Figure 35. In addition, a thin slice was removed from Side B at 3,810 hours and again from Side A at 16,000 hours in both specimens to enable a detailed characterization of crack distribution and morphology in the cross-sections.

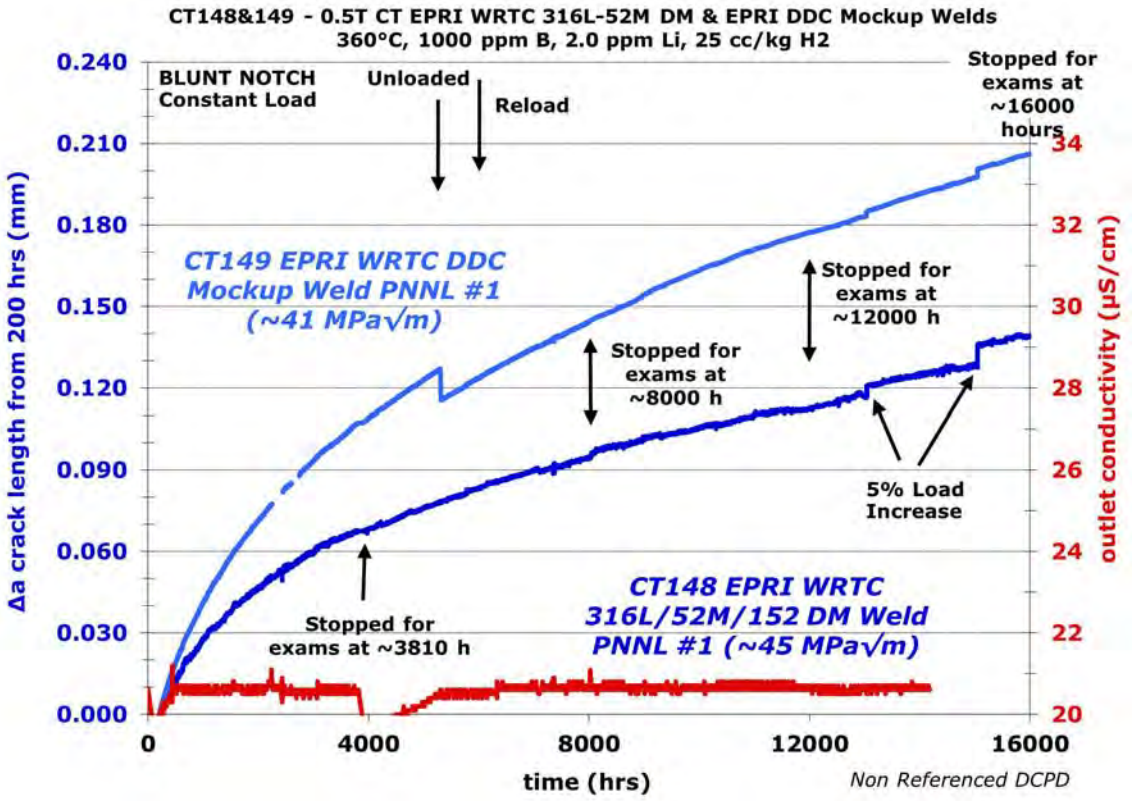

Figure 35. Overview of DCPD response length for the two blunt notch specimens (CT148 and CT149) with preexisting DDC cracks that intersect the notch surface.

Microstructural Characterizations

Microstructural examinations at test interruptions were conducted using a JEOL 7600 SEM. For blunt notch surface examinations, Oxford Aztec software installed in the SEM is used to acquire montages of the entire surface at 350X magnification. Examinations were done in BSE mode at high accelerating voltages (20–30 keV) to observe possible cracking underneath surface corrosion. In this way, morphology and location of DDC cracks and SCC precursors can be quickly documented, enabling evolution of these features to be tracked over time. The same imaging setting was also used to examine the side groove surface to determine the extent of possible cracking along the side groove faces. The slices taken off from sides of the specimens at 3,810 and 16,000 hours were polished to a mirror finish for cross-section examinations. In this case, low-kV (5–7.5keV) imaging is utilized to capture damage characteristics at higher resolution. Iterative polish and SEM examinations were conducted on selected slices to intersect multiple cracks identified on the blunt notch surface to characterize their morphology in the cross-sections. Compositional analyses were also carried out when needed using energy dispersive x-ray spectroscopy (EDS). The EDS data was collected using a 170 mm^2 X-max EDS detector from Oxford Instruments.

Results

Damage Morphology on the Surface of Blunt Notch and Side Grooves

As mentioned above, the two blunt notch specimens were removed from the test every ~4,000 hours for SEM documentation of precursor damage and DDC cracks evolution on the surface of the blunt notch and side grooves. Direct comparison was made at each test interruption to the previous examination and an overview of the evolution of notch surface morphology in CT148 is provided in Figure 36. A number of pre-existing DDC cracks with surface length ranging from ~10–300 μm were observed (marked in green) on the surface prior to testing. However, none of these cracks exhibited obvious growth in length after 3,810 hours of exposure except being opened up a little wider, which is probably due to having been constantly loaded at high stress. This is demonstrated in Figure 37 where higher magnification images of the crack evolution in regions 1 and 2 marked in Figure 36 are provided. Somewhat surprisingly, a distribution of relatively large new IG cracks was discovered with locations highlighted in yellow, among which a few have reached lengths approaching ~0.4 mm. The observation of these new cracks was unexpected and it is not known whether they represent the opening of undetected, pre-existing DDC cracks or result from SCC initiation on the blunt notch surface. In order to better examine these new cracks, a cross-section slice was removed from Side B as shown in Figure 36. The location was selected to have a minor effect on the continued SCC testing of the remaining CT and enable detailed analysis of one of these new cracks. New side groove was machined on Side B after the slice was removed for continued exposure and the notch surface morphology after a total of 8,000 hours exposure can be seen in Figure 36. Again, no obvious growth was observed for existing cracks but many newly formed short cracks were found and highlighted in red. Representative morphology of these short cracks are shown in Figure 37 where they are identified by red arrows with a surface length generally no more than 30 μm. Besides the notch surface examination, SEM characterization was also performed at this test interruption on the face of both side grooves with results presented in Figure 38. Since long IG cracks were intersected in the side groove on Side A prior to the test, direct comparison was made on their pre-test morphology versus that after 8,000 hours of exposure. As shown in the lower figure in Figure 38, no significant growth was observed for either crack, which is consistent with observations on the notch surface where pre-existing cracks exhibited little growth. No evidence of further evolution of the surface cracks were discovered after 12,000 hours of exposure. Although the load was increased by 5% twice at 13,000 and 15,000 hours, the most recent observation after 16,000 hours of exposure still did not reveal any change in surface crack morphology (Figures 36 and 37). As shown in Figure 36, another slice was taken off from Side A in CT148 after 16,000 hours to exam crack morphology in the cross-section and compare to the previous examination at 3,810 hours, of which the results will be presented in the next section.

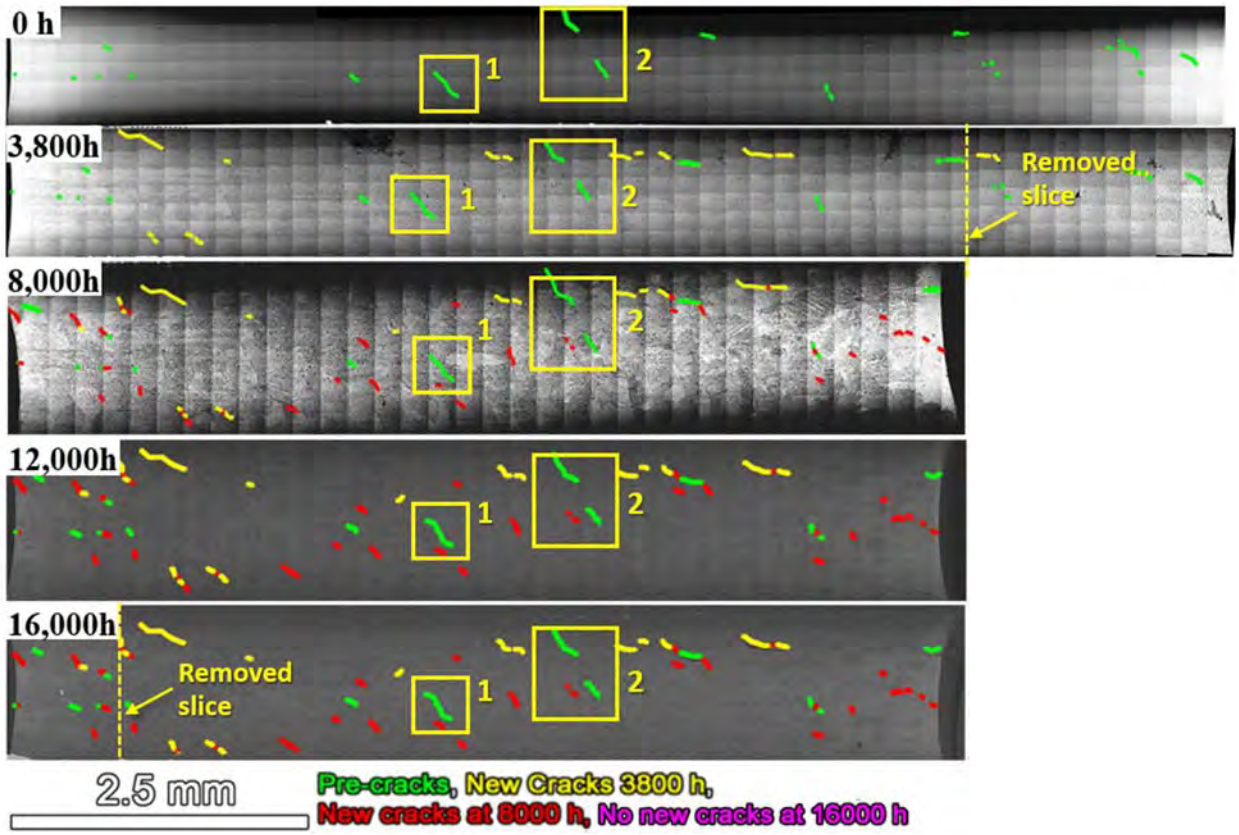

Figure 36. SEM-BSE montage imaging of the evolution of cracks on the blunt notch surface of CT148 from the EPRI WRTC 52M-316L V-groove weld over ~16,000 hours of exposure at high stress in 360°C simulated PWR primary water. Side A is always presented on the left and Side B on the right.

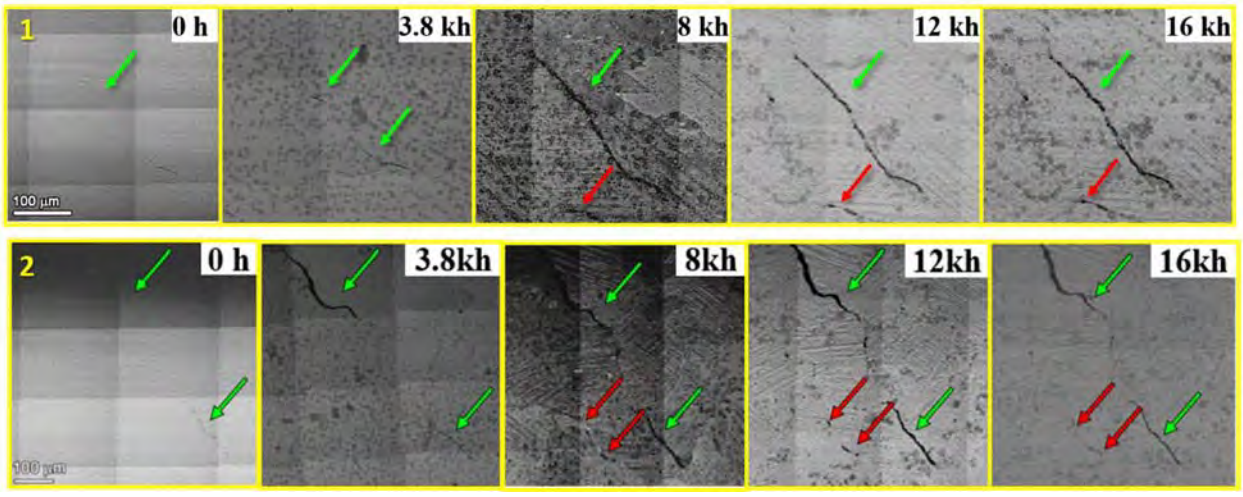

Figure 37. Higher magnification SEM-BSE image showing the evolution of cracks over ~16,000 hours of exposure in regions 1 and 2 highlighted in Figure 36 in the blunt notch surface of CT148. Green arrows indicate pre-existing cracks and red arrows indicate cracks discovered at 8,000 hours of exposure.

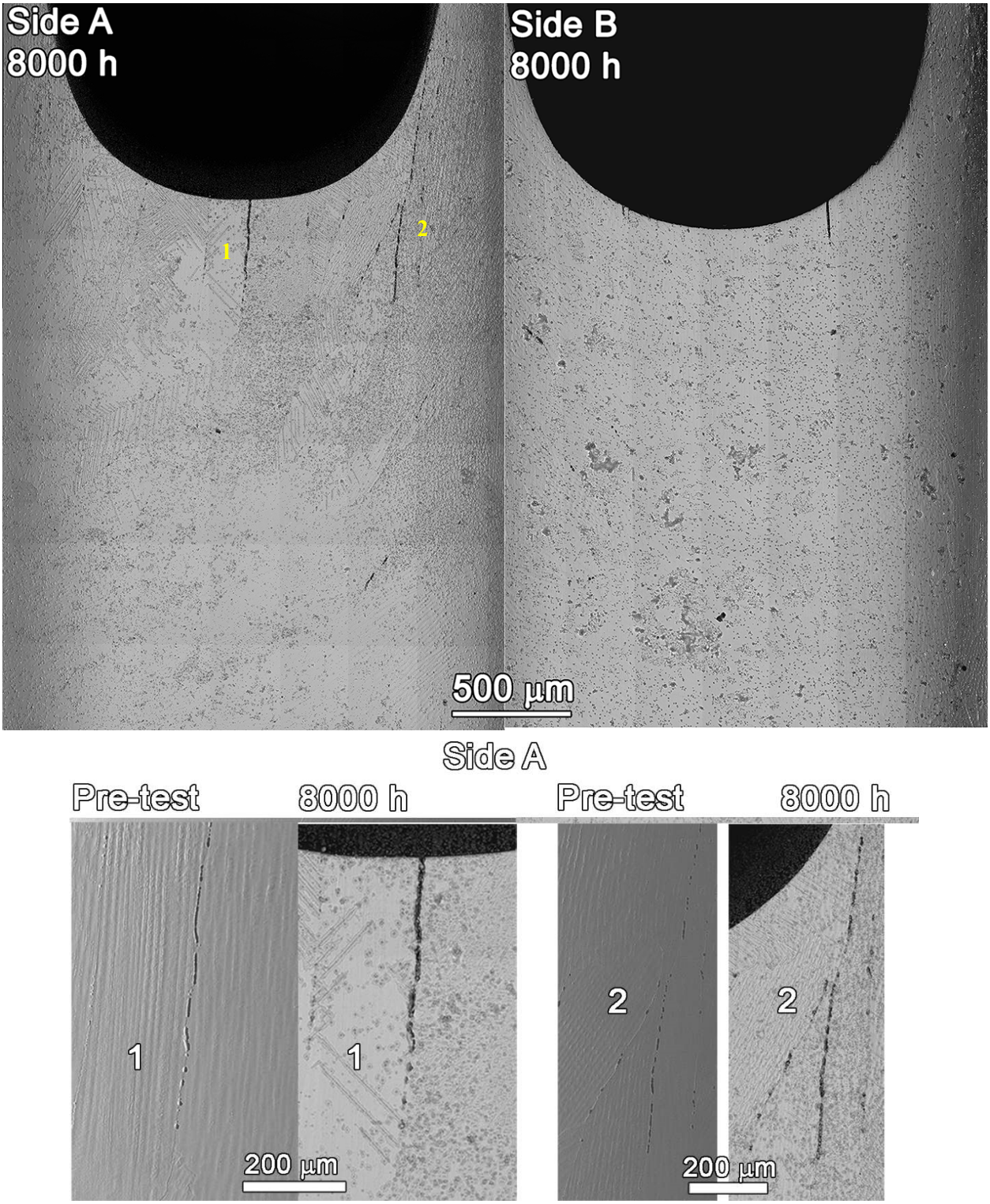

Figure 38. SEM-BSE montages of the side grooves after a test time of 8000 h are presented in the top images and comparisons are made to the pre-test examination of Side A in the bottom images.

As shown in the previous section, the other blunt notch specimen CT149 from the EPRI WRTC Alloy 52M DDC mockup did not exhibit obvious cracks on the notch surface prior to the test. SEM characterizations were performed on the notch surface at each test interruption and only revealed formation of a few crack-like features at ~3,810 and 8,000 hours (Figure 39). High magnification images on these cracks are provided in Figure 40, where discontinuous weld defects on the order of tens of micrometers were revealed. The surface of both side grooves was also examined at 8,000 hours revealing no weld defects forming in the side grooves (Figure 41). No indication of further crack initiation or growth was observed after 8,000 hours. It is noted that in order to continue SCC testing on CT148 and CT149 in series, a slice with commensurate thickness was removed from CT149 at 3,810 hours from Side B and again at 16,000 hours from Side A as shown in Figure 39.

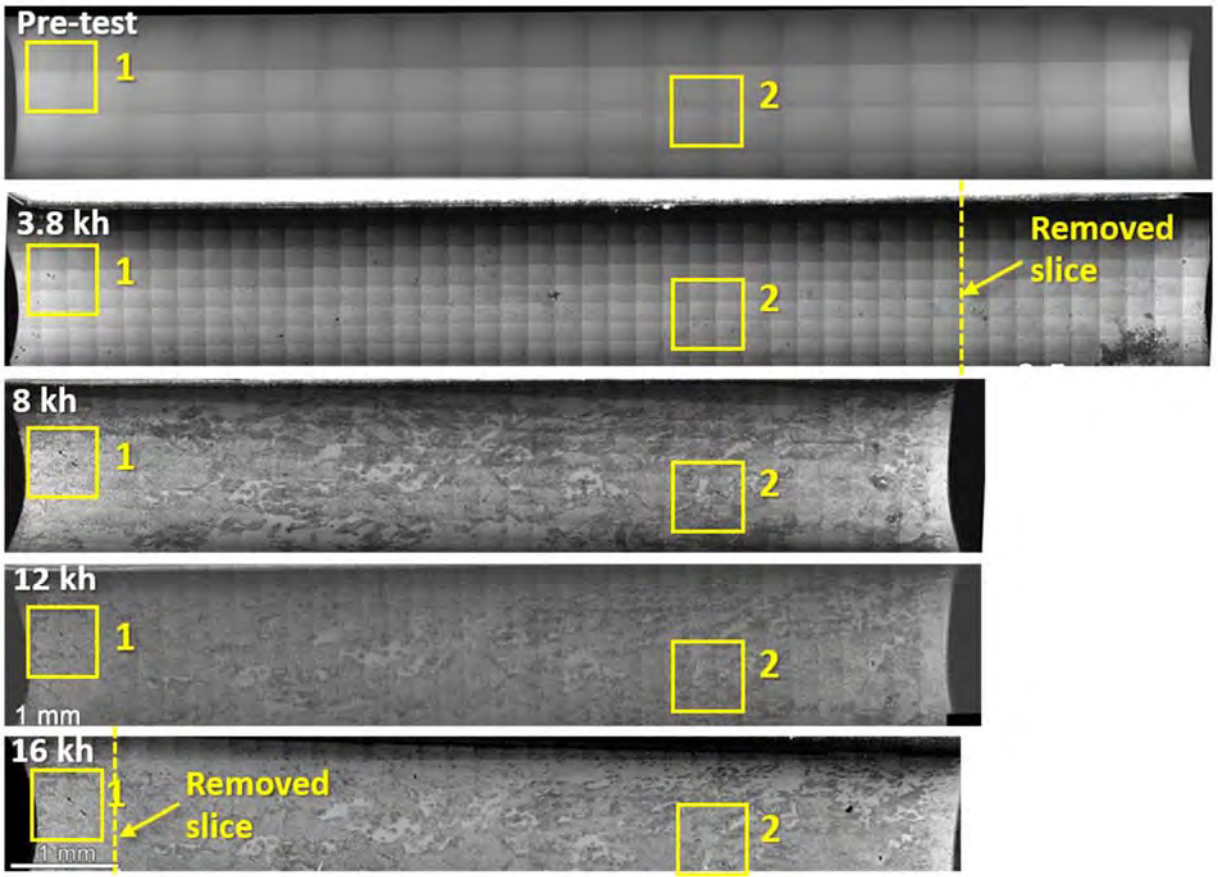

Figure 39. SEM-BSE montage imaging of the evolution of cracks on the blunt notch surface of CT148 from the EPRI WRTC 52M-316L V-groove weld over ~16,000 hours of exposure at high stress in 360°C simulated PWR primary water. Side A is always presented on the left and Side B on the right.

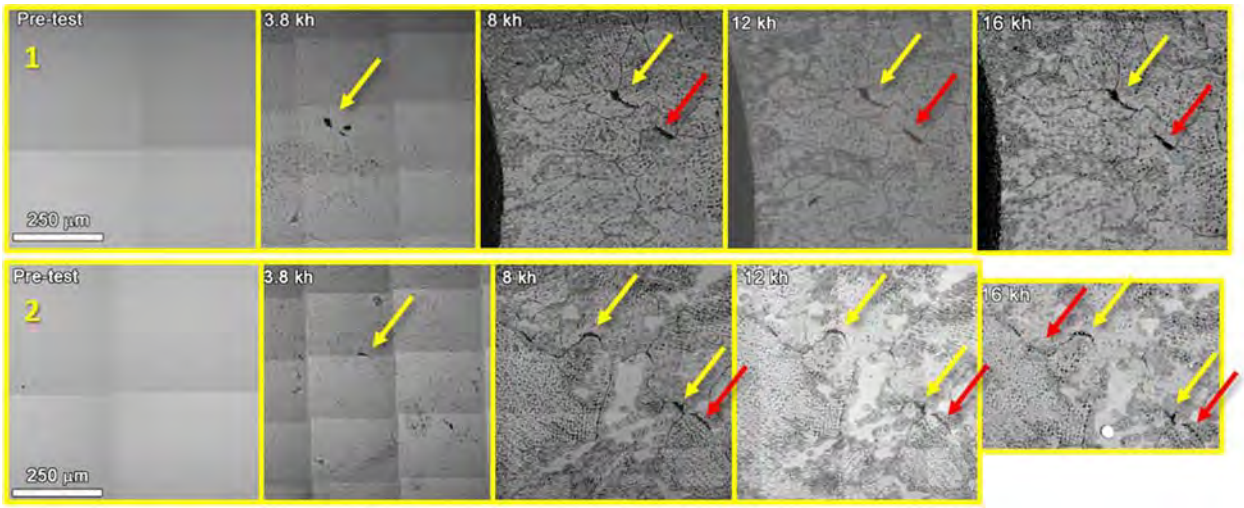

Figure 40. Higher magnification SEM-BSE image showing the evolution of possible cracks over ~16,000 hours of exposure in regions 1 and 2 highlighted in Figure 39 in the blunt notch surface of CT149. Yellow arrows indicate cracks discovered at 3810 hours and red arrows indicate cracks discovered at 8,000 hours of exposure.

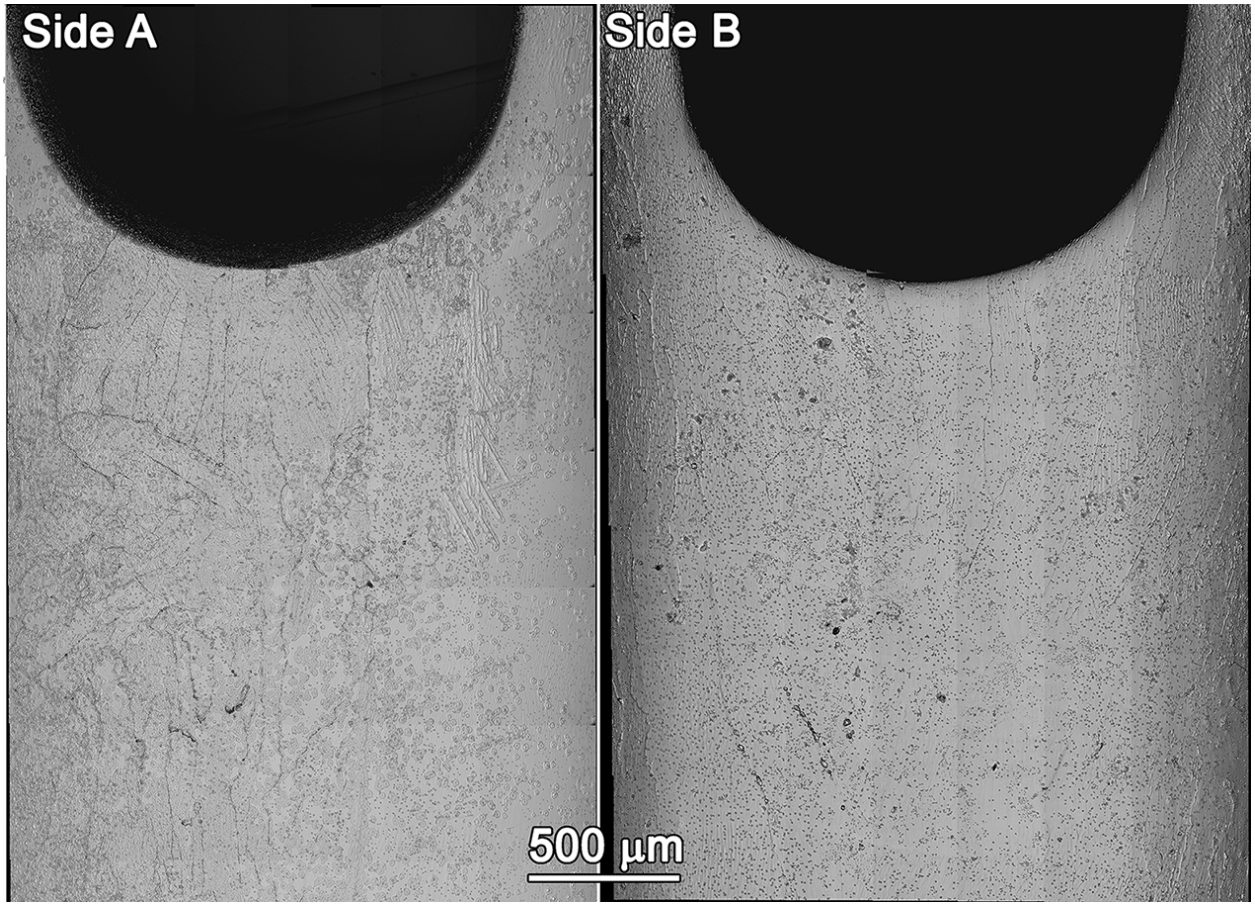

Figure 41. SEM-BSE montages of the side grooves (Side A and B) of CT149 after 8,000 h of testing.

Damage Characteristics in Specimen Cross-Sections

SEM Cross-Section Examinations on CT148 at 3,810 and 16,000 hours

As noted in Figure 36, two slices were removed from CT148 after 3,810 and 16,000 hours of exposure for cross-section examination. The slice taken off at 3,810 hours aimed to intersect a new crack discovered at this test interruption. This has been successfully achieved as shown in Figure 20 where a crack with a ~200 µm opening width in the cross-section was observed, which is consistent with its surface characteristics. SEM backscatter electron imaging shows that it is ~200 µm in depth and it is an IG crack following an elongated solidification grain boundary. The crack-tip region shown at higher magnification on the right reveals significant oxidation off the crack walls suggesting that growth into the specimen during the test is very slow. In addition, the leading crack tip appears discontinuous, suggesting the crack is moving in and out of plane.

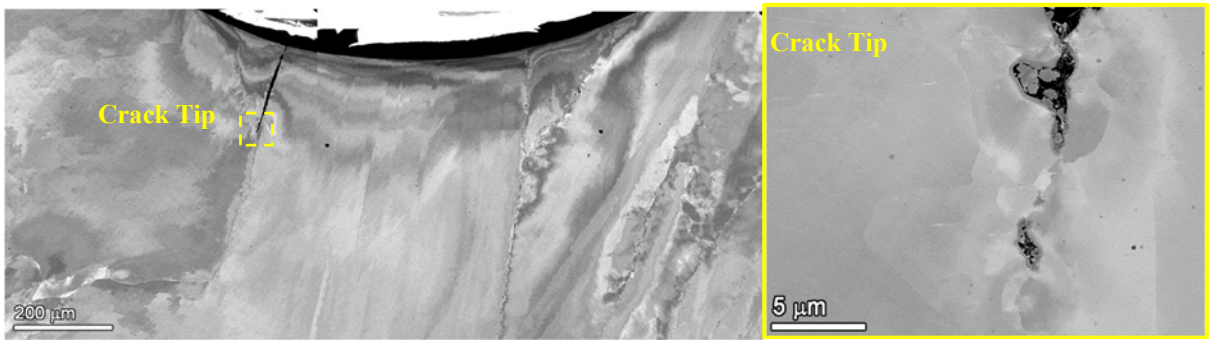

Figure 42. SEM-BSE montage highlighting two interdendritic grain boundaries in the cross-section slice from CT148 after 3,810 hours of exposure.

Another slice was removed from CT148 after 16,000 hours of exposure from the other side of the blunt notch. Iterative serial polish and SEM examination have been performed to probe cross-section morphology of several cracks present in this piece. Figure 43 illustrates the location of the serial polish plane from the top view of the blunt notch surface. The 1st polish of the thin slice did not intersect any weld defect cracks on the surface. Top down analysis of the blunt notch was subsequently performed on the already polished face, and it was determined that polishing ~100-150 µm into the side face would allow for intersection of surface cracks. Unfortunately, due to small size of the cracks and lack of experience with fine polishing of the thin A52M material, a slightly thicker than desired piece of material was removed during the 2nd polish and the initial top down examination again suggested no cracks were intersected on the surface ((Figure 43). However, cross-sectional analysis revealed a large crack with a length of ~250 µm on the right side of the image (Figure 44). A closer look at the crack near the surface region (left image in Figure 45) confirmed that it did not intersect the surface. However, it has a width of a few micrometers and is filled with oxides. Meanwhile, the leading crack front (right image in Figure 45) also exhibited a width similar to the open crack widths along the entire crack and is again filled with large, blocky oxides. In addition, penetrative oxidation was found to surround the entire crack suggests that water has made its way into this crack. It is likely that this observed subsurface crack is linked to the pre-existing weld crack that intersects the surface to its right (marked with yellow arrow). EDS elemental mapping of the leading crack front also showed the typical Cr rich oxide in the penetrative oxidation as well as the Fe and Ni rich oxides in the crack walls (Figure 46). In the higher magnification images of the leading crack front provided in Figure 47, the crack walls filled with continuous oxide and penetrative oxidation into the adjacent matrix are shown in more detail. The fact that the penetrative oxidation surrounds the leading crack front and the dark, thin lines indicative of the presence of chromia horizontal to the loading direction suggests that the crack exhibited little growth during testing. From previous analysis of the corrosion of high Cr, Ni-base alloys, the appearance of horizontal bands (to the long axis of the crack) extending into the matrix are continuous layers of chromia. Once a thin layer of chromia is

formed at the initial crack tip, Cr diffusion would continue but begin to go sideways around the leading tip forming transgranular chromia as Cr does not migrate easily through chromia. With continued corrosion, the metal is consumed as the penetrative oxidation grows and the local volume would increase as the region becomes a metal/ceramic composite. This brittle ceramic can then break, at which time water can penetrate to the depleted grain boundary ahead. This is evidenced in Figure 47 as a sub-micrometer crack emanated to the side of the original grain boundary broke through the penetrative oxide layer at the leading crack tip.

The width of the oxide filled crack in combination with the complicated damage microstructure in the penetrative oxide at the leading tip suggests that this crack, while stunted was still growing, albeit slowly. Based on progressive monitoring of the blunt notch surface, this crack was originally observed at ~3800 h of testing and then apparently stopped growing (at least longitudinally across the surface) at ~8000 h. While continuous monitoring of the depth of these large surface cracks was not feasible in this experiment, their rapid growth and appearance does suggest that their development was a function of coalescence and growth of existing weld defects along the grain boundaries in combination with exposure to high temperature water. Examinations of similar weld defects along the boundary across this cross-section were also performed to highlight the effect of continued tensile stress during testing on their structural integrity (WD1 and 2 in Figure 44).

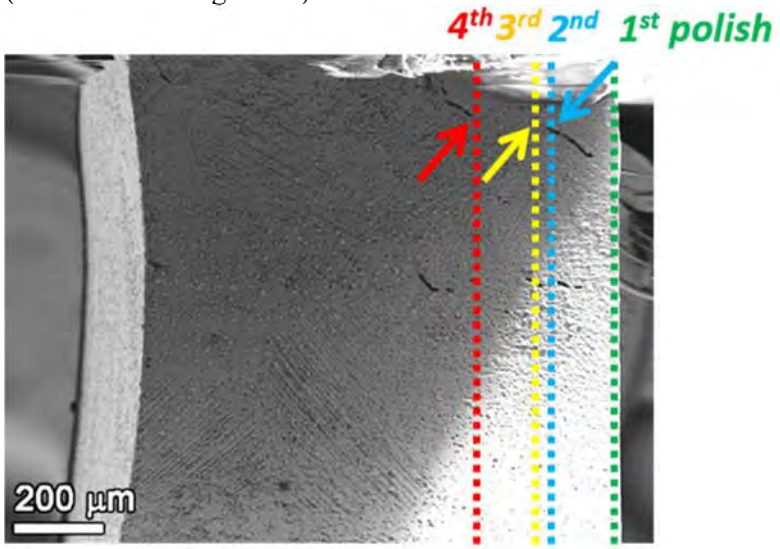

Figure 43. Top view of the location of the four sequential polish and examination series in the slice taken off from CT148 after 16,000 hours of exposure at constant load in 360°C PWR primary water.

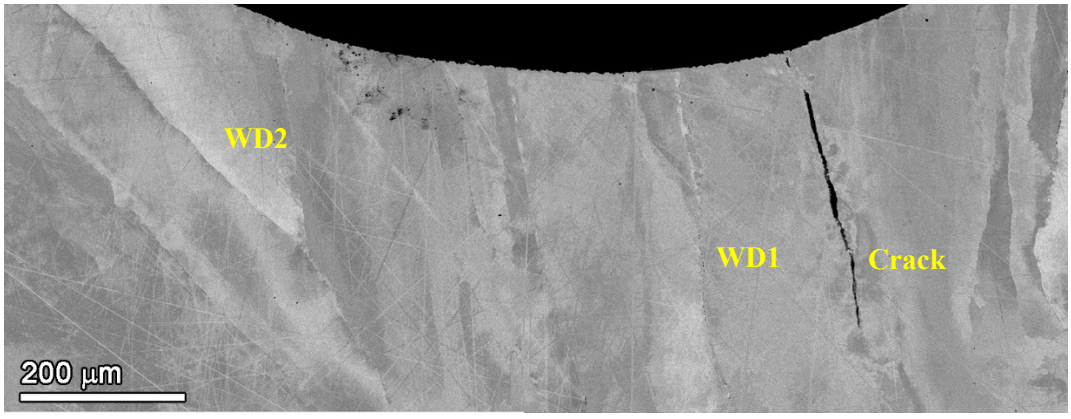

Figure 44. SEM-BSE low magnification cross-section analysis of the second polish face in the slice removed from CT148 after 16,000 hours of exposure.

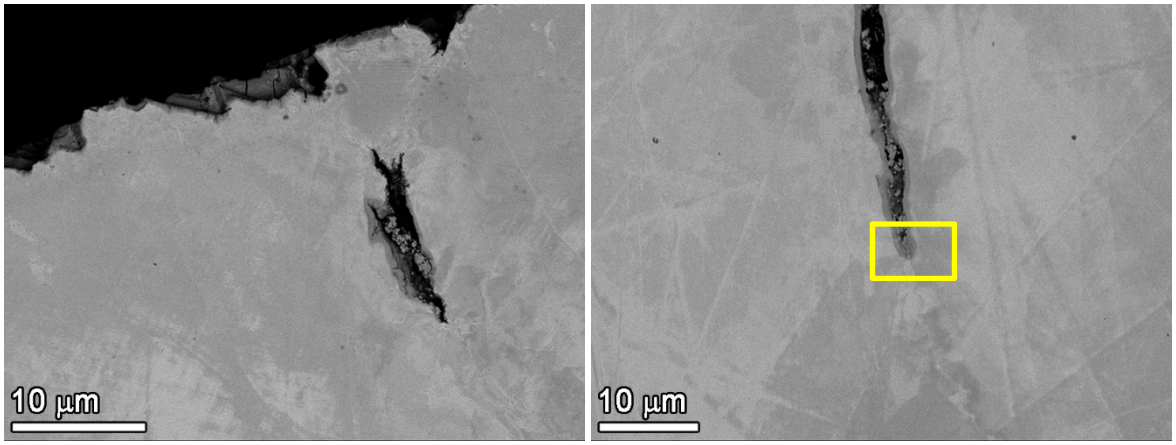

Figure 45. SEM-BSE images of the near the surface part (left) and the leading front (right) of the large crack identified in Figure 44.

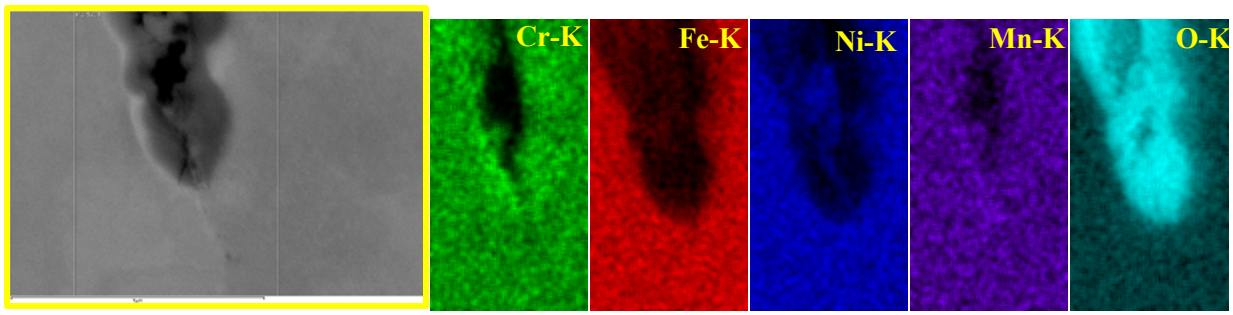

Figure 46. SEM-BSE and EDS high magnification elemental maps of the leading crack front region highlighted in Figure 45.

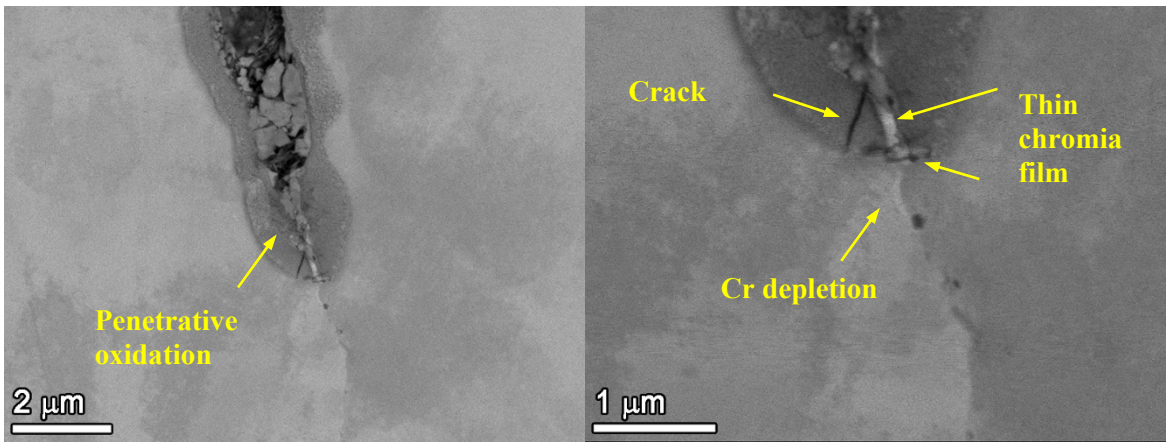

Figure 47. SEM-BSE images of the detailed morphology of the leading crack front of the large crack highlighted in Figure 45.

The weld defects (WD) along grain boundaries were examined at regions close to the larger weld crack (WD1) and as well closer to the blunt notch surface (WD2) (Figure 48). While these defects exhibited an overall length as long as 100 µm, they were always consisted of a series of semi-continuous, a few micrometers long and submicrometer wide small void segments. Higher magnification imaging of either of these regions (Figure 49) exhibit no oxide in the defect cracks (only polishing media). EDS

elemental mapping (Figure 50) was conducted to confirm the lack of any oxide in the weld defect cracks, indicating water did not make its way to these cracks through network of defects that are not observed in this cross-section.

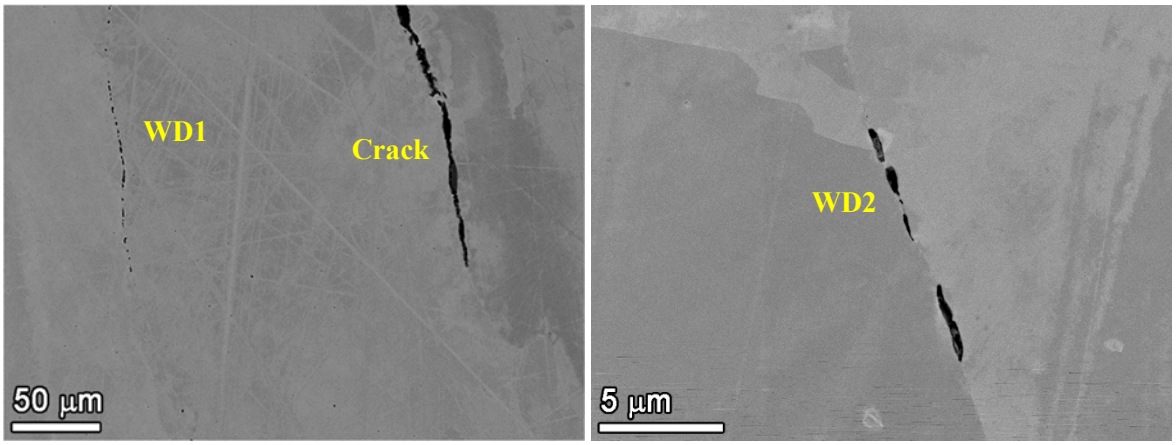

Figure 48. SEM-BSE examples of IG weld defects obseved in the slice removed from CT148 after 16,000 hours of exposure.

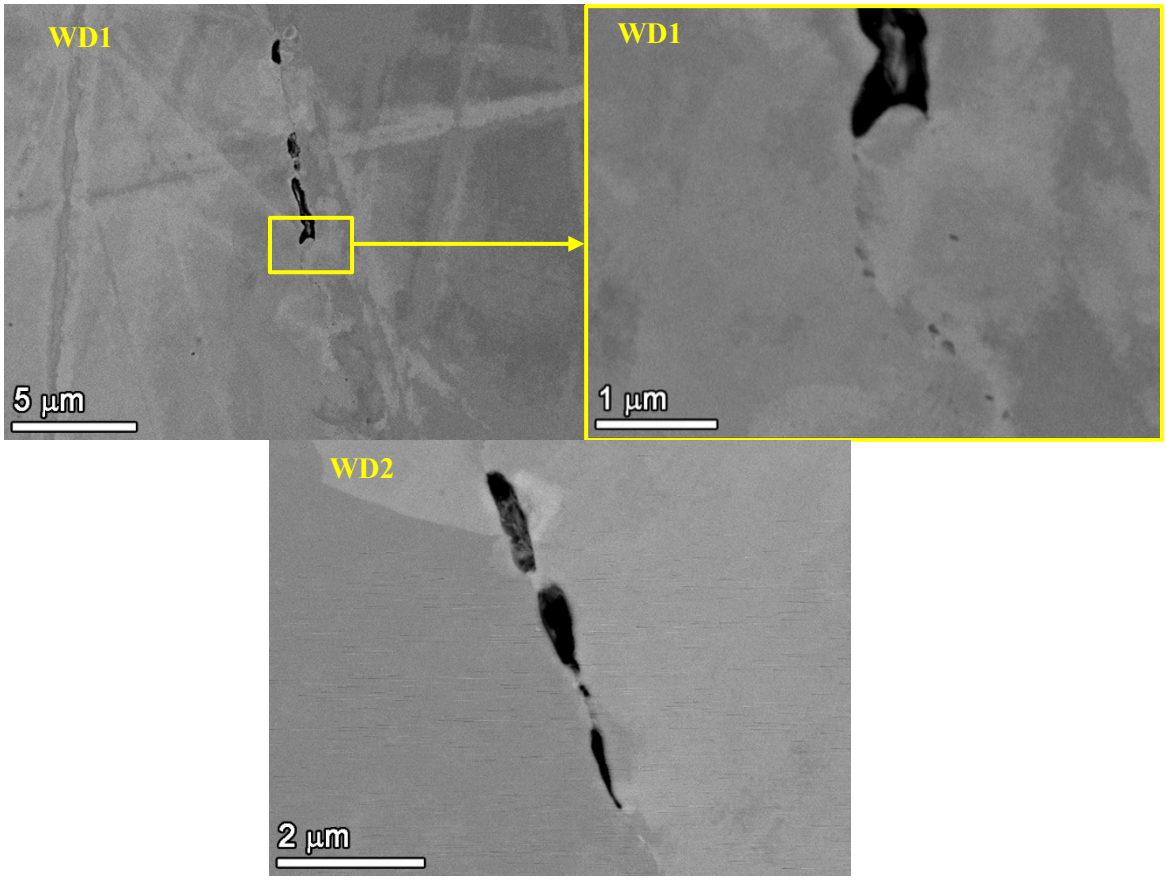

Figure 49. SEM-BSE higher magnification images of WD1 and WD2 regions showing no oxide within the defects.

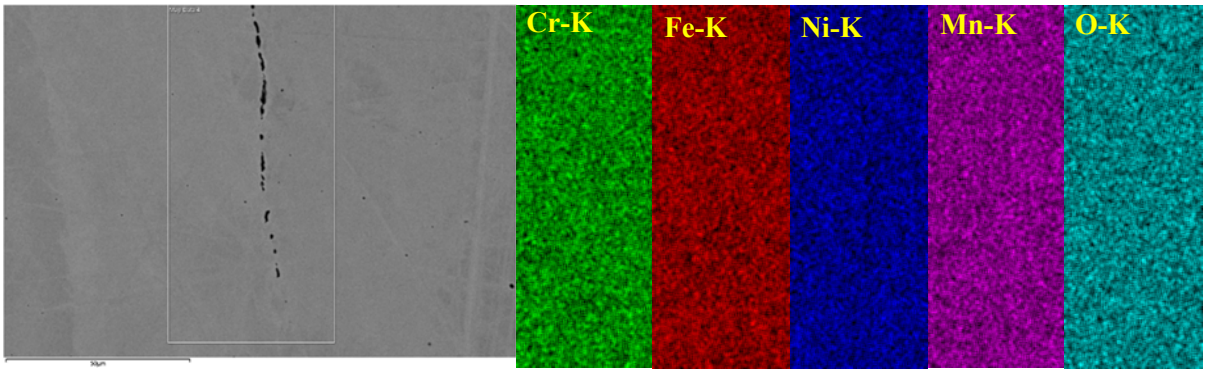

Figure 50. SEM-BSE image and EDS elemental mapping of WD1 region showing no oxide in the crack walls.

As demonstrated in Figure 43, the second polish on the thin slice taken from CT148 revealed a large subsurface crack, but did not interesect a much smaller crack in the middle of the sample. A third, very light polish was performed and intersected a small surface crack near the centerline of the notch. Due to a shorter-than-normal surface length in comparison to others cracks on the blunt notch surface, this crack was not expected to be deep. Therefore, in order to assess the location of the surface crack to the cross-section the sample was examined in the microscope at an angle of ~45° (Figure 51). The region highlighted by the yellow box indicates the approximate location of the crack in cross-section. In addition, in order to illustrate how IG damage is exhibited in these samples, a region (blue box) was also investigated.

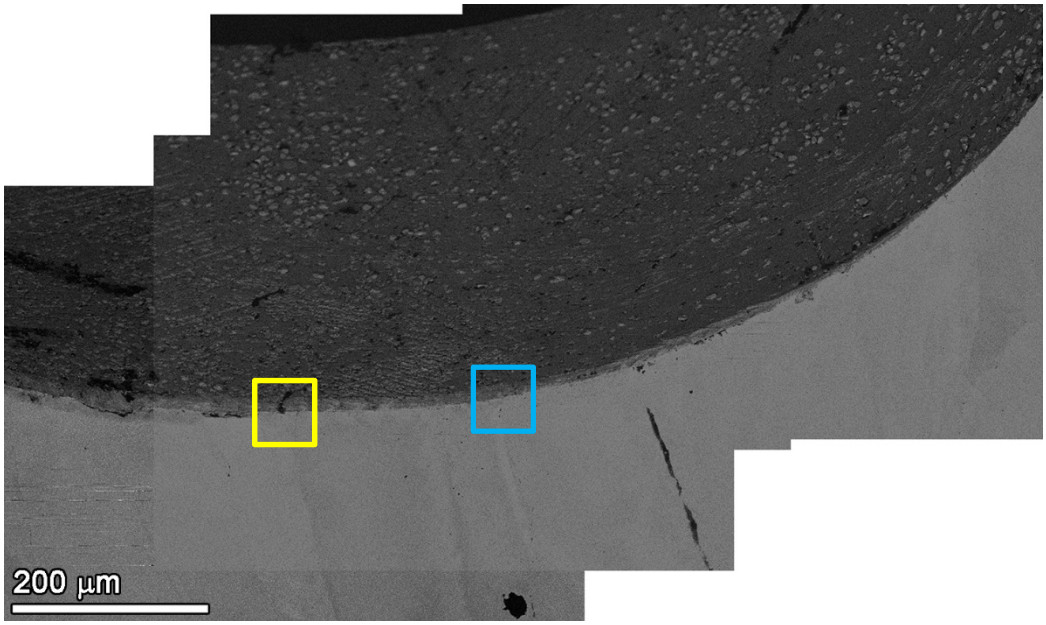

Figure 51. SEM-BSE image of the tilted slice removed from CT148 after 16,000 hours of exposure to observe top surface in relation to side surface after the 3rd minor polish.

As shown in Figure 52, the small crack with a surface length of ~40 µm long exhibited a depth of ~10 µm in the cross-section. Note that the surface finish on the edge of the curved notch was slightly rougher than normal due to the extremely light polish that was required as to not overpolish this region. The large steps at the surface of the sample and the faceting near the end of the crack is evidence of this sub-par finish. Nevertheless, localized penetrative oxidation near the crack tip was still evident. The penetrative

oxidation appeared to nearly surround the crack, but any further details which would provide more information as to whether this was a stalled or growing crack (similar to the observation in Figure 47) could not be determined. EDS analysis (Figure 53) of this SCC crack was collected, and the Cr rich nature of the penetrative oxidation as well as the Ni/Fe rich oxide in the center of the crack was observed. Small weld defect cracking ~20-30 μm ahead of the crack tip was also examined, and no apparent corrosion was detected.

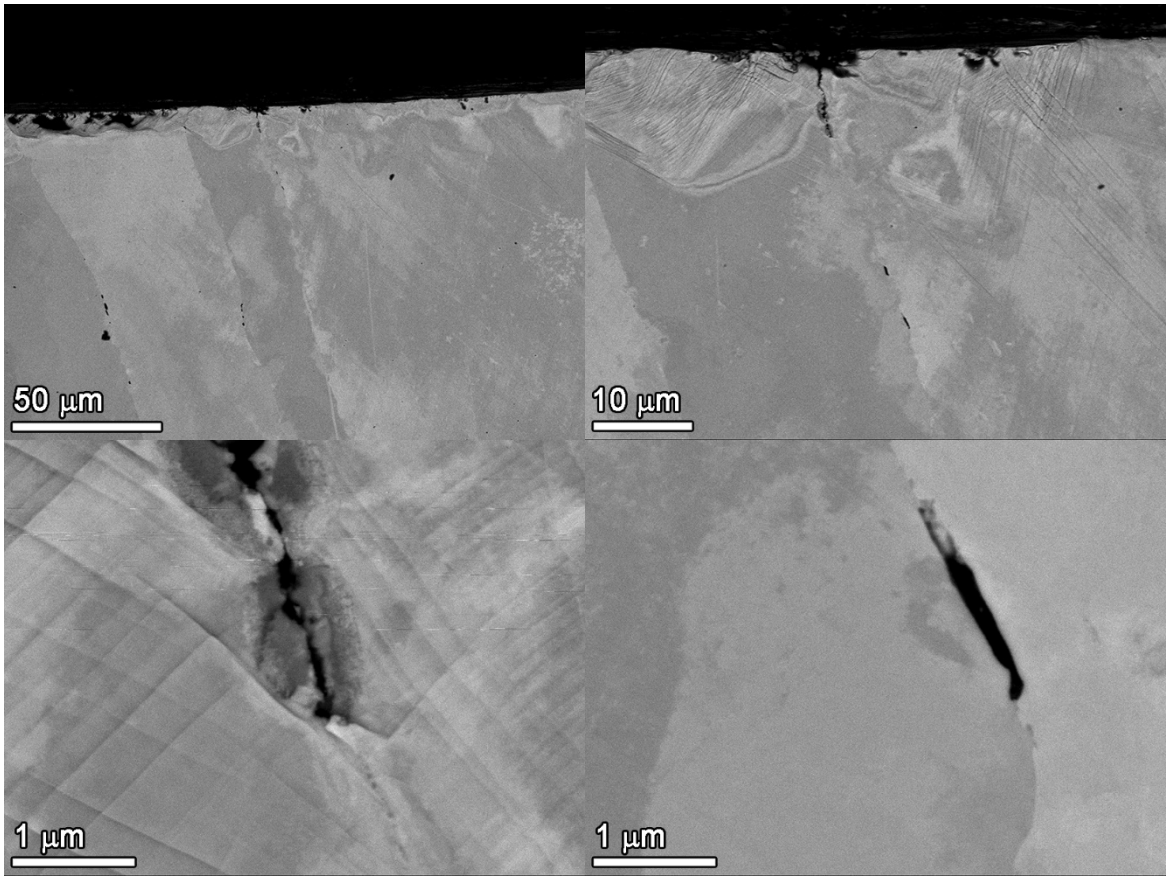

Figure 52. SEM-BSE cross-section images of a small surface crack in the slice removed from CT148 after 16,000 hours of exposure after the 3rd polish.

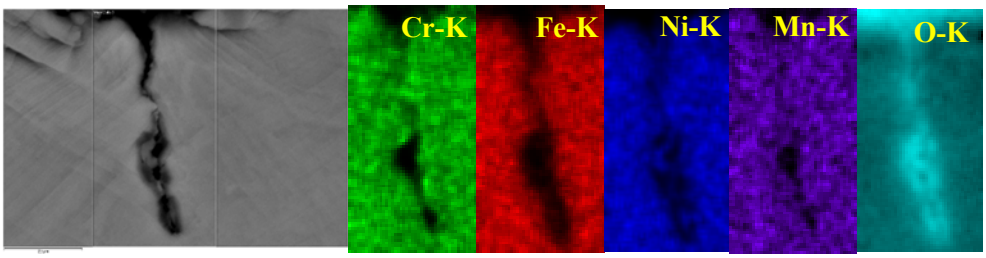

Figure 53. SEM-BSE and EDS elemental maps of a small surface crack in the slice removed from CT148 after 16,000 hours of exposure after the 3rd polish.

As noted in Figure 51, IGA of a non-cracked grain boundary (as evidenced by the lack of cracks at the surface in this region) was examined to illustrate how this weld microstructure is affected without the presence of pre-existing, intergranular weld defects. Figure 54 shows the cross-section of the blue box in Figure 51. From these examinations, shallow (~1 μm) deep penetrative oxidation is observed from the

surface. Similar to the short crack shown in Figure 52, step edges during polishing could not be fully removed and slight metal fold-over was noted at the end of the IGA, obscuring the observation of the leading IGA front. Immediately ahead of the leading IGA and ~10–15 µm ahead, pre-existing, intergranular weld defects were noted. EDS analysis (Figure 55) of the surface IGA and the weld defects ahead illustrate that the penetrative oxidation of the IGA is typical of all other corrosion observed in these samples (e.g., Cr rich, we some Fe/Ni rich oxide in the center). While there was no oxide detected in the weld defects further below the IGA on the same grain boundaries, the weld defect immediately ahead of the IGA may have had some oxide present. Due to the surface finish it is difficult to ascertain whether there truly is oxide in this weld defect or not. Since the weld defect is so close to the surface, it could be possible that high temperature water reached the defect through a connected channel that was not observed in this slice.

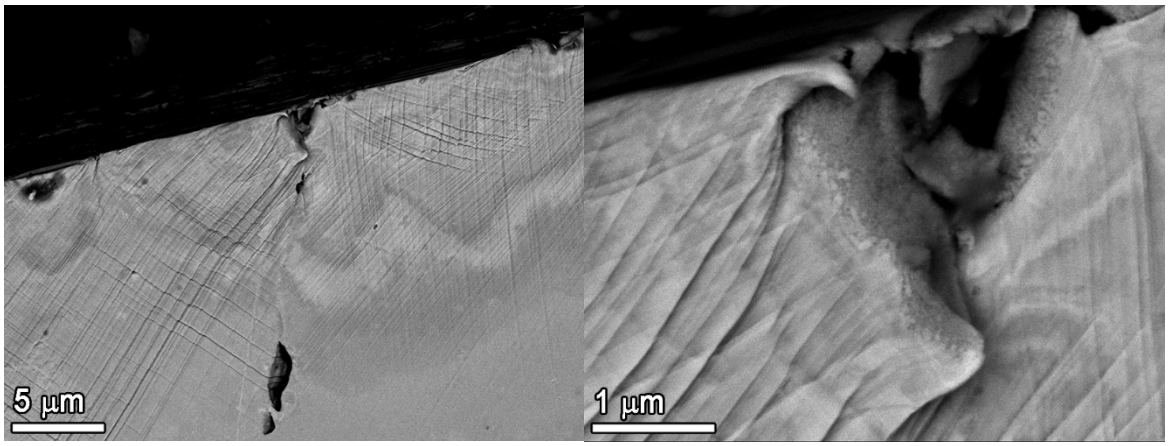

Figure 54. SEM-BSE of intergranular attack in the slice removed from CT148 after 16,000 hours of exposure after the 3rd polish.

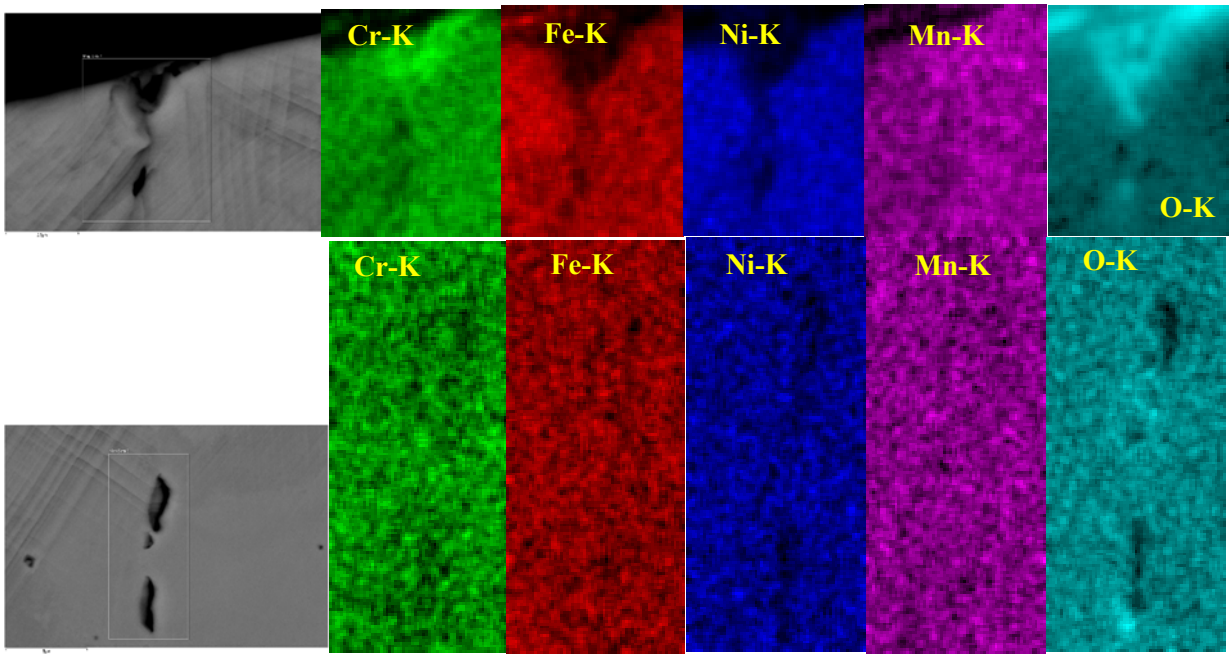

Figure 55. SEM-BSE and EDS elemental maps of surface IGA as well as a weld defect along the grain boundary ahead of the IGA shown in Figure 54.

As shown in Figure 43, the 4th polish moved forward to intersect another crack further on the left that appears to be disconnected to the crack intersected at the 1st to 3rd polish. Higher magnification examination revealed that this polish intersect one end of a new crack observed after 3800 hours of exposure as shown in Figure 56c. This crack was not seen to have grown on the surface during the subsequent exposure for up to ~12,000 hours. The cross section at this position revealed the crack has already extended to a depth of ~40 μm. Considering the fact that the observed cross-section locates just at the right end of this new crack, and recall that a depth of ~200 μm was observed for a neighboring crack at the 2nd and 3rd polishes (Figure 56a and b), which also located at just the left end of another crack, it seems reasonable to assume that these two cracks are interconnected below the surface although they appear to be two individual cracks on the surface. This also indicates that although the crack intersected at the 4th polish is marked as a new crack that formed later in the test, it may be produced by growth of the existing crack intersected at the 2nd polish.

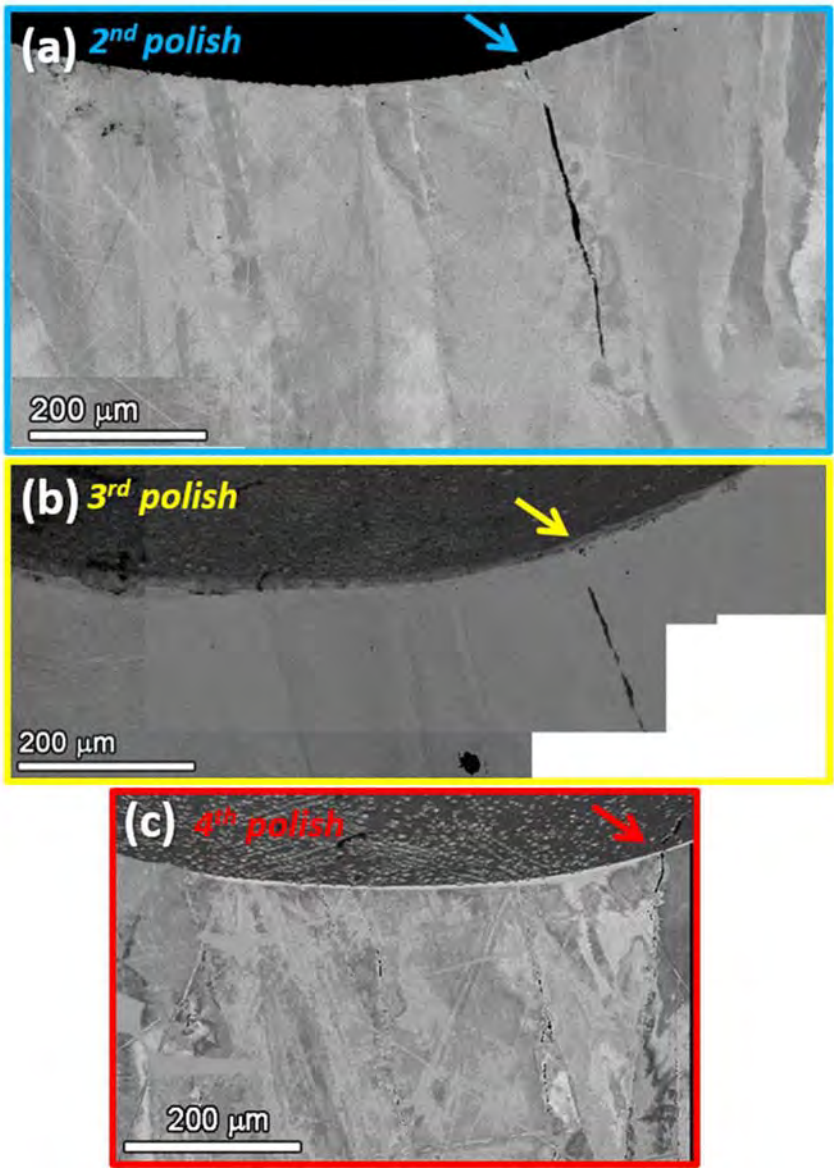

Figure 56. Cross-section morphology of the cracks found beneath the surface at positions marked in Figure 43 at each serial polish. All the images are shown at the same scale to facilitate comparison.

Close inspection of the cross-section of the crack found in the 4th polish intersecting the surface shows that it is an open crack filled with a large oxide (Figure 57). The leading crack front of this crack is also shown in Figure 57. The heavy penetrative oxidation surrounding the leading tip indicates that it is a stalled crack. As previously noted in these cracks, when the penetrative oxidation encompasses a leading crack tip it becomes brittle, additional cracking can form and breakthrough the penetrative oxidation, which is also seen here. In addition, small (10-50 nm), dark IG features were observed ahead of the leading crack tip. A weld defect is observed 15 µm ahead of the leading crack tip (Figure 58). Higher magnification of the grain boundaries adjacent to the weld defect again show small, dark semi-continuous phases that vary in contrast from dark to a lighter gray, both of which are darker than the surrounding matrix. EDS mapping was performed in these two regions and confirmed that the features ahead of the leading crack tip (Figure 59) and near the weld defect (Figure 60) are precipitates rich in Ti and Nb, which most likely suggests that they are TiN and NbC. No evidence of cavities was found in the cross-section.

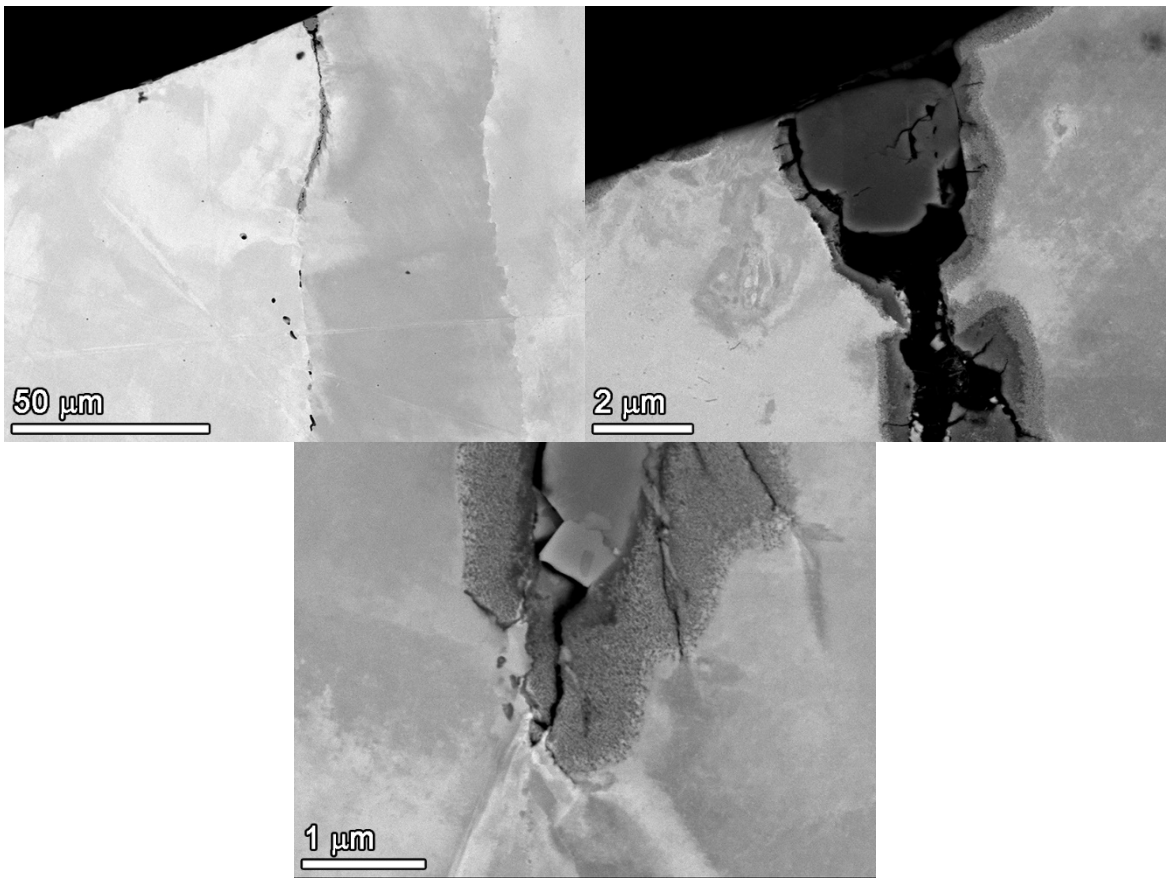

Figure 57. SEM-BSE of the crack highlighted at the 4th polish in Figure 56 showing a ~40 µm deep crack. The leading crack tip appears to be fully encased in penetrative oxidation.

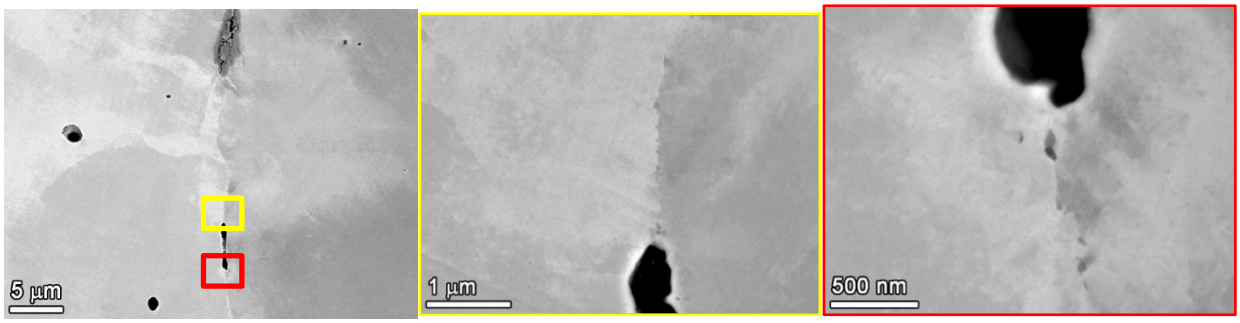

Figure 58. SEM-BSE of a weld defect ~15 µm ahead of the leading tip of the crack highlighted at the 4th polish in Figure 56.

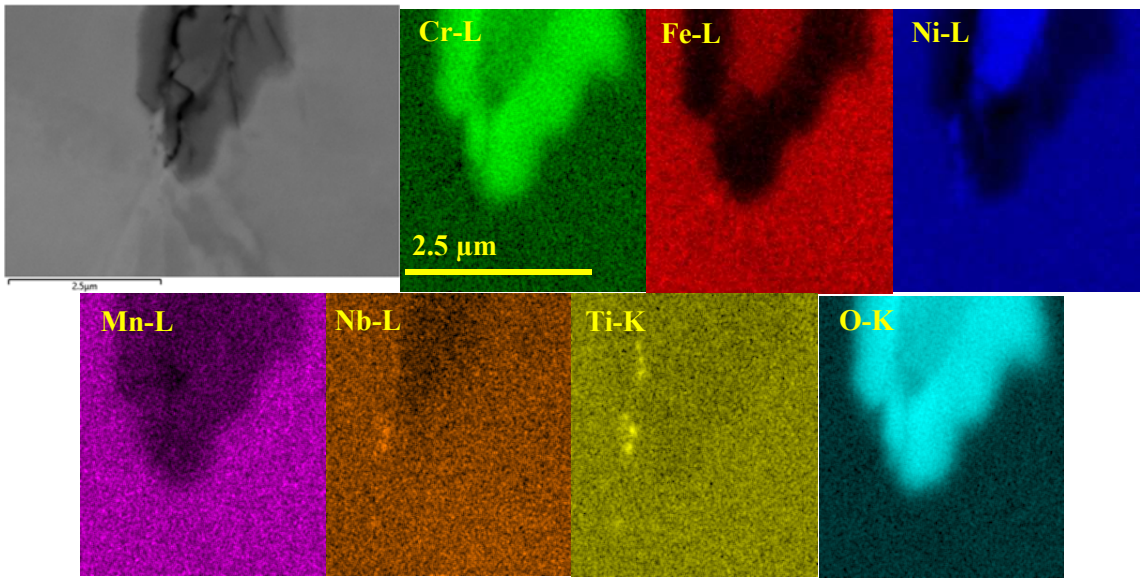

Figure 59. SEM-BSE and EDS elemental mapping of the the leading tip of the crack highlighted at the 4th polish in Figure 57 showing the Cr rich penetrative oxidation, Ni/Fe rich deposited oxide, and Nb and Ti rich precipitates on the boundary.

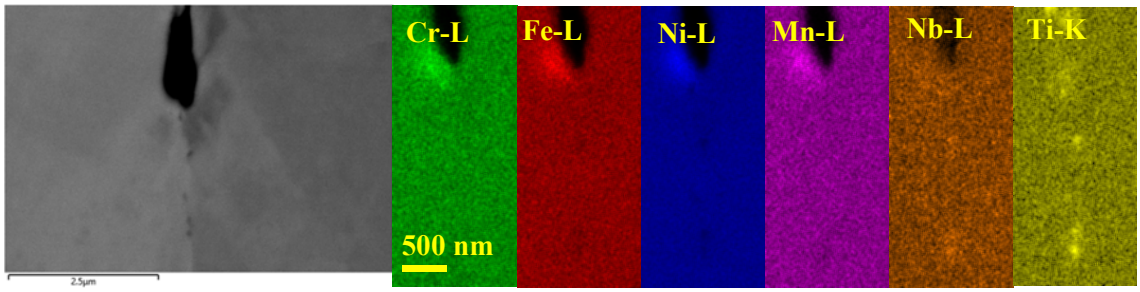

Figure 60. SEM-BSE and EDS elemental mapping of a weld defect from Figure 58 confirming the Nb and Ti rich precipitates on the grain boundary.

SEM Cross-Section Examinations on CT149 at 3,810 and 16,000 hours

The slice removed in CT149 after 3,800 hours of testing was polished to a colloidal silica finish to examine whether surface cracking was present at a length scale that imaging down the blunt not at long working distances would preclude. Figure 61 illustrates the cross-section, of which no cracks were detected near the blunt notch surface. However, a larger weld defect with wide opening and a length of 250 μm was observed ~0.5 mm below the surface. Closer examination revealed no oxide present is present at the crack walls, indicating this crack is not linked to the surface. Strain contrast was revealed around the crack suggesting turbulence in the metal possibility due to heat input during the formation of the defect. There were no other cracks observed within this cross-section.

The initial cross-section examination in the slice removed after 16,000 hours revealed neither cracks intersecting the notch surface nor pre-existing defects below the notch surface, which is consistent with the low density of DDC cracks in this weld. Additional polish and examinations are underway and the results will be reported in the future.

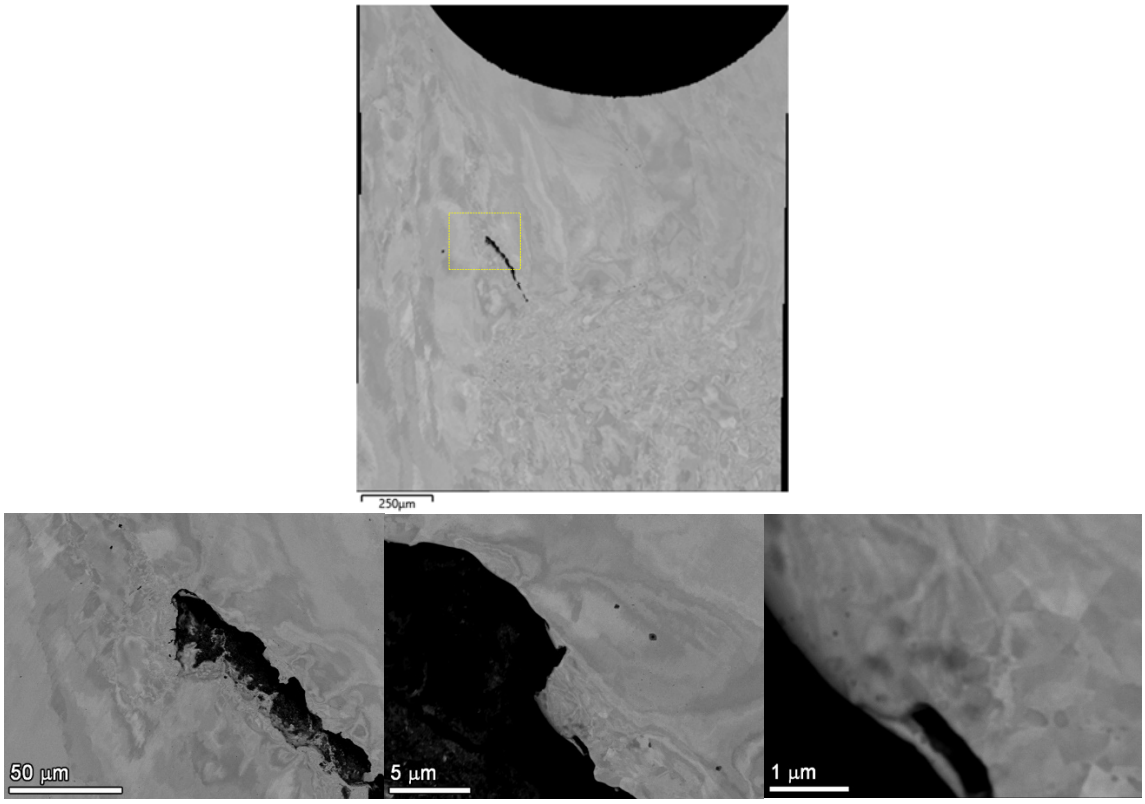

Figure 61. SEM-BSE images showing the cross-section of Side A after 8,000 hours. No apparent weld defects were noted at the surface, and only one large (250 μm) weld defect was observed in the interior of the sample.

SUMMARY AND CONCLUSIONS

Long-term SCC initiation testing are being conducted on high-Cr, Ni-base Alloy 690 and its weld metals at constant load in 360°C simulated PWR primary water with recent progress summarized in this report. Periodic high-resolution microstructural characterizations performed on tested specimens are providing key information to understand possible degradation mechanism in these SCC resistant materials over long-term exposure and facilitating the prediction of their service life in LWRs.

Alloy 690 is considered resistant to SCC because a protective oxide layer readily forms above GB intersecting the surface when exposed to high-temperature water due to its high Cr content. However, the ongoing research has demonstrated an alternate mechanism of crack initiation in this material through formation and growth of GB cavities induced by creep. While previously this was only observed in highly CW materials featuring nanometer-sized carbides with spacing commensurate to their size after 1-2 years of exposure in high temperature water, the latest results revealed that materials having GB carbides of similar size but wider spacings (up to ~10X of the carbide size) can also become susceptible to IG nucleation due to increasing GB cavities after longer exposure times. Interestingly, this was observed in not only highly, but also moderately CW condition of this material. To better understand the effect of cold work on GB cavity evolution, supplementary quantification was conducted in material with similar microstructure in 21%CW condition. A >50% increase was observed in both cavity density and GB cavity coverage from 1-year to 2-year exposure in high temperature water. However, the absolute values remained very low and no crack nucleation was found. In addition, unlike in the 31%CW condition where the increase of applied stress to yield strength has dramatically promoted GB cavity formation and growth in this material, little effect of applied stress on GB cavity evolution was seen after the same duration of exposure in 21%CW condition, highlighting the complexity involved in cavity evolution with impacts from multiple variables. The new results also revealed that with extended exposure for up to 2 years, neither obvious increase in GB cavity distribution nor IG crack formation was observed in highly CW materials with the most susceptible GB carbide microstructure but loaded at 90% YS, or in highly CW materials without GB carbides. However, it is still too early to rule out the possibility of crack occurring after longer exposure in these conditions that appear less susceptible for now. Long-term SCC initiation testing is continuing with expanded specimen matrix to better evaluate degradation behavior of Alloy 690 materials in these conditions.

The investigation of SCC initiation in the compatible weld metals of Alloy 690 focused on whether the presence of pre-existing defects can promote SCC initiation and growth in service. This is because weld cracking is recognized as a significant issue during the joining of high-Cr, Ni-base alloys and their effect on SCC remains poorly understood. In order to make assessment possible, two BNCT specimens were carefully machined to ensure that pre-existing DDC cracks intersected the notch surfaces of both specimens. Detailed SEM examinations were performed every ~4,000 hours on the notch surface for a total exposure time of ~16,000 hours in 360°C simulated PWR primary water. In the specimen that exhibited a moderate density of pre-existing IG cracks on the surface, limited nucleation of new small cracks and minor growth of a few pre-exiting DDC cracks have taken place with a decreasing trend over increased exposure times. The other specimen contains fewer pre-existing crack-like features that showed little growth during the entire exposure. No clear evidence of new crack nucleation was found except for formation of a few very small crack-like features. In-situ DCPD has not been able to detect crack initiation or growth in these specimens suggesting that the cracks observed on the blunt notch surface are very shallow. This has been confirmed by cross-section examination on slices removed from specimens after 3,810 and 160,000 hours. The cracks that were found to intersect the notch surface all feature thick penetrative oxidation along the crack walls indicating very slow growth of cracks during exposure. This is consistent with the observed crack evolution on the notch surface and suggests that the presence of pre-existing weld cracks did not promote SCC initiation susceptibility in Alloy 52M welds.

REFERENCES

1. Zhai, Z., et al., Precursor damage evolution and stress corrosion crack initiation of cold-worked alloy 690 in PWR primary water. September 2016.
2. Zhai, sZ., M.B. Toloczko, and S.M. Bruemmer, Stress corrosion crack initiation behavior of Alloy 600 and Alloy 690 in PWR primary water. September 2018.
3. Zhai, Z., et al., Grain boundary microstructure effects on stress corrosion crack initiation mechanisms in Alloy 600 and Alloy 690. September 2019.
4. Zhai, Z., et al., Stress corrosion crack initiation of alloy 600 in PWR primary water. Corrosion Science, 2017. 123: p. 76-87.
5. Toloczko, M.B., et al. Stress corrosion crack initiation measurements of alloy 600 in PWR primary water. in 17th International Conference on Environmental Degradation of Materials in Nuclear Power Systems - Water Reactors. 2015. Ottawa, ON, Canada: Canadian Nuclear Society.
6. Zhai, Z., et al., Summary of Stress Corrosion Crack Initiation Measurements and Analyses on Alloy 600 and Alloy 690. September 2015.
7. Arioka, K., 2014 Whitney Award Lecture: Change in Bonding Strength at Grain Boundaries before Long Term SCC Initiation. Corrosion, 2015. 71(4): p. 403-419.
8. Arioka, K., et al., Role of Cavity Formation in Crack Initiation of Cold-Worked Carbon Steel in High-Temperature Water. Corrosion, 2013. 69(5): p. 487-496.
9. Arioka, K., et al., Dependence of Stress Corrosion Cracking of Alloy 690 on Temperature, Cold Work, and Carbide Precipitation - Role of Diffusion of Vacancies at Crack Tips. Corrosion, 2011. 67(3): p. 035006-1-035006-18.
10. Arioka, K., et al., Degradation of Alloy 690 After Relatively Short Times. CORROSION, 2016. 72(10): p. 1252-1268.
11. Zhai, Z., et al., Precursor Evolution and Stress Corrosion Cracking Initiation of Cold-Worked Alloy 690 in Simulated Pressurized Water Reactor Primary Water. CORROSION, 2017. 73(10): p. 1224-1236.
12. Zhai, Z., et al., Grain Boundary Damage Evolution and SCC Initiation of Cold-Worked Alloy 690 in Simulated PWR Primary Water, in 18th International Conference on Environmental Degradation of Materials in Nuclear Power Systems – Water Reactors, J.H. Jackson, D. Paraventi, and M. Wright, Editors. 2018, Springer International Publishing: Portland, OR, USA. p. 457-483.
13. Zhai, Z., et al. Precursor corrosion damage and stress corrosion crack initiation in alloy 600 during exposure to PWR primary water. in 17th International Conference on Environmental Degradation of Materials in Nuclear Power Systems - Water Reactors. 2015. Ottawa, ON, Canada: Canadian Nuclear Society.
14. Andresen, P.L., I.P. Vasatis, and F.P. Ford, Behavior of short cracks in stainless steel at 288°C, in CORROSION 1990. 1990, NACE: Las Vegas, Nevada, USA.
15. Richey, E., D.S. Morton, and M.K. Schurman. SCC initiation testing of nickel-based alloys using in-situ monitored uniaxial tensile specimens. in 12th International Conference on Environmental Degradation of Materials in Nuclear Power Systems - Water Reactors. 2005. Salt Lake City, UT, USA: The Minerals, Metals & Materials Society.
16. Bruemmer, S.M., et al., Stress Corrosion Crack Initiation of Cold-Worked Alloy 600 and Alloy 690 in PWR Primary Water. September 2014.
17. Bruemmer, S.M., M.B. Toloczko, and M.J. Olszta, Pacific Northwest National Laboratory Investigation of Stress Corrosion Cracking in Nickel-Base Alloys, Volume 2. 2012, Pacific Northwest National Laboratory.
18. Toloczko, M.B., et al., Pacific Northwest National Laboratory Investigation of Stress Corrosion Cracking in Nickel-Base Alloys, Volume 3: Stress Corrosion Cracking of Cold-Worked Alloy 690. 2015, Pacific Northwest National Laboratory.